AN IN-SITU INVESTIGATION OF SOLID ELECTROLYTE INTERPHASE FORMATION ON ELECTRODE MATERIALS FOR LITHIUM-ION BATTERIES USING SPECTROSCOPIC ELLIPSOMETRY

by

Mark A. McArthur

Submitted in partial fulfillment of the requirements
for the degree of Master of Science

at

Dalhousie University
Halifax, Nova Scotia
August 2011

DALHOUSIE UNIVERSITY

DEPARTMENT OF PHYSICS AND ATMOSPHERIC SCIENCE

The undersigned hereby certify that they have read and recommend to the Faculty of Graduate Studies for acceptance a thesis entitled "AN IN-SITU INVESTIGATION OF SOLID ELECTROLYTE INTERPHASE FORMATION ON ELECTRODE MATERIALS FOR LITHIUM-ION BATTERIES USING SPECTROSCOPIC ELLIPSOMETRY" by Mark A. McArthur in partial fulfillment of the requirements for the degree of Master of Science.

Dated: August 8, 2011

Supervisor: _____

Readers: _____

_____

DALHOUSIE UNIVERSITY

DATE: August 8, 2011

AUTHOR: Mark A. McArthur

TITLE: AN IN-SITU INVESTIGATION OF SOLID ELECTROLYTE INTERPHASE FORMATION ON ELECTRODE MATERIALS FOR LITHIUM-ION BATTERIES USING SPECTROSCOPIC ELLIPSOMETRY

DEPARTMENT OR SCHOOL: Department of Physics and Atmospheric Science

DEGREE: MSc CONVOCATION: October YEAR: 2011

_____

Signature of Author

To Mom and Dad…

Table of Contents

List of Tables vii
List of Figures viii
Abstract xii
List of Abbreviations and Symbols Used xiii
Acknowledgements xix
Chapter 1 Introduction 1
1.1 Thesis Structure 3
Chapter 2 Lithium-Ion Batteries 4
2.1 Introduction to Li-Ion Cells 4
2.2 Negative Electrode Materials 11
2.3 The Solid Electrolyte Interphase Model 13
2.3.1 Modeling the SEI 15
2.3.2 Measuring Physical Properties of the SEI 19
2.4 Electrolytes and Additives for Li-Ion Batteries 23
Chapter 3 Background and Theory of Spectroscopic Ellipsometry 26
3.1 History and Development 26
3.2 Principles of Optics 27
3.3 Principles of Spectroscopic Ellipsometry 40
Chapter 4 Other Instrumentation 49
4.1 Magnetron Sputter Deposition 49
4.2 In-situ Electrochemical Cell 54
Chapter 5 Experimental Details 58
5.1 Electrode Preparation 58
5.2 Electrode Characterization 59
5.3 Electrochemical and Spectroscopic Ellipsometry Testing 65
5.3.1 Constant Current Testing 66
5.3.2 Constant Potential Testing 67

5.4 Optically Modeling SE Data 68
5.4.1 Refractive Indices of Nonaqueous Electrolyte 71
5.4.2 Refractive Indices of the SEI 71
5.4.3 Modeling the Baseline and Extracting Surface Film Thickness 72
Chapter 6 Results and Discussion 74
6.1 Preliminary Optical Measurements 74
6.1.1 Optical Properties of Bare Electrode Materials 74
6.1.2 Optical Properties of Electrolyte and SEI 81
6.2 In-situ Electrochemical Measurements 84
6.2.1 a-Si Thin Film Electrodes 86
6.2.2 Ni Thin Film Electrodes 93
6.2.3 TiN Thin Film Electrodes 99
Chapter 7 Conclusion 113
7.1 Future Work 114
Bibliography 116

List of Tables

Table 2.1 Contrasting various commercial cell chemistries available today. Li-ion batteries provide the largest voltage, specific energy, and energy densities among the cell chemistries shown. 6

Table 2.2 List of physical properties of several common salts for Li-ion batteries..... 24

Table 5.1 Sputtering conditions for the listed target materials. 59

Table 6.1 Fitting parameters for two models from bare a-Si thin film electrodes measured using spectroscopic ellipsometry in air. Model 1 gives parameters from a single Tauc-Lorentz oscillator. Model 2 gives the parameters from a 2-term Tauc-Lorentz oscillator. 76

Table 6.2 Fitting parameters for a model used to determine the optical properties and thickness of a bare TiN thin film electrode measured by spectroscopic ellipsometry in air. To model the TiN electrode, a single Drude-type and two Lorentz-type oscillators were used. 79

Table 6.3 Cauchy parameters used to determine the real part of the refractive index for various electrolytes and the SEI used in all in-situ electrochemical testing. 83

Table 6.4 Descriptions of the Li/TiN cells displayed in Figure 6.20. 108

List of Figures

Figure 1.1 A schematic of a commercial graphite/$LiCoO_2$ Li-ion cell in the discharged state just before the start of a charge. 2

Figure 2.1 Schematic of the interior of a Li-ion coin cell used to study different cell chemistries, cycling behaviour, and more for various electrode materials.... 4

Figure 2.2 Voltage curves for Li/graphite and Li/$LiCoO_2$ cells cycled in the same electrolyte (1 M $LiPF_6$/EC:DEC(1:2)). 8

Figure 2.3 Potentiostatic chronoamperometry study on a Li/TiN cell in 1 M $LiPF_6$/EC:DEC(1:2) held at 0.5 V at 22ºC..... 10

Figure 2.4 Graphical comparison of specific capacities of negative electrode alloy materials vs graphite. (Adapted from Ref. [16]). 12

Figure 2.5 Equilibrium Li-Ni phase diagram. 12

Figure 2.6 Schematic of the SEI developed on a negative electrode. Letters indicate the SEI species as described in the legend. (Adapted from [2]). .. 14

Figure 2.7 Schematic representation of the solvent diffusion model for determining the growth of the SEI on negative electrode materials. 17

Figure 3.1 Electromagnetic (light) wave propagating from a dielectric medium with $n = n_1$ and $k = 0$ to a dielectric medium with $n = n_2$ and: (a) $k = 0$ and (b) $k > 0$. 30

Figure 3.2 Electric field, $\boldsymbol{E}$, and induced magnetic field, $\boldsymbol{B}$, for: (a) p-polarization and (b) s-polarization. 32

Figure 3.3 A simple optical model consisting of ambient/transparent film of thickness *d*/thick reflective substrate with complex refractive indices of N_0, N_1, and N_2, respectively. 35

Figure 3.4 Representations of (a) linear polarization, (b) circular polarization, and (c) elliptical polarization. 40

Figure 3.5 Block diagramme of the optical components of the J.A. Woollam M-2000 spectroscopic ellipsometer at Dalhousie University. 42

Figure 3.6 Geometry of a typical ellipsometry measurement. 44

Figure 4.1 Schematic of a top-down cross-sectional view of a sputtering chamber and components during a deposition of a target material. 49

Figure 4.2 Cross-sectional view of a magnet, target material, and Cu backing plate used in magnetron sputter deposition. 50

Figure 4.3 Photograph of the magnetron sputter deposition machine used to prepare thin film electrodes for electrochemical testing. 52

Figure 4.4 Schematic of various sputtering masks including: a constant mask (a), a "linear out" mask (b), and a "linear in" mask (c). 53

Figure 4.5 Schematic (a) and photographs (b) of the in-situ electrochemical cell used for study with spectroscopic ellipsometry. 54

Figure 4.6 Cross-section of the in-situ electrochemical cell, including the Li electrode support (a), the working electrode material "well" (b), the working electrode material (c), and the fused quartz tube body (d). 56

Figure 5.1 Total film thickness (a) and mass densities (b) of a a-Si sputter deposition along the length of the sputtering track. 60

Figure 5.2 Total film thickness (a) and mass densities (b) of a Ni sputter deposition along the length of the sputtering track. 61

Figure 5.3 Total film thickness (a) and mass densities (b) of a TiN sputter deposition along the length of the sputtering track. 62

Figure 5.4 X-ray diffraction data for three electrodes used for SEI investigations. ... 64

Figure 5.5 Time dependence of the ellipsometric parameters, Ψ and Δ, for 3 wavelengths during a 3 hour equilibrium period for an in-situ cell with a TiN working electrode at open circuit. 65

Figure 5.6 A simple 2-phase optical model consisting of a Si substrate and its native SiO_2 oxide. 68

Figure 5.7 Cauchy dispersion curve describing the real part of the refractive index of a transparent SiO_2 film with respect to wavelength. 69

Figure 6.1 Ellipsometric parameters (open circles), Ψ and Δ, and the corresponding fitting results from two optical models for a bare a-Si thin film electrode measured in air. 75

Figure 6.2 Ellipsometric parameters (open circles), Ψ and Δ, and the corresponding fitting results from an optical model for a bare Ni thin film electrode measured in air. 77

Figure 6.3 Ellipsometric parameters (open circles), Ψ and Δ, and the corresponding fitting results from an optical model for a bare TiN thin film electrode measured in air. 78

Figure 6.4 Optical constant (*n*, *k*) for the a-Si (a), Ni (b), and TiN (c) thin film electrodes determined from the optical models for each electrode in air. ... 80

Figure 6.5 Optical constants for the electrolytes used with the in-situ electrochemical cell. 82

Figure 6.6 Optical constants for the SEI layer determined by potentiostatic chronoamperometry using a Li/TiN electrode. 84

Figure 6.7 Voltage-time curve of an in-situ cell constructed with no active working electrode material. 85

Figure 6.8 Time dependence of the ellipsometric parameters, Ψ and Δ, for 5 wavelengths during cycling of two Li/a-Si in-situ cells at constant current.. 87

Figure 6.9 Time slices of the ellipsometric parameters during cycling of a Li/a-Si in-situ cell.. 90

Figure 6.10 Predicted ellipsometric parameters of an a-Li_xSi_{1-x} alloy electrode in 0.1 M $LiPF_6$/EC:DEC (1:2) as x varies from 0.0 to 1.0. 92

Figure 6.11 Time dependence of the ellipsometric parameters, Ψ and Δ, for 5 wavelengths during cycling of a Li/Ni in-situ cell between 0.005 V and 3.0 V. 94

Figure 6.12 Voltage curve of the first 3 cycles of a Li/NiO cell. 96

Figure 6.13 Differential capacity curve for 2 cycles of a Li/Ni in-situ cell cycled between 0.005 V and 3.0 V at a C/5 rate. 97

Figure 6.14 Time dependence of the surface film thickness, MSE to the fit of the optical model to the ellipsometric data, and corresponding voltage curve of a Li/Ni in-situ cell cycled at C/5 (80 μA). 98

Figure 6.15 Time dependence of the ellipsometric parameters, Ψ and Δ, for 3 wavelengths during a potential hold study of a Li/TiN in-situ cell using 1 M $LiPF_6$/EC:DEC electrolyte. 100

Figure 6.16 Time dependence of the ellipsometric parameters, Ψ and Δ, for 3 wavelengths during a potential hold study of a Li/TiN in-situ cell using 1 M $LiPF_6$/EC:DEC/2 wt.% VC electrolyte. 101

Figure 6.17 Time dependence of the ellipsometric parameters, Ψ and Δ, for 3 wavelengths during a potential hold study of a Li/TiN in-situ cell using 1 M $LiPF_6$/EC:DEC/2 wt.% FEC electrolyte. In the bottom panel, the cell current is shown. Potential "steps" were, in order, 1.0 V, 0.5 V, 0.1 V, 1.0 V, 2.0 V, and 3.0 V. The beginning of the transition to another potential "step" is shown as a steep change in slope. 102

Figure 6.18 Time dependence of the ellipsometric parameters, Ψ and Δ, for 2 wavelengths during a potential hold study of a Li/TiN in-situ cell using 1 M $LiPF_6$/EC:DEC electrolyte. 105

Figure 6.19 Fit of the ellipsometric data from t = 53 hrs of the potential hold study to determine the optical constants of the SEI (Figure 6.18). 106

Figure 6.20 SEI thicknesses and MSEs determined ellipsometrically on TiN electrodes in Li/TiN in-situ cells using potentiostatic chronoamerometry. The electrolytes used were 1 M $LiPF_6$/EC:DEC (1:2) (a), 1 M $LiPF_6$/EC:DEC (1:2)/2% VC (b), and 1 M $LiPF_6$/EC:DEC (1:2)/2% FEC (c). 107

Figure 6.21 SEI layer thickness grown on TiN electrodes in Li/TiN in-situ cells plotted against the total charge, *Q*, delivered to the in-situ cells. 110

Abstract

A novel method to detect and quantify the growth of the solid electrolyte interphase (SEI) on battery electrode materials using in-situ spectroscopic ellipsometry (SE) is presented. The effects of additives in 1 M $LiPF_6$/EC:DEC (1:2) electrolyte on the SEI were studied. Thin film electrodes of a-Si, Ni, and TiN were prepared by magnetron sputtering for use with a custom-designed tubular in-situ electrochemical cell. Li/a-Si and Li/Ni in-situ cells in 0.1 M $LiPF_6$/EC:DEC (1:2) were studied by galvanostatic chronopotentiometry. Large changes in the ellipsometric parameters, Ψ and Δ, were observed for both materials. These changes were closely related to the state of charge of the in-situ cell. The formation of an a-Li_xSi alloy, the formation of an SEI layer, or both contributed to these large changes for a Li/a-Si in-situ cell. For a Li/Ni in-situ cell, a thin transparent surface layer was observed. The surface layer, presumably made from SEI species and species from the displacement reaction between NiO and Li, increased to roughly 17 nm during the first discharge. During the first charge, the surface layer thickness decreased to roughly 5.5 nm and could not be removed, even at high potentials. The effect of vinylene carbonate (VC) and fluoroethylene carbonate (FEC) additives on SEI formation were studied using a Li/TiN in-situ cell in 1 M $LiPF_6$/EC:DEC (1:2) by potentiostatic chronoamperometry. SEI thicknesses for cells containing no additives, VC, and FEC were roughly 18 nm, 25 nm and 30 nm, respectively, after a 10 h hold at 0.1 V. SE is a useful technique for measuring thin film growth in-situ on electrode materials for Li-ion batteries.

List of Abbreviations and Symbols Used

α_2	normalized Fourier coefficient
α_4	normalized Fourier coefficient
β	phase thickness
β_2	normalized Fourier coefficient
β_4	normalized Fourier coefficient
γ	width of Lorentz or Drude oscillator
γ-BL	γ-butyrolactone
Δ	phase difference between s- and p-polarization components
Δ^{exp}	measured phase difference
ΔG	Gibbs free energy
Δ^{model}	predicted phase difference
δ	initial phase of traveling wave
δ_{rp}	p-component phase difference after reflection
δ_{rs}	s-component phase difference after reflection
ε	complex dielectric constant
ε_0	permittivity of free space (8.85×10^{-12} F/m)
ε_1	real part of the complex dielectric constant
ε_2	imaginary part of the complex dielectric constant
ε_∞	offset dielectric constant
ζ	modified boundary condition after change of variables
θ_0	angle of incidence of light on layer '0'
θ_1	angle of incidence of light on layer '1'
θ_2	angle of incidence of light on layer '2'
θ_B	Brewster angle
θ_i	angle of incidence
θ_r	angle of reflection
θ_t	angle of transmission
λ	wavelength

μ_{neg}	chemical potential of a negative electrode
μ_{pos}	chemical potential of a positive electrode
π	constant (3.14159265358979323846264338327950288419716939937510 5…)
ρ	ellipsometric quantity
σ_{Δ}^{exp}	standard deviation of the phase difference
σ_{Ψ}^{exp}	standard deviation of the amplitude ratio
χ	dielectric susceptibility
Ψ	amplitude ratio
Ψ^{exp}	measured amplitude ratio
Ψ^{model}	predicted amplitude ratio
ω	angular frequency
ω_C	angular rotational frequency of a compensator
a	dummy variable
A	Cauchy parameter
AFM	atomic force microscopy
A_j	amplitude of a Lorentz or Drude oscillator
a-Li_xSi	amorphous-Li_xSi
AN	acrylonitrile
a-Si	amorphous-Si
B	Cauchy parameter
$\boldsymbol{B}_{ip}$	incident induced magnetic field vector in p-direction
$\boldsymbol{B}_{is}$	incident induced magnetic field vector in s-direction
B_{is}	magnitude of the incident induced magnetic field vector in s-direction
$\boldsymbol{B}_{rp}$	reflected induced magnetic field vector in p-direction
$\boldsymbol{B}_{rs}$	reflected induced magnetic field vector in s-direction
B-spline	basis-spline
$\boldsymbol{B}_{tp}$	transmitted induced magnetic field vector in p-direction
$\boldsymbol{B}_{ts}$	transmitted induced magnetic field vector in s-direction
B_{ts}	magnitude of the transmitted induced magnetic field vector in s-direction
C	rotational angle of the compensator
C	Cauchy parameter

c_0	proportionality constant
c_1	integration constant
CCD	charge-coupled device
c_{eq}	equilibrium molar density
c_{light}	speed of light in a vacuum (2.998×10^{8} m/s)
c_P	insoluble product molar density
c_S	solvent molar density
d	layer thickness
DC	direct current
DEC	diethyl carbonate
DMC	dimethyl carbonate
D_S	effective diffusivity constant of solvent in the solid electrolyte interphase
e	charge of an electron (1.602×10^{-19} C)
$\boldsymbol{E}$	electric field vector
E	1-dimensional electric field
e^-	an electron
$\boldsymbol{E}_0$	electric field vector amplitude constant
E_0	1-dimensional electric field amplitude constant
E_{01}	1-dimensional electric field amplitude constant at an interface
E_{after}	1-dimensional electric field at the bottom of a film stack
E_{before}	1-dimensional electric field at the top of a film stack
EC	ethylene carbonate
E_D	electric field observed at a detector
$E_{incident}$	incident electric field on a film stack
$\boldsymbol{E}_{ip}$	incident electric field vector in the p-direction
E_{ip}	magnitude of the incident electric field vector in the p-direction
EIS	electrochemical impedance spectroscopy
$\boldsymbol{E}_{is}$	incident electric field vector in the s-direction
EMA	effective medium approximation
EMF	electromotive force; potential; voltage
En	energy of a Lorentz or Drude oscillator

En_0	position of a Lorentz or Drude oscillator
E_j^r	*j*th reflected electric field from a film stack
$\boldsymbol{E}_{rp}$	reflected electric field vector in the p-direction
E_{rp}	magnitude of the reflected electric field vector in the p-direction
$\boldsymbol{E}_{rs}$	reflected electric field vector in the s-direction
E_{total}^r	total reflected electric field from a film stack
$\boldsymbol{E}_{tp}$	transmitted electric field vector in the p-direction
E_{tp}	magnitude of the transmitted electric field vector in the p-direction
$\boldsymbol{E}_{ts}$	transmitted electric field vector in the s-direction
F	Faraday's constant (96485 C/mol)
FEC	fluoroethylene carbonate
FTIR	Fourier transform infrared spectroscopy
HOPG	highly ordered pyrolitic graphite
I	current
i	the imaginary number ($\sqrt{-1}$)
I	light intensity
I_0	initial light intensity constant
I_{ip}	incident light intensity in the p-direction
I_{is}	incident light intensity in the s-direction
IRC	irreversible capacity
I_{rp}	reflected light intensity in the p-direction
I_{rs}	reflected light intensity in the s-direction
k	extinction coefficient
$L(t)$	time-dependent thickness of the solid electrolyte interphase
M	number of variable parameters in an optical model
MCMB	mesocarbon microbead
MN_x	metal nitride
MP3	moving picture experts group-1 audio layer III
MSE	absolute mean-squared error
n	index of refraction

N	complex index of refraction
n_e	number of electrons
N	number of (Ψ, Δ) pairs sampled
N_0	complex index of refraction of layer ‘0’
N_1	complex index of refraction of layer ‘1’
N_2	complex index of refraction of layer ‘2’
N_i	complex index of refraction of the incident medium
n_i	index of refraction of the incident medium
NMC	$LiNi_{1-x-y}Mn_xCo_yO_2$
N_t	complex index of refraction of the transmission medium
n_t	index of refraction of the transmission medium
P	insoluble product
p	parallel polarization direction relative to plane of incidence
PC	propylene carbonate
P_ε	1-dimensional dielectric polarization
Q	charge transferred to cell
q	dummy variable
q^*	complex conjugate of dummy variable
$\hat{q}$	directional unit vector
$\boldsymbol{r}$	spatial coordinate vector
r	dummy variable
r_{01}	Fresnel amplitude reflection coefficient at the 01 interface
$r_{012,\mathrm{p}}$	total Fresnel amplitude reflection coefficient in the p-direction
$r_{012,\mathrm{s}}$	total Fresnel amplitude reflection coefficient in the s-direction
r_{10}	Fresnel amplitude reflection coefficient at the 10 interface
r_{12}	Fresnel amplitude reflection coefficient at the 12 interface
RAE	rotating-analyzer ellipsometer
RC	reversible capacity
RCE	rotating-compensator ellipsometer
RF	radio frequency
r_p	Fresnel amplitude reflection coefficient in the p-direction

R_p	reflectance in the p-direction
RPE	rotating-polarizer ellipsometry
r_s	Fresnel amplitude reflection coefficient in the s-direction
R_s	reflectance in the s-direction
S	solvent
s	perpendicular polarization direction relative to plane of incidence
S_1	first Stokes vector
S_2	second Stokes vector
S_3	third Stokes vector
SE	spectroscopic ellipsometry
SEI	solid electrolyte interphase
t	time
t_{01}	Fresnel amplitude transmission coefficient at the 01 interface
t_{10}	Fresnel amplitude transmission coefficient at the 10 interface
THF	tetrahydrofuran
t_p	Fresnel amplitude transmission coefficient in the p-direction
t_s	Fresnel amplitude transmission coefficient in the s-direction
u	dummy variable for change of variable solution
V	electromotive force; potential; voltage
v	speed of light in a medium
VA	vinyl acetate
VC	vinylene carbonate
wMSE	weighted mean-squared error
x	stoichiometric number of species present in a chemical reaction
XPS	x-ray photoelectron spectroscopy
XRD	x-ray diffraction
x_{SEI}	solid electrolyte interphase layer thickness
y	stoichiometric number of species present in a chemical reaction
y	dummy variable
z	1-dimensional spatial coordinate

Acknowledgements

This thesis would not have been possible if it wasn't for all of the help and support from various individuals from inside and outside of the Dahn Lab.

Thank you, Mom and Dad, for always believing in me as I travel along my academic path. Thanks for all the guidance, support, (delicious peanut butter cookies), and love you've shown me over the years.

Roberta, thanks for putting up with me and my work schedule. I apparently owe you some time… after another 4 more years…

Many thanks go out to Robbie for training on the sputtering machine and other laboratory equipment. Also, thanks for putting up with me for all these years. The lab would not run as smoothly without you!

Thank you, Simon, for spending time fabricating many "dainty" parts for use with the in-situ cell.

Thanks to the staff of the physics department, especially Andy George for cutting so many quartz tubes and the office staff for answering so many little questions along the way.

Chris Bums, thanks for sharing the Master's experience with me. I couldn't have done it without you.

Thanks to all the members of the Dahn Lab for your support and guidance throughout my time here. I have learned a lot, not only from grueling course work, but also from you guys! Special thanks to Braden, Jessie, Jock, Gary, Tims (both of them), John, Eric, Aaaaaron, Patrick, and Dave for invaluable *chin-wags* which gave me a much needed repose between measurements and coursework!

Most of all, Jeff, thank you for the excellent supervision, not only for my MSc, but also my undergrad "life" as well. You have always inspired me to be better at… everything! You have also improved my repertoire of wacky sayings! I will always cherish my time in your lab.

Finally, thanks to NSERC and Killam for the much-needed cash money.

Chapter 1 Introduction

Lithium-ion (Li-ion) batteries power everything from portable electronics (cellular telephones, MP3 players, digital cameras, portable computers, etc.) to vehicles (such as the Nissan Leaf). A Li-ion battery is composed of two conducting electrodes (one positive, one negative) surrounded by an electrolyte separated by a thin porous film (called a separator) which allows for Li^+ ion mobility. Together, the negative electrode/separator/positive electrode combination form an electrochemical cell by which Li^+ ions are transported from the positive electrode to the negative electrode, mediated by the electrolyte, during a charge. A corresponding electron is released from the Li atom which flows through the external circuit. The reverse of this process is called a discharge. During a discharge, the flow of released electrons can be used to do electrical work. Hence, a Li-ion battery can be used to produce electrical work from chemical work and vice versa. This behaviour allows for many charge/discharge cycles over the lifetime of a cell, delivering current to devices when and where a consumer desires.

Figure 1.1 displays a general schematic of a commercial Li-ion cell consisting of a graphite negative electrode and a $LiCoO_2$ positive electrode in a discharged state. The electrode materials are "pasted" onto conductive current collectors to facilitate the motions of the electrons. Li^+ ions, viewed as green spheres, have been inserted within the layers of the positive electrode and are just beginning to intercalate between the graphite layers as a charge current is applied.

After many charge/discharge cycles, the retained charge within the cell decreases and the cell no longer operates effectively. This phenomenon occurs due to chemical reactions at the surfaces of the negative and positive electrode materials. The electrolyte species decompose during cycling and thin surface layers are formed on the electrodes. On the electrodes, these layers are called the solid electrolyte interphase (SEI) [1, 2], and it will be the focus of much of this thesis. The SEI on the negative electrode forms during the first charge/discharge cycle and irreversibly consumes Li^+ ions in the cell, thus reducing the available lithium that can transfer charge [3-5]. This layer keeps building

up during the subsequent charge/discharge cycles and ultimately affects the calendar life of a Li-ion cell [6-8].

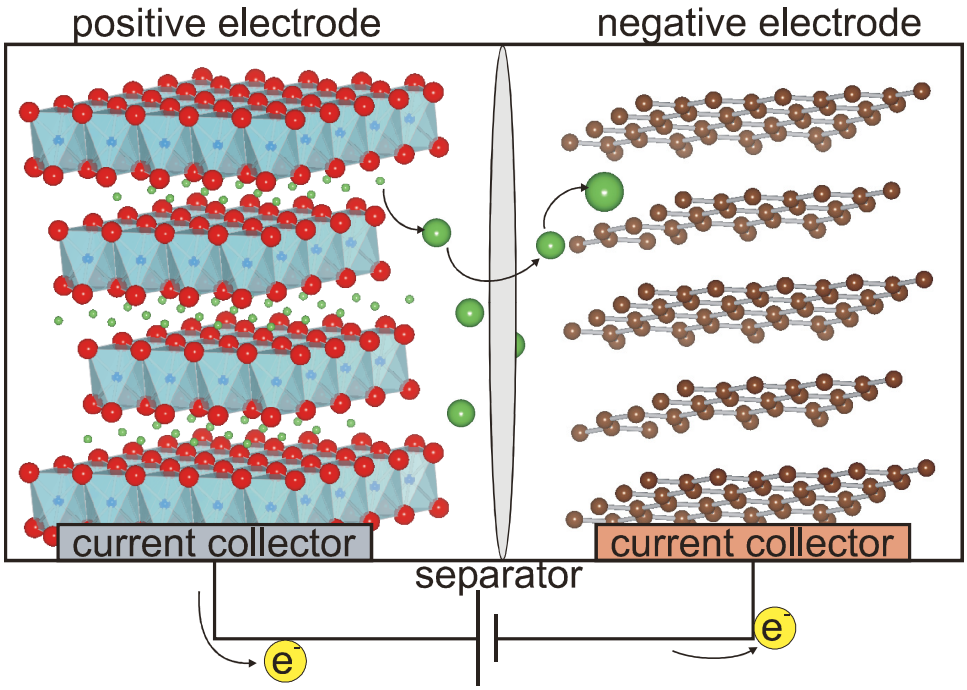

Figure 1.1 A schematic of a commercial graphite/$LiCoO_2$ Li-ion cell in the discharged state just before the start of a charge. Li^+ ions (green spheres) leave the positive electrode material, travel through the porous separator, and intercalate into the negative electrode material. Electrons are simultaneously passed through the external circuit.

As important as the development of the SEI is, a methodical characterization of its growth and thickness is lacking. Although some research groups have studied the formation of SEI, there are very few good in-situ studies.

The aim of this thesis is to quantify the growth of this surface film in real time using spectroscopic ellipsometry (SE). SE can continuously monitor reactions which form a surface film on an electrode, including the growth of a thin SEI layer, using optical methods (as will be discussed in later chapters). Not only is it possible for ellipsometry to measure SEI thickness, but its optical properties as well, which, to the best of our knowledge, have not been reported in great detail. Finally, with this tool, it is possible to characterize the effect of electrolyte additives on SEI growth.

1.1 Thesis Structure

Chapter 2 of this thesis further introduces concepts of Li-ion batteries specific to the present work. These include the electrode materials studied, the importance of the so-called SEI layer during cell cycling and its effects on calendar life predictions, and the usefulness of in-situ measurements.

In Chapter 3, a brief discussion of the background and theory of SE will be presented. These include the mathematical formalism of ellipsometry and the description of a general measurement.

Chapter 4 offers a discussion of some simple theory and operations of other instrumentation used in this thesis, including magnetron sputtering and the in-situ electrochemical cell.

Chapter 5 presents a description of the experimental methodology taken to perform the study in the thesis. This includes sample preparation and testing conditions as well as some simple characterization results of the thin films produced.

Chapter 6 states the results of the project, including SEI thicknesses on various electrode materials, data from the real time optical measurements and the electrochemical data. A discussion of the results will follow and elaborate on key findings.

Chapter 7 concludes this thesis by outlying future work which arises from this project and summarizes the major conclusions involved therein. Here, the value of the measurements obtained by ellipsometry in-situ are discussed.

Chapter 2 Lithium-Ion Batteries

2.1 Introduction to Li-Ion Cells

A Li-ion battery is an electrochemical cell consisting of two electrodes bathed in an ion-conducting electrolyte and separated by an ion-permeable membrane. Figure 2.1 shows a schematic of a Li coin cell, including the electrode materials and separator as well as a stainless steel spacer and disc spring which provide an even pressure distribution throughout the cell. In this arrangement, the cell is able to convert chemical energy to electrical energy and vice versa.

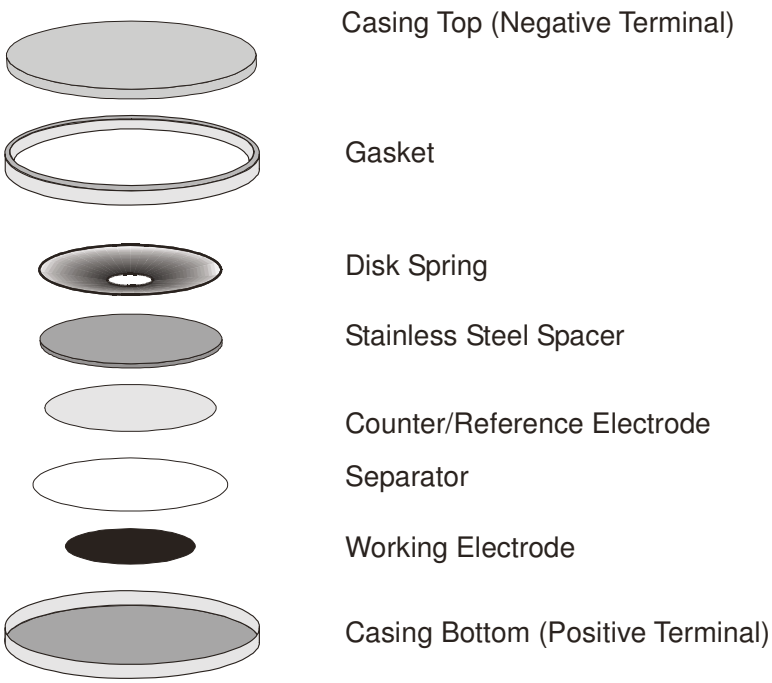

Figure 2.1 Schematic of the interior of a Li-ion coin cell used to study different cell chemistries, cycling behaviour, and more for various electrode materials.

For a typical cell, the positive electrode material is the source of Li^+ ions with which charge can be transferred to the negative electrode (the Li^+ sink) during a charge (these definitions are reversed when dealing with a cell whose negative electrode material is Li-metal). During cell discharge, the flow of ions is reversed, leaving the negative

electrode and migrating towards the positive electrode. In a Li-metal cell (where the negative electrode material is Li-metal), Li-ions exchange at the Li-metal electrode by the chemical reaction

$$\mathrm{xLi^+ + x}e^- \underset{\text{discharge}}{\overset{\text{charge}}{\rightleftharpoons}} \mathrm{xLi} \tag{2.1}$$

where e^- are electrons. Eq. (2.1) is called a "half-reaction" of the negative electrode. A corresponding "half-reaction" occurs at the positive electrode. For example, in a Li/graphite cell, the positive half-reaction is

$$\mathrm{Li_yC} \underset{\text{discharge}}{\overset{\text{charge}}{\rightleftharpoons}} \mathrm{C + yLi^+ + y}e^- \tag{2.2}$$

where C is the carbon atom and y describes the moles of each species present.

The electrons flow through the external circuit and can do work (here, x and y are the number of electrons produced for every x or y atoms of Li). This work is expressed in terms of the change in Gibbs free energy ΔG, given by

$$\Delta G = -n_e F V \tag{2.3}$$

where n_e denotes the number of electrons, F is Faraday's constant, or the charge of 1 mol of electrons (96485 C/mol), and V is the electromotive force (EMF) or voltage of the cell. The net voltage delivered by a Li-ion cell (in Eq. (2.3)) reflects the difference in chemical potential of the Li atoms in the electrode materials through

$$V = -\frac{\mu_{\text{pos}} - \mu_{\text{neg}}}{e} \tag{2.4}$$

where μ_{pos} and μ_{neg} are the chemical potentials of the Li atoms in the positive and negative electrodes, respectively, and e is the charge of an electron (1.602×10^{-19} C). In a Li-ion cell, voltages are referenced to the potential of Li-metal. Typically, negative

electrode materials have a potential which is closer to Li-metal than positive electrode materials. Table 2.1 compares average cell potentials, specific energies, and energy densities of several different commercial battery chemistries [9]. Clearly, Li-ion cell chemistries allow for higher voltage applications and deliver more energy per volume than traditional battery sources.

Table 2.1 Contrasting various commercial cell chemistries available today. Li-ion batteries provide the largest voltage, specific energy, and energy densities among the cell chemistries shown.

Cell Chemistry	Average Voltage (V)	Specific Energy (mWh/g)	Energy Density (mWh/cm^3)
Lead-Acid	2	35	70
Nickel-Cadnium	1.2	40	135
Nickel-Metal-Hydride	1.2	100	235
Lithium-ion (graphite/$LiCoO_2$)	3.8	200	570

The separator material provides a means for ion transport and ensures the electrodes remain spatially separated from one another. The separator is typically a thin, porous membrane made from a polymer and must be compatible with nonaqueous electrolytes. As the topic of battery separators is lengthy, any further discussion would be beyond the scope of this thesis.

The conductive electrolyte mediates ion transport within the cell. Nonaqueous electrolytes, such as those for Li-ion batteries, are made using a Li-containing salt and one or more organic solvents. The most common Li-salt used is $LiPF_6$. A good Li-salt for Li-ion electrolytes must have a high conductivity, a high Li^+ transference number, acceptable safety properties, and be moderately inexpensive. $LiPF_6$ meets these requirements, though it is modestly expensive and can aid in the formation of HF from H_2O contamination within the cell. This can lead to destruction of the electrode materials and other cell components leading to cell failure. Just as there are numerous Li-salts for nonaqueous electrolytes, there are many organic solvents available. Further discussion of nonaqueous electrolytes will be given in later sections.

A new electrode material can be studied by making a cell with the electrode material and Li-metal. By cycling a Li-metal cell (commonly referred to as a "half cell"), complicated side reactions with other electrode materials can be avoided. Performing these types of studies on both positive and negative electrode materials can be used to predict the cycling behaviour of a cell made with both positive and negative electrode materials (i.e., without Li-metal).

In a cycling experiment, a current is applied to a cell and the cell's voltage is measured. From the known current, the time, and other properties of the electrode material (mass, theoretical capacity, etc.) a plot of voltage versus specific capacity can be made. The specific capacity of a cell defines the amount of charge which can be stored per unit mass of electrode material (units of mAh/g). The theoretical capacity of a material is the maximum amount of charge stored in the material. The theoretical capacity is typically calculated by modeling the intercalation of Li within a host material. For example, the theoretical capacity of graphite is 372 mAh/g whereas the theoretical capacity of $LiCoO_2$ is 155 mAh/g [10]. A plot of voltage versus capacity yields further information about the cell such as reversible and irreversible capacities (RC and IRC, respectively) and charge and discharge capacities. A cell's RC is the amount of charge which can be stored/extracted without loss. The IRC is the capacity which is lost during cell cycling due to surface reactions to form the SEI at both the positive and negative electrodes.

Figure 2.2 shows cycling curves for the first cycle of a graphite negative electrode and a $LiCoO_2$ positive electrode both cycled against Li-metal in the same electrolyte (1 M $LiPF_6$ in a 1:2 ratio of ethylene carbonate (EC):diethyl carbonate (DEC)). Losses due to the IRC can be observed for each curve. These are most prominent during the first full discharge/charge cycle and are labeled in Figure 2.2 for the Li/graphite cell. For the graphite electrode, ~56 mAh/g of capacity is lost in the first cycle due to the formation of the SEI which parasitically removes usable Li from the cell in its formation. Similarly, an IRC of ~9 mAh/g is observed for the $LiCoO_2$ electrode. In Figure 2.2, the RC of the graphite electrode is indicated. The voltage of a graphite/$LiCoO_2$ cell would merely be the difference in potential between the positive and negative electrodes as indicated by the vertical line in Figure 2.2.

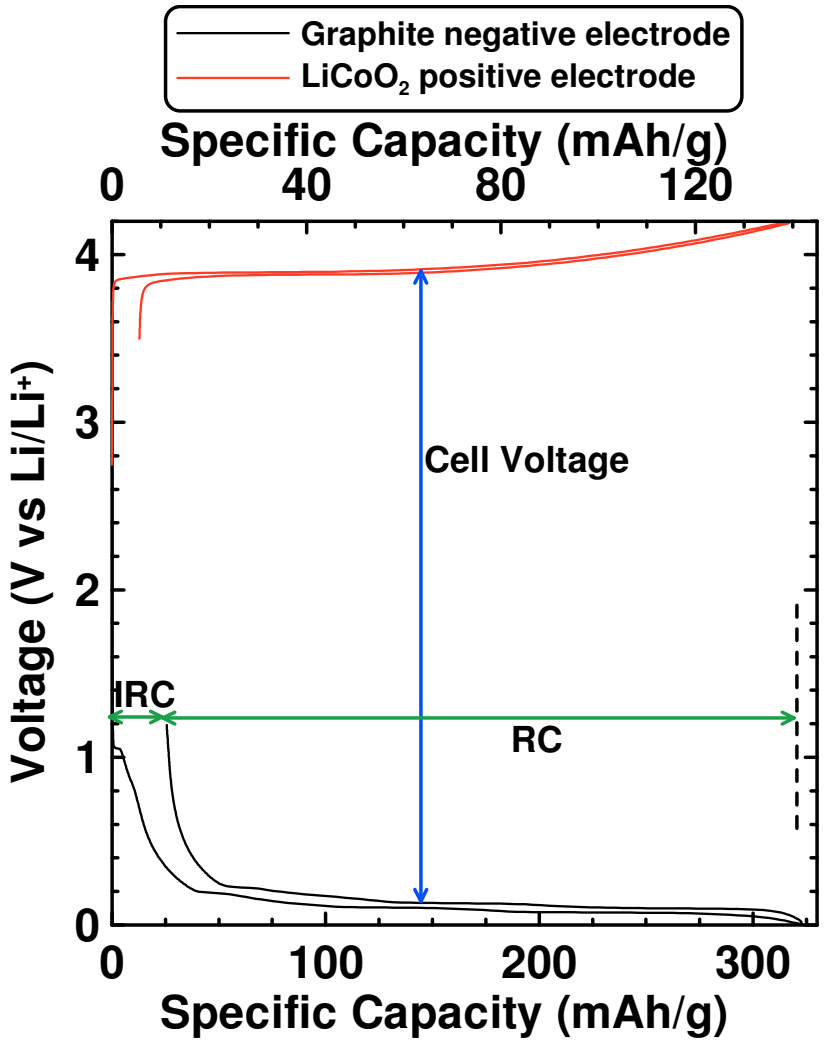

Figure 2.2 Voltage curves for Li/graphite and Li/$LiCoO_2$ cells cycled in the same electrolyte (1 M $LiPF_6$/EC:DEC(1:2)). Horizontal lines indicate the irreversible capacity (IRC) and the reversible capacity (RC) or the Li/graphite cell. The vertical line predicts the net cell voltage of the combined graphite/$LiCoO_2$ Li-ion cell. (Data courtesy of J.C. Burns).

Various electrode materials behave differently when they react with lithium. Li-ions can enter into an electrode material's structure via several routes: intercalation, alloying, or displacement, for example. Intercalation is the reversible insertion of a guest species into open sites within a host material. For example, a graphite negative electrode is composed of structured layers of graphene. Li-ions can intercalate/deintercalate between the layers during a discharge/charge of a Li/graphite cell. Intercalation materials are very common Li-ion battery materials. These include the positive electrode materials $LiCoO_2$, $LiNi_{(1-x-y)}Mn_xCo_yO_2$ (NMC), and $LiMn_2O_4$ (spinel) and the negative electrode

materials graphite and $Li_{4/3}Ti_{5/3}O_4$. Alloy materials are those which do not intercalate Li into their structure; rather, Li guest atoms form an alloy with the host material. During the alloying process, the volume of the material expands markedly due to the insertion of Li. There are several key examples of electrode negative materials which undergo alloying with Li-ions, including Si, Sn, and Al which form $Li_{3.75}Si$, $Li_{4.4}Sn$, and LiAl when fully lithiated, respectively. Another lithiation mechanism is by displacement. Here, Li can displace oxygen in a metal oxide electrode material to form Li_2O and the metal.

In this thesis, two electrochemical measurements were used to test Li cells: galvanostatic chronopotentiometry and potentiostatic chronoamperometry. In a galvanostatic chronopotentiometry measurement, the current is controlled and the resultant cell voltage is measured. In Figure 2.2, both electrodes were studied using this method. Galvanostatic chronopotentiometry is useful to determine charge/discharge capacities, IRC, and lithiation behaviour (how Li and host material interact) of an electrode material. Potentiostatic chronoamperometry is a measurement of the cell's current with time as the voltage is fixed. These measurements are useful to determine the total amount of charge transferred to the cell. Figure 2.3 shows data from a potentiostatic chronoamperometry measurement for a Li/TiN cell. In Figure 2.3, the voltage was fixed at 0.5 V and the current was measured. The curve is negative in current because the voltage is being stepped from open-circuit (~3.1 V) to 0.5 V. The charge, Q, transferred to the TiN electrode can be calculated by integrating the measured current, I, during a time, t, as

$$Q = \int dt \cdot \mathrm{I}. \tag{2.5}$$

Equation (2.5) has been used in Figure 2.3 to calculate the charge transfered and is represented as the shaded area under the curve.

Though both galvanostatic chronopotentiometry and potentiostatic chronoamperometry are useful in determining the electrochemical characteristics of Li-ion systems in real time, they do not determine the physical surface chemistry of the electrodes (however, this can be inferred indirectly such as in Ref. [8]). To study the

surface of an electrode at a specific state of charge, one would cycle a cell, carefully disassemble it, rinse the electrode with a solvent, let it dry, and then perform measurements on the electrode of interest under vacuum or inert gas. This is an ex-situ measurement and is useful for studying stable materials. Ideally, one wishes to examine surface reactions as the cell cycles in real time or in-situ. However, in-situ measurements typically require new cell hardware. These cells must be designed with the characterization equipment in mind. For example, Refs. [11-14] show the experimental details involved with using these in-situ-type electrochemical cells.

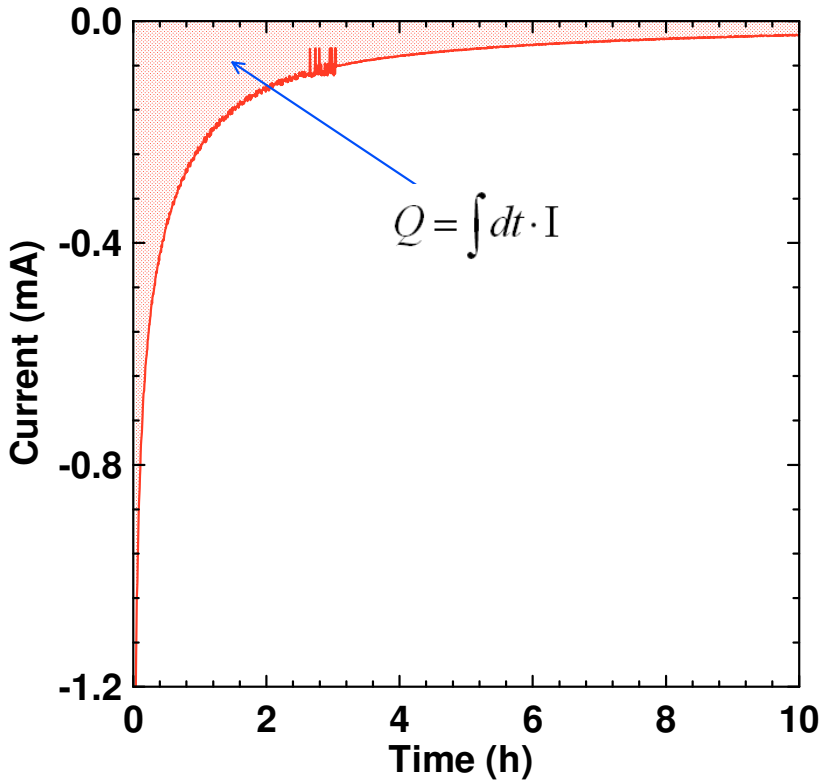

Figure 2.3 Potentiostatic chronoamperometry study on a Li/TiN cell in 1 M $LiPF_6$/EC:DEC(1:2) held at 0.5 V at 22ºC. The charge delivered to the TiN electrode is determined by integrating the current over the temporal range. The fraction of the charge that flows to the working electrode (i.e. not the vacuum fittings, etc.) is entirely associated with surface film formation.

In this thesis, the working electrode of a Li/working electrode cell was probed in-situ using spectroscopic ellipsometry (SE) during electrochemical testing. SE probes a surface using a beam of light (this will be discussed in further detail in Chapter 3).

Therefore, an in-situ cell which allows light to impinge and reflect from the electrode surface is required. The in-situ cell design will be presented in Chapter 4, but for now, it is sufficient to describe the cell as a clear quartz tube inside of which a negative electrode, a positive electrode, and electrolyte can be placed. With SE and the in-situ cell, any surface reactions occurring on the working electrode can be monitored during galvanostatic chronopotentiometry or potentiostatic chronoamperometry measurements.

2.2 Negative Electrode Materials

Graphite is a common negative electrode material for Li-ion batteries. One typically compares the performance of negative electrode materials to graphite as this is the current industry standard (and hence the best understood). Graphite is an intercalation material which can accommodate a single Li atom per 6 C's (LiC_6) at full lithiation which leads to a specific capacity of 372 mAh/g [15]. Also, as an intercalation material, graphite only expands roughly 10% of its original volume at full lithiation [16]. Alloy materials, however, have been found to exhibit both larger specific capacities and volume expansions than graphite. Figure 2.4 shows the specific capacities of various negative electrode materials (adapted from Ref. [16]). Si has the highest specific capacity of the alloy materials. However, Si, as well as other alloy materials, experiences a huge volume expansion of 280% from its unlithiated state [17] making it undesirable as a negative electrode material on its own. As delithiation occurs, the electrode undergoes extreme motions decreasing its volume. These motions cause a loss of contact between the active electrode material and the foil current collector. It is this loss of contact which can cause the large capacity fade observed in some cells with Si negative electrodes and ultimately ends in cell failure [18].

At room temperature, Ni and TiN do not alloy with Li. As such, these materials would not be suitable candidates to replace either Si or graphite. However, such "lithium-inert" materials are great for method development and fundamental understanding of events occurring within a cell. Moreover, Baggetto et al. have described the use of barrier material coatings for use in 3-dimensional all-solid-state Li-ion batteries which act as an electronically conductive layer capable of blocking lithium

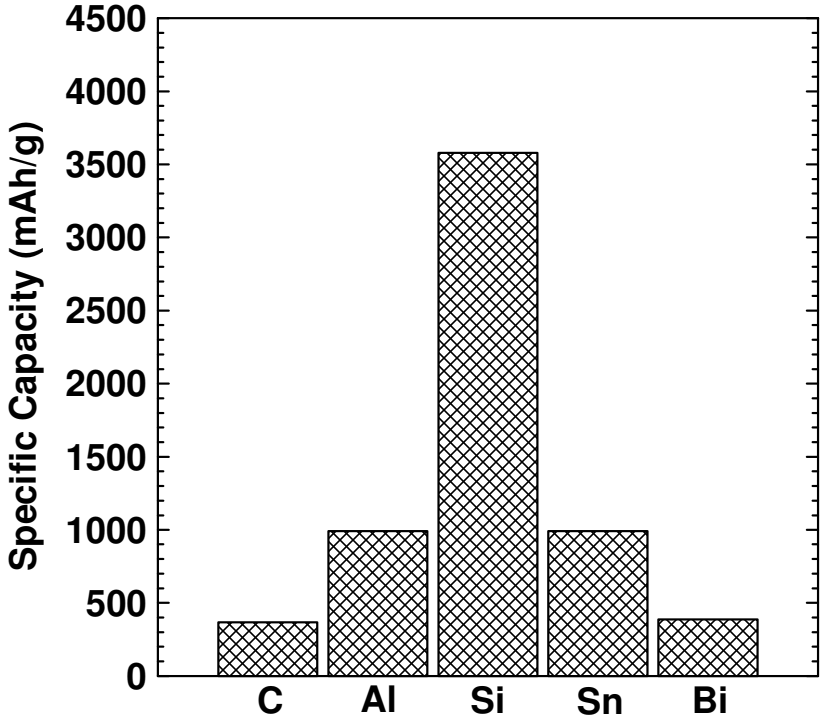

Figure 2.4 Graphical comparison of specific capacities of negative electrode alloy materials vs graphite. (Adapted from Ref. [16]).

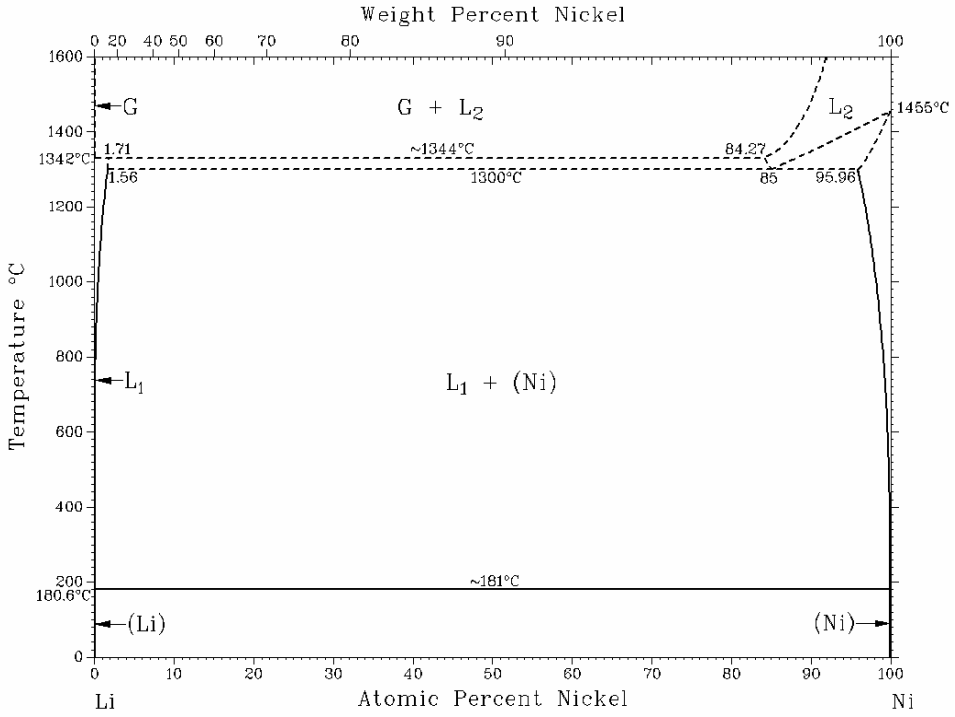

Figure 2.5 Equilibrium Li-Ni phase diagram. Until roughly 181ºC, there is no alloying between the species, making Ni a good material to inhibit lithiation.

species from reacting with the active electrode materials [19-21]. In these publications, Baggetto et al. describe the use of non-alloying metal nitrides (MN_x) which undergo a conversion reaction whereby the N in MN_x reacts irreversibly with Li to form Li_3N [22] following

$$MN_x + 3xLi \rightarrow M + xLi_3N \tag{2.6}$$

For a TiN-containing thin film, Baggetto et al. showed through cyclic voltammetry that only 0.02 Li per TiN formula unit can be reversibly inserted into or extracted from the TiN structure due to the very poor kinetics or the unfavourable thermodynamics between TiN and Li. Similar to TiN, Ni does not alloy with Li and thus would have similar properties and applications as TiN. Figure 2.5 shows the equilibrium Li-Ni phase diagram. At room temperature, there are no intermetallic phases observed between the two elements. TiN and Ni are useful for developing the methodology in this thesis. Specifically, the reduction and decomposition of electrolyte species are still observed using SE to form the SEI.

2.3 The Solid Electrolyte Interphase Model

During the cycling of a Li-ion cell, the electrolyte reacts on the negative electrode surface and reacts to form a passivating layer. This layer, coined by Peled in 1979 as the solid electrolyte interphase (SEI) [1], is very important to the cycling characteristics of a Li-ion cell. The SEI is conductive to Li^+ ions yet electronically insulating. Once formed, the SEI almost entirely prevents reactions between intercalated Li and the electrolyte. The SEI forms as a thick porous layer during the first cycle and continues to grow during subsequent cycles [1]. The rate at which SEI grows is increased at elevated temperatures – this is characteristic of films grown during chemical reactions. Studies of the chemical composition of the SEI on Li-metal and carbon electrode materials have been performed. The SEI has been shown to include LiF, Li_2CO_3, Li_2O, lithium alkoxides, lithium alkyl carbonates, nonconductive polymers and other electrolyte reaction products [23-27]. As

some of these insoluble reaction products are unstable, physical characterization of the SEI ex-situ is difficult. Thus, in-situ measurements are essential to understand the SEI. Figure 2.6 shows a schematic of the SEI model developed by Peled [2]. In Peled's model, the SEI is depicted as a porous film of Li-containing particles such as LiF, Li_2CO_3, etc. on the electrode surface. The grain boundaries of the particles play an important role in ion diffusion through the SEI and contribute to the overall resistance of the layer [1]. In Li-ion cells, the SEI is the cause of the IRC loss observed in the first cycle [2].

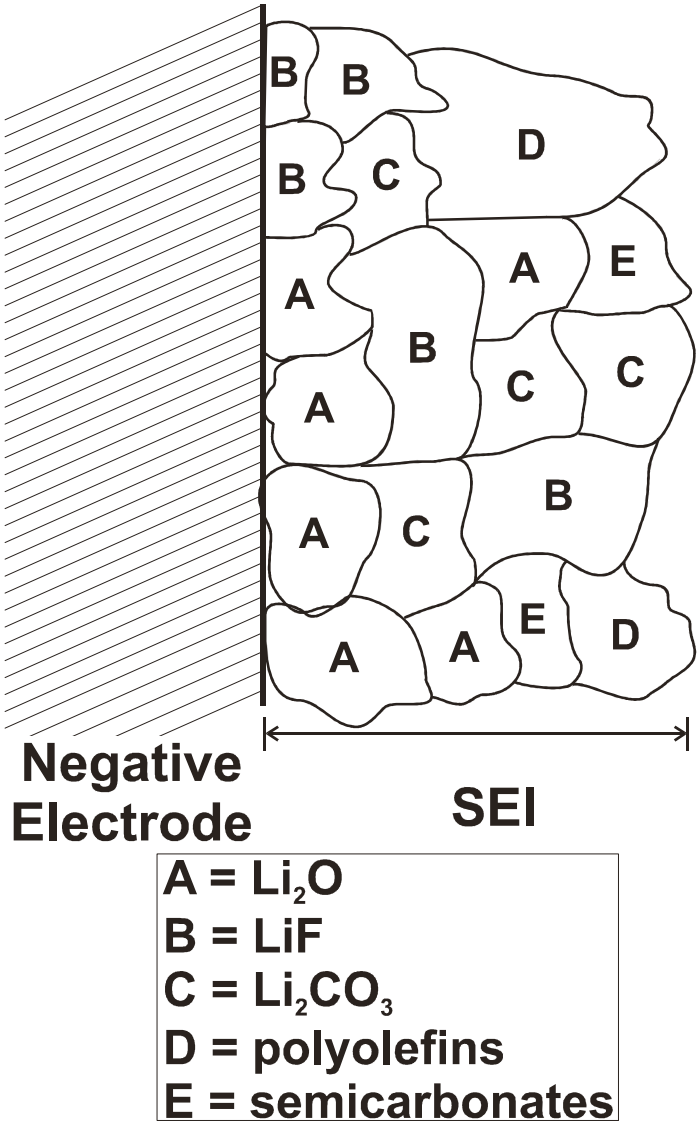

Figure 2.6 Schematic of the SEI developed on a negative electrode. Letters indicate the SEI species as described in the legend. (Adapted from [2]).

2.3.1 Modeling the SEI

There are several models proposed in the literature which deal with the growth of the SEI layer. Recently, Smith et al. have developed a simple model for SEI growth based on similar arguments to the growth of oxides on metals put forward by Lawless [28]. Just as a metal exposed to air forms a passivating oxide that reduces the rate of any further reaction, Smith et al. proposed that a lithiated negative electrode material (such as graphite/Si/etc.) reacts to form an analogous SEI. In the review by Lawless, many rate laws were considered; however, the simplest among them was chosen and tested by Smith et al. This is the parabolic growth law, which assumes that the rate of increase in SEI thickness, x_{SEI}, is inversely proportional to the thickness of the layer, that is,

$$\frac{dx_{\mathrm{SEI}}}{dt} = \frac{c_0}{x_{\mathrm{SEI}}} \tag{2.7}$$

where c_0 is a constant of proportionality. Equation 2.7 is in the form of a separable differential equation which can be solved through the integration of

$$\int dx_{\mathrm{SEI}} \cdot x_{\mathrm{SEI}} = \int dt \cdot c_0 \tag{2.8}$$

whose solution is

$$\tfrac{1}{2} x_{\mathrm{SEI}}^2 = c_0 t + c_1 \tag{2.9}$$

with integration constant c_1. If it is assumed that there is no SEI growth as soon as the cell is constructed, then $x_{\mathrm{SEI}} = 0$ at $t = 0$. Under this assumption, the integration constant becomes 0 and thus

$$x_{\mathrm{SEI}} = (2c_0)^{\frac{1}{2}} \cdot t^{\frac{1}{2}} \tag{2.10}$$

Eq. (2.10) states that the thickness of the passivation layer on the surface of the electrode varies as the square-root of time. Hence, there is very little to no contribution to SEI thickness from the way a Li-ion cell is cycled, but instead, is controlled by time alone at fixed potential. One can gather further information about the growth rate of the SEI by examining the time-derivative of Eq. (2.10), given by

$$\frac{dx_{\mathrm{SEI}}}{dt} = (\tfrac{1}{2} c_0)^{\frac{1}{2}} \cdot t^{-\frac{1}{2}}. \tag{2.11}$$

Thus, the rate in change of the SEI thickness is related to the inverse of the square-root of time. Eqs. (2.10) and (2.11) describe the thickness and growth rate of the SEI versus time for an electrode against Li.

In a model proposed by Ploehn et al. [7], it was proposed that the SEI growth and formation are due in part to the diffusion of the organic solvents present in the electrolyte through the SEI. In the solvent diffusion model, it was assumed that the solvent S underwent a two-electron reduction with Li^+ ions to form an insoluble product P such that

$$\mathrm{S} + 2e^- + 2\mathrm{Li}^+ \rightarrow \mathrm{P}. \tag{2.12}$$

The molar densities of the solvent and product were assumed to be constant and given by c_S and c_P, respectively. As S is dilute within the SEI, it was assumed that $c_S \ll c_P$. The only mobile phase in the model is S which has an effective diffusivity constant D_S in the SEI layer. Figure 2.7 shows the geometry considered for the model. In the model, the SEI/electrolyte interface was taken as the origin (spatial coordinate $z = 0$) and z increased positively towards the electrode.

To test the validity of the model, Ploehn et al. applied it to results of a year-long study by Broussely et al. [29] on Li-ion cells with graphite negative electrodes held in the fully charged state. It was assumed that all S was in the form of ethylene carbonate (EC) as it was the most reactive solvent species present and that all P represented Li_2CO_3 on the electrode surface.

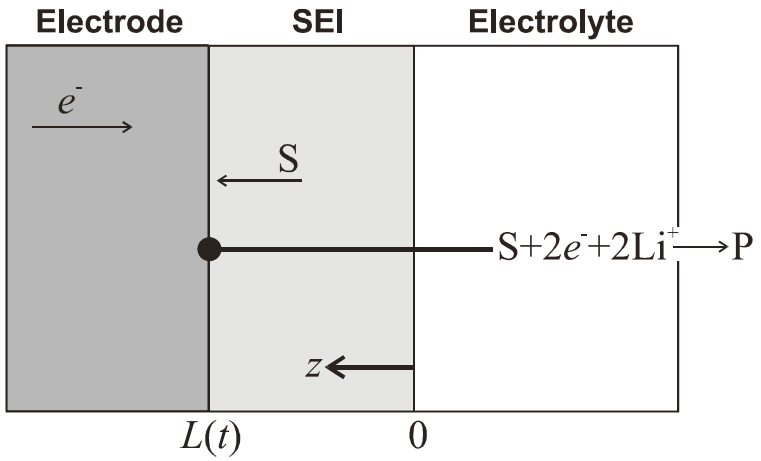

Figure 2.7 Schematic representation of the solvent diffusion model for determining the growth of the SEI on negative electrode materials. Spatial coordinate z was used as the origin at the SEI/electrolyte interface and extended positively towards the electrode. S, Li^+, P, e^-, and $L(t)$ represent the solvent phase, Li-ion, insoluble product (SEI), electrons, and the physical extension of the SEI, respectively. (Adapted from Ref. [7]).

Assuming diffusion described by Fick's law, Ploehn et al. concluded that the diffusion of EC through the SEI was governed by

$$\frac{\partial c_S}{\partial t} = D_S \frac{\partial^2 c_S}{\partial z^2} \tag{2.13}$$

with respective boundary conditions at the electrode/SEI and SEI/electrolyte interfaces

$$z = L(t); \qquad c_S \approx 0 \tag{2.14a}$$

and

$$z = 0; \qquad c_S = c_{eq} \tag{2.14b}$$

In words, the boundary condition outlined by Eq. (2.14a) indicates that all S which diffuses through the SEI is consumed by the electrode/SEI interface. A local equilibrium is established at the SEI/electrolyte interface whose molar density is similar to c_S. Together, Eqs. (2.13), (2.14a), and (2.14b) can be solved in a similar fashion to the

oxidation of Si (as described in Ref. [30]). By applying the change of variables (through dimensional analysis), one can attain

$$u \equiv \frac{z}{\left(4D_{\mathrm{S}}\right)^{\frac{1}{2}}\left(t\right)^{\frac{1}{2}}} \tag{2.15}$$

Substitution of Eq. (2.15) into (2.13) yields

$$\frac{d^2 c_{\mathrm{S}}}{du^2} + 2u\frac{dc_{\mathrm{S}}}{du} = 0 \tag{2.16}$$

with the modified boundary conditions (from Eqs. (2.14a) and (2.14b))

$$u = \zeta; \qquad c_{\mathrm{S}} \approx 0 \tag{2.17a}$$

and

$$u = 0; \qquad c_{\mathrm{S}} = c_{\mathrm{eq}} \tag{2.17b}$$

where ζ can be expressed as

$$\zeta = \frac{L\left(t\right)}{\left(4D_{\mathrm{S}}\right)^{\frac{1}{2}}\left(t\right)^{\frac{1}{2}}} \tag{2.18}$$

From Eq. (2.18), it is simple to show that the SEI thickness is

$$L\left(t\right) = 2\zeta\left(D_{\mathrm{S}}\right)^{\frac{1}{2}}\left(t\right)^{\frac{1}{2}} \tag{2.19}$$

where ζ can be expressed as a complicated function in terms of error functions, the mathematics of which are beyond the scope of this thesis.

2.3.2 Measuring Physical Properties of the SEI

Several research groups have proposed techniques for measuring the thickness and composition of the SEI on negative electrode materials [24, 31-43]. However, nontrivial methods must be devised as the species forming the SEI are unstable/air sensitive. As such, it is challenging to perform thickness/surface measurements on the SEI. This section will discuss the development of in-situ techniques for studying the SEI layer and will introduce the technique used in this thesis.

One of the simplest techniques used to study SEI film formation is electrochemical impedance spectroscopy (EIS), whereby the impedance of a Li-ion cell is measured continuously during cycling. This technique has been employed to determine the resistive and capacitive properties as well as the formation reaction kinetics of the SEI on various electrode materials using different electrolytes [2, 23, 34, 39, 40]. These measurements are simple relative to other more exotic techniques as EIS can be performed simultaneously with traditional galvanostatic and/or potentiostatic measurements. A large issue of the validity of EIS measurements is the analyses of the data. From a Nyquist plot of the impedance of an electrode, for example, one must construct an equivalent circuit model reflecting its resistive and capacitive properties. The model may contain many variable parameters to match the recorded data. One could continually introduce new elements into the model until a perfect fit is achieved. This analysis can lead to unphysical results. However, EIS can yield thickness information of the SEI by modeling its capacitive properties provided the user has a keen understanding of the technique.

X-ray photoelectron spectroscopy (XPS) is a technique able to quantify the species on the surface of a sample. This technique is well known and has provided accurate information about the surface chemistry of the SEI. As well, XPS can provide depth profiles of the surface constituents by sputtering away surface layers one at a time. These measurements must be done ex-situ as a drying step is required for the electrodes as measurement is performed under ultra-high vacuum. XPS has been successful in determining the surface chemistry of the SEI formed on graphitic and lithium metal electrodes with various electrolytes [26, 33, 44].

In this thesis, formalism is adopted to describe electrolytes and additives used in battery testing. Electrolytes will be described as: X M (salt)/(solvent)/(additive) where X is the concentration of Li-salt dissolved in the solvent, (salt) is the Li-containing conductive salt, (solvent) is the solvent used in the electrolyte, and (additive) represents any additives used. For example, the electrolyte 1 M $LiPF_6$/elthylene carbonate (EC):diethyl carbonate (DEC) (1:2)/2 wt.% fluoroethylene carbonate (FEC) has 1 M of $LiPF_6$ dissolved in a 1:2 ratio of EC:DEC with 2% by weight FEC.

Kanamura et al. established the composition of the SEI using XPS in various electrolytes [26]. In the study, Li was electrodeposited onto Ni electrodes at 1.0 mA/cm^2 until the total charge passed was 0.667 mAh/cm^2 in electrolytes of 1 M $LiClO_4$, $LiAsF_6$, $LiBF_4$, and $LiPF_6$ in either γ-butyrolactone (γ-BL) or tetrahydrofuran (THF). The electrodes were washed with the solvent and dried under vacuum and placed into the XPS chamber. SEI species were found to be similar with all electrolytes (depending on the halide present, the SEI would have some fluorine or chlorine component appearing as LiF or LiCl). It was shown from depth profiling that the SEI formed on the electrodes was thinner when $LiPF_6$ was present in the electrolyte. Hydrocarbons, LiOH, Li_2CO_3 and Li_2O as well as LiF and LiCl (if the salt was F- or Cl-containing) were found to be the major compounds forming the SEI.

In another study by Peled et al. [33], XPS measurements were performed on highly ordered pyrolitic graphite (HOPG) electrodes in a Li/HOPG cell in a 1 M $LiPF_6$/EC:DEC (1:1) electrolyte. The cells were discharged to 0.1 V, charged to 2.5 V and disassembled. The HOPG electrodes were washed with dimethyl carbonate (DMC) and vacuum dried prior to XPS measurements. Both the cross-section and basal plane of the HOPG electrodes were sampled for SEI measurements. From depth profiling, it was found that roughly 90 at.% of the bulk SEI consisted of LiF in the cross-section. The rest of the species appeared as polymers, LiOC groups (from alkoxides), and Li_2O. Li_2CO_3 was not observed in either the bulk nor the solution exposed side of the electrode. For the basal plane, about 10-30 at.% of Li_2CO_3 was observed on the surface and in the bulk of the SEI (from depth profiling). The basal plane also contained much less LiF and much more polymeric material (~50 at.% at the surface) than the HOPG cross-section. From this, Peled et al. concluded that the greatest contribution to SEI formation on the basal

plane is solvent reduction, whereas on the cross-section, it is the reduction of electrolyte anions. Alkoxides and Li_2O were also present in the bulk and the HOPG/SEI interface of the basal SEI. From depth-profiling analysis, the basal SEI was estimated to be ~2 nm thick, whereas the cross-sectional SEI was ~30 nm thick. Peled et al. concluded that the SEI of the cross-section was thicker than the basal SEI.

In-situ techniques have also been used to study the growth of the SEI on various electrodes. Typically, however, in-situ measurements are more difficult than ex-situ measurements as they require a novel cell design to allow probing of the electrode surface. In a study by Santner et al., Fourier transform infrared spectroscopy (FTIR) was used to study the surface of a glassy carbon electrode in a Li/carbon cell in-situ [35]. Using electrolytes of 0.5 M $LiClO_4$/propylene carbonate (PC) and 0.5 M $LiClO_4$/THF, the effects of electrolyte additives on SEI formation were studied. These additives were vinyl acetate (VA) and acrylonitrile (AN); they were added to the electrolytes at concentrations of 10% by volume. These additives, referred to as vinylene additives, contain a single vinylene group. An in-situ cell was constructed in which the probing infrared beam could impinge on the glassy carbon electrode while cyclic voltammetry measurements were simultaneously performed. It was found that in each electrolyte, the vinylene additive reduced on the surface of the glassy carbon electrode. The reduction potentials for AN and VA additives were ~1200 mV and ~1.1 V, respectively. The vinylene additives initiated the electrolyte reduction in all cases considered. Unfortunately, in-situ FTIR was unable to resolve the reduction of other electrolyte species such as $LiClO_4$, THF, or PC on the electrode surface. From the work of Santner et al., it was concluded that the initial reduction of the vinylene additives promoted the growth of a "better" SEI by forming either polymeric nuclei on which further SEI products grow or a polymeric network which reinforces the adherence and retention of the SEI at the electrode surface.

In-situ atomic force microscopy (AFM) measurements have also been performed to study the surface morphology of the SEI during cell storage [32]. In a study by Inaba et al., HOPG electrodes were studied in a Li/HOPG in-situ AFM cell at different temperatures. In the study, 1 M $LiClO_4$/EC and 1 M $LiClO_4$/EC/3 wt.% vinylene carbonate (VC) was used as the electrolyte. Cell cycling was performed using cyclic

voltammetry. After one complete discharge/charge cycle between 2.9 V and 0.05 V (vs Li/Li^+) at 30ºC to form an SEI, an AFM measurement of SEI layer thickness was performed. Afterwards, the cell was held at 2.9 V or 0.05 V at 45ºC, 60ºC, or 80ºC for 12 hours, cooled to 30ºC and another AFM measurement was performed. A dense SEI layer of 16 nm in thickness was observed at 2.9 V after a complete discharge/charge cycle. After holding at 2.9 V for 12 hours at 45ºC, 60ºC, and 80ºC, a porous and grained SEI film was formed with a thickness of 30 nm, 50 nm, and 10 nm, respectively. At 2.9 V, the electrolyte should not reduce on the electrode surface. Thus, Inaba et al. suggests that the apparent increase in SEI thickness at elevated temperatures is due to a partial dissolution of SEI species back into the electrolyte. After a hold at 0.05 V for 12 hours at 30ºC, the same dense, stable 16 nm SEI layer remained. Inaba et al. did not observe any appreciable thickness increase during the hold period. After a 12 hour hold at 60ºC, however, the SEI grew to 160 nm. It was concluded that the SEI did not work effectively as a barrier to further solvent penetration which allowed the SEI to swell. With the addition of VC, an SEI of 20 nm was formed at 2.9 V at 30ºC. After a 12 hour hold at 60ºC, the SEI consisted of very fine particles and did not increase in thickness appreciably. Similarly, at 0.05 V, the SEI layer thickness was 20 nm at 30ºC and increased to only 25 nm after a 12 hour hold at 60ºC. Inaba et al. concluded that the presence of VC in electrolytes for the Li/HOPG system dramatically improved the formation of SEI. With the availability of VC, the SEI formed on HOPG electrodes was very dense and did not allow solvent molecules to penetrate into the electrode surface. This yielded superior charge/discharge characteristics of Li/HOPG cells cycled at elevated temperatures. In other work done on cycling Li/graphite cells with VC additives by Xiong et al., a large IRC was observed [45]. The increased IRC of a cell, due to the formation of the SEI, indicates that a thick SEI is grown. These results agree with the findings of Inaba et al.

There have been several studies of the optical characteristics and thickness of the SEI performed by McLarnon's group using spectroscopic ellipsometry (SE) [41-43]. Spectroscopic ellipsometry is a powerful optical technique used to characterize thin film growth and excels at in-situ measurements. In this thesis, SE will be used to detect and

measure the change in thickness of the SEI during electrochemical measurements. Using SE, the effect of electrolyte additives on the SEI's thickness can be studied.

2.4 Electrolytes and Additives for Li-Ion Batteries

This chapter concludes with a brief review of electrolytes, their additives and their effects on the performance of a Li-ion cell and the formation of the SEI. The information given in this section has been adapted from two excellent review articles by Zhang [46] and Xu [47].

The electrolyte used in Li-ion batteries functions as a medium for ion exchange between the two electrodes. It is worth discussing some properties of electrolytes used in Li-ion batteries as it is important in the formation of the SEI layer. The main requirements of an electrolyte for use in a Li-ion cell are as follows:

1. it should be a good ionic conductor and electronic insulator (improves ion transfer and ensures self-discharge remains a minimum),
2. it should operate over a wide potential range such that very little electrolyte decomposition occurs,
3. it should be inert to other cell components such as the cell casing, separator materials, etc.,
4. it should be mechanically, electrically, and thermally stable under abusive conditions, and
5. it should be environmentally safe.

Electrolytes are made by dissolving a Li-salt into one or more nonaqueous (more appropriately termed, aprotic) organic solvents. For the electrochemical work in this thesis, 0.1 M and 1 M $LiPF_6$/EC:DEC(1:2)/Y (where Y stands for any additives present) electrolyte was used.

A good Li-salt for electrolytes has several important requirements. The salt should be able to completely dissolve and dissociate in aprotic solvents and its associated ions should have a high mobility, especially Li^+. The anion of the salt should be stable against oxidative decomposition at high potentials near the positive electrode material. The anion should be relatively inert to the solvent and both the anion and cation should be inert to other cell components, such as cell casings, separators, etc. Table 2.2 lists some of the more popular Li-salts for Li-ion battery electrolytes. Of the available salts, only $LiPF_6$ adequately meets the requirements listed above. $LiPF_6$ does not excel at any one thing; instead, $LiPF_6$ became the commercial salt due to a balance of its physical properties.

Table 2.2 List of physical properties of several common salts for Li-ion batteries.

Salt	Molecular Weight (g/mol)	Melting Temperature (ºC)	Conductivity (1.0 M, 25ºC) (mS/cm) in EC:DMC
$LiBF_4$	93.9	293	4.9
$LiPF_6$	151.9	200	10.7
$LiAsF_6$	195.9	340	11.1
$LiClO_4$	106.4	236	8.4
$LiN(CF_3SO_2)_2$	286.9	234	9

Similarly, good electrolyte solvents also have key requirements which enable good Li-ion cell performance. A good solvent should dissolve salts to a sufficient concentration (these typically have a high dielectric constant). The solvent should have a low viscosity to improve ion transport, and it should be inert to other cell components. Finally, a good solvent should remain a liquid over a wide temperature range. Ethylene carbonate (EC) is well known as one of the best electrolyte solvents and has since been commercialized as such. Unfortunately, EC has a high melting point (~36ºC) and is therefore a solid at room temperature. However, EC can be dissolved in any ratio in linear carbonates, such as diethyl carbonate (DEC). The resultant solution delivers a high solvation power of EC towards Li-salts, offers high anodic stability of EC on positive electrode surfaces, and benefits from the low viscosity of DEC to promote ion transport.

As such, this solvent combination has been used in Li-ion batteries, although similar linear carbonates such as dimethyl carbonate (DMC) can be substituted for DEC.

Unmodified electrolyte decomposes on the negative electrode to form the SEI layer, predominantly during the first charge/discharge cycle. The SEI is typically porous and if it is disturbed (cracked, punctured, etc.), it will irreversibly consume more Li to repair itself. As the SEI is very important in predicting calendar life and ultimately capacity fade and cell death, much research has gone into making a better SEI in terms of its compactness and impedance. Typically, additives can be included in the electrolyte to modify the SEI. These additives facilitate formation of the SEI on the negative electrode surface and reduce the IRC and gas generation during long-term cycling. In general, electrolyte additives have high reduction potentials such that they will react on the anode during the first cycle before other electrolyte species to modify the SEI. For example, vinylene carbonate (VC) and fluoroethylene carbonate (FEC) are believed to reduce on the negative electrode first, thus producing a stable thin film on which electrolyte species can reduce and form a more stable SEI [46]. Moreover, FEC has been shown to improve IRC loss for Si negative electrode materials [48]. It is postulated that FEC allows for a "springy" SEI which holds together during the huge volume expansion experienced by the Li-Si alloying/dealloying process. Clearly, research on additives is an important aspect to improve Li-ion batteries. However, the use of additives in Li-ion cells is commercially unregulated and information is, for the most part, proprietary. This makes their study nontrivial and further work is required to understand which additive works the "best" for the cell chemistries under study.

Chapter 3 Background and Theory of Spectroscopic Ellipsometry

3.1 History and Development

Optical measurements were performed ever since the discovery of the lens for use as a scientific tool. Like the lens, the theory behind ellipsometry has been known for two centuries [49, 50]. The history of ellipsometry begins in 1669 with the discovery of double refraction of light beams by Erasmus Bartholinus as he studied the properties of a transparent crystal of calcite ($CaCO_3$) [51]. What Bartholinus was actually observing was the polarizability of light, which was studied in greater detail by Huyghens in 1690 [52]. This basic property of light would later serve as the crux of all ellipsometry (and most reflectance) measurements.

During the early 1800s, three major discoveries were made which helped shape modern optics. In 1808, Malus discovered that sunlight, reflected from a glass pane could be polarized [53, 54]. Malus conducted several tests to determine the degree of polarization by varying the incident angle of light on the pane. Prior to 1821, Fresnel was researching the wave-like behaviour of light, describing it as the transverse luminous vibrations from the ether medium [55]. While studying, Fresnel was able to derive the reflection and transmission coefficients for monochromatic light at an interface of two unlike dielectric media. Moreover, Fresnel was able to identify the two components which define a beam of linearly polarized light incident on a surface at oblique angles. These components are parallel (p) and perpendicular (s) to the plane of incidence. Fresnel established various forms of polarized light, be it circular or elliptical. From the discoveries of both Malus and Fresnel, Brewster was able to unify his theory of the polarizing angle (the angle at which all incident light on a surface becomes fully polarized in the s-direction) in 1811 [56]. It is from these fundamental concepts and theories that ellipsometry measurements are even possible to this day.

In 1887, almost 80 years after the discovery of polarization, Paul Drude unified the previous optical theories and laid out the mathematical equations used to describe the change in the polarization state of light upon reflection from a smooth, solid interface [49, 50]. His new theory became the framework from which would describe what is known as modern ellipsometry. The term *ellipsometry*, however, was not coined until 1945 when Alexandre Rothen published his paper describing the instrumentation required to measure a film's thickness using elliptically polarized light [57]. During Rothen's time, all ellipsometry measurements were performed manually at fixed wavelength and were rather time consuming, to say the least.

Ellipsometric measurements did not gain momentum until the mid 1970s when the development and implementation of the first, fully automated spectroscopic ellipsometer came into being by a team led by Aspnes [58]. It was not until the early 1990s, however, that a group from Pennsylvania State University discovered an ellipsometry breakthrough. A new type of ellipsometer was developed with an incorporated photodiode array detector [59]. With such a detector, it was possible to simultaneously measure samples at a whole multitude of wavelengths, both quickly and efficiently. This ability led the way for spectroscopic ellipsometry, whereby multiple wavelengths could be used as a probe to strengthen correlations within data. Throughout the years, ellipsometric techniques have been improving, so much so that there are at least four different ellipsometer models commercially available for many unique tasks [60]. But with all the advances in technology and experimental methods, there is at least one reliable constant – the valid theory laid out by Drude and others some 120 years ago.

3.2 Principles of Optics

Many theoretical aspects of SE found in the following subsection were modeled from Fujiwara's *Spectroscopic Ellipsometry: Principles and Applications* [60] and Tomkins's *Spectroscopic Ellipsometry and Reflectometry: A User's Guide* [61] and *A User's Guide to Ellipsometry* [62], unless otherwise stated.

Light can be described as a transverse electromagnetic (EM) wave propagating through space. Mathematically, these EM waves can be described as 3-dimensional plane waves propagating with time by

$$\boldsymbol{E}(\boldsymbol{r},t) = \boldsymbol{E}_0 \exp\left(-\frac{i2\pi N}{\lambda}\hat{q}\cdot\boldsymbol{r}\right)\exp(i\omega t) \tag{3.1}$$

where $\boldsymbol{r}$ is the propagation vector, t is time, $\boldsymbol{E}_0$ is a complex vector constant describing the amplitude and polarization state of the wave, $\hat{q}$ is the unit vector along the direction of wave propagation, λ is the wavelength of light in a vacuum, ω is the angular frequency of the wave, i is the imaginary number ($i = \sqrt{-1}$), and N is the complex refractive index defined as

$$N \equiv n - ik \tag{3.2}$$

where n is the real part of the refractive index (called the index of refraction) and k is the extinction coefficient. In a dielectric medium, the real part of the refractive index is defined as

$$n \equiv \frac{c_{\text{light}}}{v} \tag{3.3}$$

where c_{light} is the speed of light in a vacuum and v is the speed of light in the medium under study, such that $n \geq 1$. The extinction coefficient describes how rapidly the intensity (or amplitude) of light decreases as it passes through the material due to adsorption. Thus, a transparent medium would have an extinction coefficient near zero. Together, both n and k form a set of optical constants (at fixed wavelength) which completely describe how an EM wave propagates through a medium.

To simplify the electric field equations for a clearer understanding, it is beneficial to study Eq. (3.1) in 1-dimension, that is,

$$E(z,t) = E_0 \exp\left[i\left(\omega t - \frac{2\pi N}{\lambda} z + \delta \right) \right] \tag{3.4}$$

where E_0 is the electric field amplitude, z is the propagation direction, and δ has been introduced as the initial phase of the EM wave. By substituting Eq. (3.2) into Eq. (3.4), the complete equation for a 1-dimensional EM wave traveling in any general light-adsorbing medium can be expressed as

$$E(z,t) = E_0 \exp\left(-\frac{2\pi k}{\lambda} \right) \exp\left[i\left(\omega t - \frac{2\pi n}{\lambda} z + \delta \right) \right]. \tag{3.5}$$

Eq. (3.5) indicates how the light wave oscillates as it passes through a dielectric medium. Figures 3.1(a) and 3.1(b) describe pictorially the behaviour of light propagating across the interface between two dielectric media for a wave of wavelength λ and amplitude E_0 propagating from an ambient of $(n, k) = (n_1, 0)$ into: (a) a medium of $(n, k) = (n_2, 0)$ and (b) a medium with $(n, k) = (n_2, \eta)$, where $\eta > 0$. When $k = 0$, only the real part of the refractive index is important and we recover an expression similar to Eq. (3.4) with a reduced amplitude E_{01} and wavelength λ/n. For materials with $k > 0$, the electric field amplitude will exponentially decay by a factor $E_{01}\exp(-2\pi kz/\lambda)$ as it is adsorbed by the medium. This decay is larger for large k values and as such, the light will not penetrate within a high-k medium (such as a metal).

As light passes through dielectric media, a change in the dielectric polarization is observed. Dielectric polarization of a material arises from charge separation due to an applied electric field, such as an impinging beam of light. Depending on the medium, the degree of polarization varies; dielectric materials exhibit large dielectric polarizations whereas metals show only weak polarizations as applied electric fields lead to charge flow. Dielectric polarizations of materials are very important to understand as the optical constants n and k, which are essential to describing the optical properties of materials, are defined by induced dielectric polarizations. Just as optical properties of matter are described by a complex refractive index, so too are the polarizations of dielectrics. In

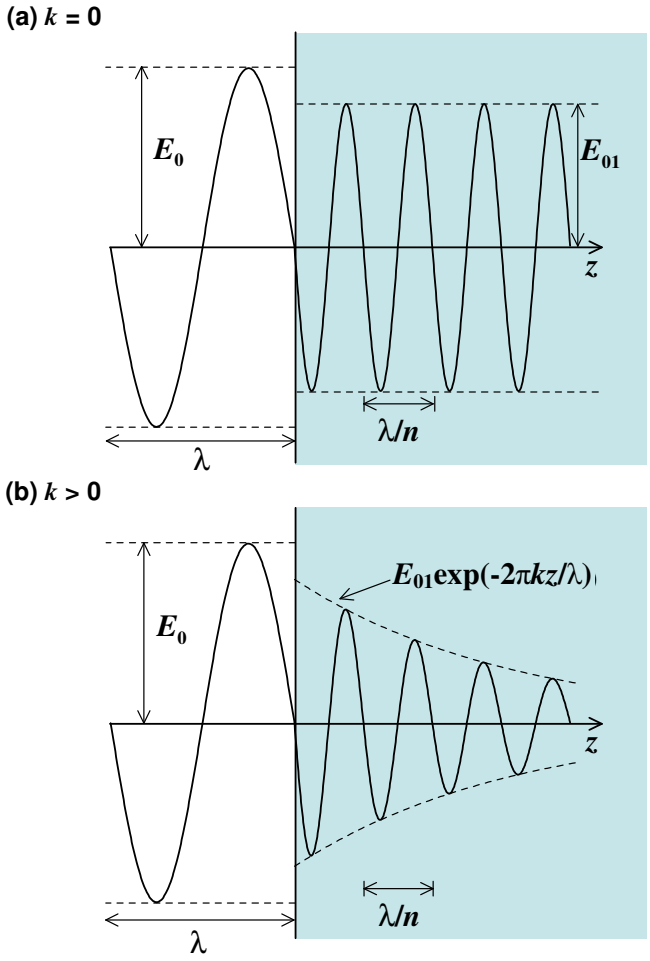

Figure 3.1 Electromagnetic (light) wave propagating from a dielectric medium with $n = n_1$ and $k = 0$ to a dielectric medium with $n = n_2$ and: (a) $k = 0$ and (b) $k > 0$.

this case, however, the complex dielectric constant is employed as a descriptor for dielectric polarization, given mathematically as

$$\varepsilon = 1 + \frac{P_\varepsilon}{\varepsilon_0 E} = 1 + \chi \tag{3.6}$$

where ε is the dielectric constant, P is the 1-dimensional dielectric polarization, E is the 1-dimensional electric field, ε_0 is the permittivity of free space (8.85×10^{-12} F/m) and χ is referred to as the dielectric susceptibility $\left(\chi \equiv P/(\varepsilon_0 E)\right)$. From Eq. (3.6), the dielectric constant increases with the dielectric polarization of the material. For a full derivation of

Eq. (3.6) (beyond the scope of this thesis), the reader is asked to refer to any introductory electrodynamics texts such as Ref. [63].

The complex refractive index is defined by the dielectric constant in the following manner

$$N^2 \equiv \varepsilon \tag{3.7}$$

and similar to N, ε can be expressed as

$$\varepsilon \equiv \varepsilon_1 - i\varepsilon_2 . \tag{3.8}$$

Depending on the application, it is useful to express the optical constants of a material in terms of its dielectric constants through

$$n = \left(\frac{\varepsilon_1 + \left(\varepsilon_1^2 + \varepsilon_2^2\right)^{1/2}}{2} \right)^{1/2} \tag{3.9a}$$

$$k = \left(\frac{-\varepsilon_1 + \left(\varepsilon_1^2 + \varepsilon_2^2\right)^{1/2}}{2} \right)^{1/2} \tag{3.9b}$$

by substitution of Eq. (3.8) into Eq. (3.2). So, by knowing the complex dielectric constants of a material, the optical constants can be calculated and thus its optical properties can be known completely.

With these theoretical aspects discussed, it is useful to discuss how light interacts with a flat, reflective, partially transparent surface at oblique angles of incidence. As a light beam impinges on this surface, it is partially reflected by and partially transmitted into the material. In this discussion, it is assumed that the reader is familiar with both the laws of reflection and refraction (Snell's law), given respectively by

$$\theta_i = \theta_r \tag{3.10}$$

and

$$N_i \sin\theta_i = N_t \sin\theta_t , \tag{3.11}$$

where θ_i, θ_r, θ_t are the complex angles of incidence, reflection, and transmission with respect to the plane of incidence and N_i and N_t are the complex refractive indices of the incident and transmitted media, respectively. From these equations, it can be shown that the light beam will be reflected by an angle equal to that from which it was incident (Eq. (3.10)) and the beam will be transmitted at an angle θ_t which can be calculated from Eq. (3.11).

Light waves can be described by their polarization states relative to the plane of incidence, classified as being either p- or s-polarized. In an ellipsometry measurement, it is convenient to use the p- and s-directions as orthogonal basis vectors to describe the light's polarization states. For the p-polarized direction, the electric fields of the incident and reflected light wave oscillate within the plane parallel to the plane of incidence (which contains the unit vector normal to the surface). Alternatively, for s-polarized light, these light waves oscillate in a plane orthogonal to the p-direction. The p- and s-polarizations define a right-handed Cartesian coordinate system describing the propagation of light.

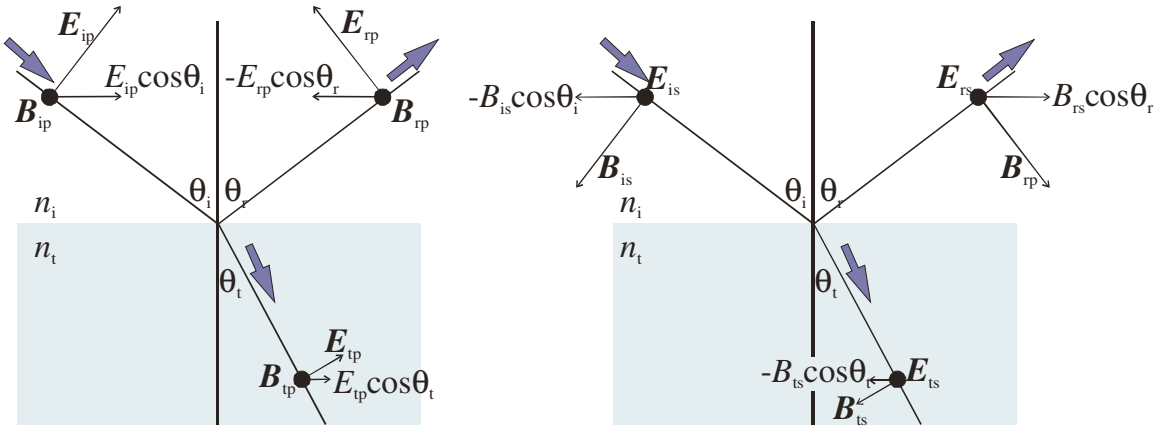

Figure 3.2 Electric field, ***E***, and induced magnetic field, ***B***, for: (a) p-polarization and (b) s-polarization. The solid circles along each beam indicate the field direction orthogonal to the page.

Figures 3.2(a) and 3.2(b) describes the electric and magnetic fields for light impinging on the interface between a transparent ambient with $n = n_i$ and a transparent medium with $n = n_t$, respectively. The subscripts i, r, t, s, and p stand for the incident, reflected, and transmitted fields in either the s- or p-polarization direction, respectively. The light reflection and transmission are represented by the vectors of the electric field and induced magnetic field given as $\boldsymbol{E}_{xy}$ and $\boldsymbol{B}_{xy}$ (where xy = (i, r, t)(s, p)), respectively, for subscript pairs as described above). Both p- and s-polarized light will behave differently when a light beam is incident on a surface at oblique angles. This arises due to the difference in electric dipole radiation induced by the incident light beam on the sample. This variation in p- and s-polarizations is what the ellipsometer records as the change in the polarization state of a light beam. According to the boundary conditions of an EM wave propagating at an interface between two unlike dielectric media, the $\boldsymbol{E}$ and $\boldsymbol{B}$ components parallel to the interface are continuous at the interface.

For p-polarized light and the subscript notation above, these conditions can be expressed as

$$E_{ip}\cos\theta_i - E_{rp}\cos\theta_r = E_{tp}\cos\theta_t \tag{3.12}$$

$$B_{ip} + B_{rp} = B_{tp}\,. \tag{3.13}$$

For a medium with an index of refraction n, it follows that $E = vB$ (with $v = c/n$ from Eq. (3.3)), since $E = cB$ and therefore $B = NE/c$. Here, the complex refractive index has been used in the place of n. It can be shown that the two are equivalent in the formalism presented. So, upon substitution, Eq. (3.13) can be rewritten as

$$N_i\left(E_{ip} + E_{rp}\right) = N_t E_{tp}\,. \tag{3.14}$$

Eliminating E_{tp} from Eqs. (3.12) and (3.14) and using Eq. (3.10) yields the amplitude reflection coefficient

$$r_p \equiv \frac{E_{rp}}{E_{ip}} = \frac{N_t\cos\theta_i - N_i\cos\theta_t}{N_t\cos\theta_i + N_i\cos\theta_t} \tag{3.15}$$

for p-polarized light. Elimination of E_{tp} from Eqs. (3.12) and (3.14) yields the amplitude transmission coefficient for p-polarized light:

$$t_p \equiv \frac{E_{tp}}{E_{ip}} = \frac{2N_i \cos\theta_i}{N_t \cos\theta_i + N_i \cos\theta_t}. \tag{3.16}$$

Similarly, the boundary conditions for s-polarized light are given by

$$E_{is} + E_{rs} = E_{ts} \tag{3.17}$$

$$-B_{is} \cos\theta_i + B_{rs} \cos\theta_r = -B_{ts} \cos\theta_t. \tag{3.18}$$

Following a similar treatment as that used for deriving Eqs. (3.15) and (3.16), an expression for the amplitude reflection and transmission coefficients for s-polarized light is given by

$$r_s \equiv \frac{E_{rs}}{E_{is}} = \frac{N_i \cos\theta_i - N_t \cos\theta_t}{N_i \cos\theta_i + N_t \cos\theta_t} \tag{3.19}$$

$$t_s \equiv \frac{E_{ts}}{E_{is}} = \frac{2N_i \cos\theta_i}{N_i \cos\theta_i + N_t \cos\theta_t}. \tag{3.20}$$

Collectively, r_p, r_s, t_p, and t_s are known as the Fresnel equations of reflection and transmission for p- or s-polarized light (indicated by subscripts). As will be discussed in the following section, an ellipsometry measurement is based on the ratio of the amplitude reflection coefficients r_p/r_s for p- and s-polarized light.

Thin films are typically presented as multi-layers. Some other layer such as an oxide (or a layer formed by chemical reaction) typically coats the surface. Most ellipsometry measurements are made to determine the thickness of such overlying films on a surface in an ambient medium. A beam of light at oblique incidence first interacts with this thin transparent film prior to probing the surface of the substrate below. Often times, there are two or more films present on a substrate's surface (the treatment of accounting for multiple overlayers is similar to one thin layer, and as such, will not be

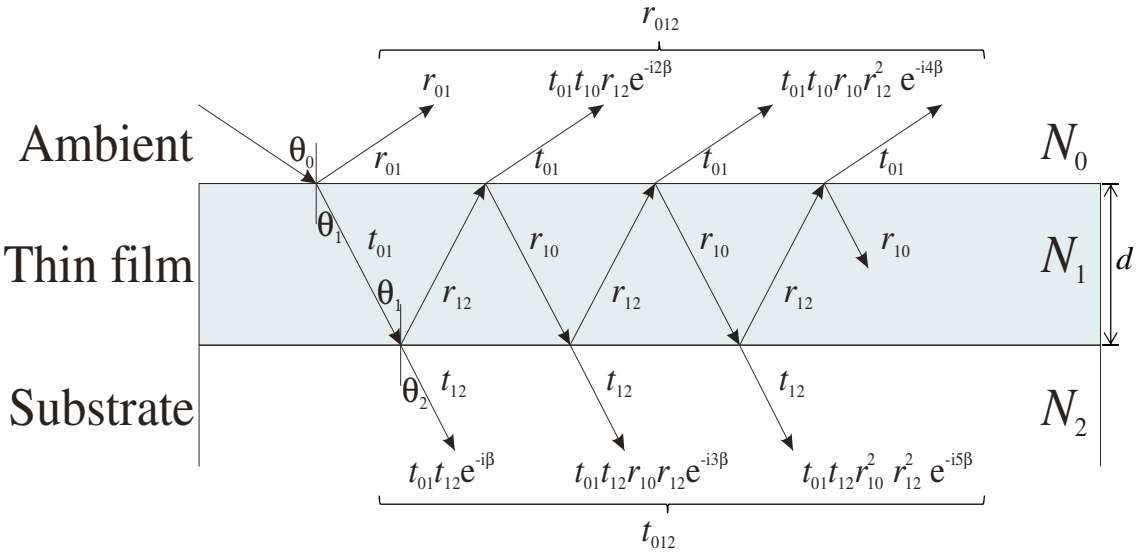

Figure 3.3 A simple optical model consisting of ambient/transparent film of thickness *d*/thick reflective substrate with complex refractive indices of N_0, N_1, and N_2, respectively. Light is incident on the surface at angle θ_0, refracted into the thin film by θ_1, and refracted into the substrate by θ_2. The various r_{ij}'s (t_{ij}'s) indicate the Fresnel reflection (transmission) coefficients for the interface between the various interfaces (where ij = 01, 10, and 12) and r_{012} (t_{012}) describes the total reflection (transmission) coefficient accounting for interferences.

considered as the derivation is more complex and unnecessary to the current discussion). As light strikes this thin film, waves reflected from different locations on the sample will produce interferences – regions where the field is amplified (constructive interference) or reduced (destructive interference). Figure 3.3 depicts a simple optical model consisting of an ambient, a film of thickness *d*, and a thick adsorbing substrate (referred as ambient/thin film/substrate) with complex refractive indices N_0, N_1, and N_2, respectively. At each interface, denoted as 0, 1, or 2 (for the ambient/thin film/substrate, respectively), a reflected or transmitted light beam is present. Thus, a beam incident from the ambient (0) to the thin film (1) interface would be labeled as the 01 beam. These subsequent light beams are described by Fresnel reflection or transmission coefficients (from Eqs. (3.15), (3.16), (3.19), and (3.20)) denoted as $r_{ij,x}$ or $t_{ij,x}$, respectively where ij,x (ij = 01, 10 12; x = s, p) indicates the interface at which reflection or transmission occurs and in which polarization direction the wave is propagating (for example, the p-polarized reflection coefficient between the ambient and thin film is given by $r_{01,p}$).

In this simple model, it can be shown that the propagating electric field (of the form of Eq. (3.1)) including interferences is given by

$$E_{\text{after}} = E_{\text{before}} \cdot \exp(-i2\beta) \tag{3.21}$$

where E_{before} is the electric field at the top of the film stack, E_{after} is the electric field at the bottom of the film stack, and β is what is known as film phase thickness, expressed as

$$\beta = \frac{2\pi d}{\lambda}\left(N_1^2 - N_0^2 \sin^2 \theta_0\right)^{1/2} \tag{3.22}$$

with angle of incidence θ_0. Eq. (3.21) accounts for a phase shift of 2β for each full pass that the light makes through the thin film (from top to bottom).

The total electric field reflected from a surface on a sample similar to Figure 3.3 is merely the sum of the individual fields expected to occur at each interface. In the formalism of Eq. (3.21), it follows that

$$\begin{aligned} E_{\text{total}}^{\text{r}} &= E_1^{\text{r}} + E_2^{\text{r}} + E_3^{\text{r}} + \ldots \\ &= \left(r_{01} \cdot E_{\text{incident}}\right) + \left(t_{01}t_{10}r_{12}e^{-i2\beta} \cdot E_{\text{incident}}\right) + \left(t_{01}t_{10}r_{10}^2 r_{12}^3 e^{-\text{i}6\beta} \cdot E_{\text{incident}}\right) + \ldots \end{aligned} \tag{3.23}$$

Where E_{total}^{r} is the total reflected light wave, E_1^r is the first reflected light beam, E_2^r is the second reflected light beam, and so on. E_{incident} above describes the light wave incident on the film and the r_{xy}, t_{xy} are described elsewhere. Thus, for the *j*th reflected electric field,

$$E_j^{\text{r}} = \left(r_{01} + t_{01}t_{10}\sum_{j=2}^{\infty}\left[r_{10}^{j-2}r_{12}^{j-1} - e^{-i(2j-2)\beta}\right]\right) \cdot E_{\text{incident}} \,. \tag{3.24}$$

Noticing that Eq. (3.23) is of the form $y = \text{a} + \text{ar} + \text{ar}^2 + \ldots$ which has the closed form solution $\text{y} = \text{a}/(1-\text{r})$, Eq. (3.24) can be expressed as

$$E_{\text{total}}^{\text{r}} = \left(r_{01} + \frac{t_{01} t_{10} r_{12} \exp(-i2\beta)}{1 - r_{10} r_{12} \exp(-i2\beta)} \right) \cdot E_{\text{incident}} \,. \tag{3.25}$$

Using Eqs. (3.15), (3.16), (3.19), and (3.20), it is possible to attain the relations

$$r_{10} = -r_{01} \tag{3.26}$$

and

$$t_{01} t_{10} = 1 - r_{01}^2 \tag{3.27}$$

which, when substituted into Eq. (3.25), yields

$$E_{\text{total}}^{\text{r}} = \left(\frac{r_{01} + r_{12} \exp(-i2\beta)}{1 + r_{10} r_{12} \exp(-i2\beta)} \right) \cdot E_{\text{incident}} \tag{3.28}$$

as the simplified total electric field reflected from a sample consisting of a transparent film on a reflective substrate. Therefore, the total Fresnel reflection coefficients in the p- and s-polarization direction can be written directly from Eq. (3.28) as

$$r_{012,\text{p}} = \frac{r_{01,\text{p}} + r_{12,\text{p}} \exp(-i2\beta)}{1 + r_{10,\text{p}} r_{12,\text{p}} \exp(-i2\beta)} \tag{3.29}$$

and

$$r_{012,\text{s}} = \frac{r_{01,\text{s}} + r_{12,\text{s}} \exp(-i2\beta)}{1 + r_{10,\text{s}} r_{12,\text{s}} \exp(-i2\beta)} \,, \tag{3.30}$$

respectively. It follows that the reflectances in the p- and s-polarization directions, defined as the ratio of reflected light intensity I_{r} to incident light intensity I_{i} are respectively

$$R_{\text{p}} \equiv \frac{I_{\text{rp}}}{I_{\text{ip}}} = \left| r_{012,\text{p}} \right|^2 \tag{3.31a}$$

and

$$R_s \equiv \frac{I_{rs}}{I_{is}} = \left| r_{012,s} \right|^2 . \tag{3.31b}$$

By applying Snell's law

$$N_0 \sin\theta_0 = N_1 \sin\theta_1 = N_2 \sin\theta_2 \tag{3.32}$$

the incidence and transmission angles can be determined.

As will be discussed in the following section, the reflectance and reflection coefficients are very important when performing an ellipsometry measurement. In ellipsometry, a measurement of the ratio of the amplitude reflection coefficients (r_p/r_s) is made. These values are the most sensitive when the difference between r_p and r_s is maximized, and thus the best measurement can be obtained. The difference between the reflection coefficients is maximized (in a transparent film) when $R_p = 0$ at a certain angle of incidence, called the Brewster angle θ_B. This occurs because of the electric dipole radiation of the media at an interface. For electric dipole radiation, light does not propagate in the direction of oscillation of the electric dipoles. Thus, at θ_B, the electric dipoles are oscillating in the direction of reflection, thus R_p is a minimum and the amplitude reflection coefficient in the p-polarization is maximized. For s-polarizations, the direction of oscillation of the electric dipoles is always perpendicular to the reflected beam's propagation direction. Thus, R_s does not decrease to a minimum; instead it increases with θ_i. At the Brewster angle, the highest system sensitivity is achieved as the difference in R_p and R_s is maximized, thus, ellipsometry measurements are usually performed at or very near θ_B. The Brewster angle for a material can be calculated through

$$\tan\theta_B = \frac{n_t}{n_i} \tag{3.33}$$

where n_t and n_i are the real parts of the refractive index for a light beam transmitted and incident to a transparent film, respectively and varies (for most materials) between 60-80º.

With the basic theory of light and its interaction with thin films laid out, it is beneficial to discuss what is meant by polarization states of an EM. Earlier, electric field waves were represented as being 1-dimensional waves in the p- or s-polarization state. However, it should be noted that an oscillating electric field is a superposition of two waves describing a vector with components in the p- or s-directions. Light can be unpolarized or polarized. A beam of light with its electric field oscillating in completely random directions perpendicular to the direction of travel is said to be unpolarized. If all of the photons in a light beam are oriented in the same direction, the light is referred to as fully polarized. In an ellipsometry measurement, fully polarized light is used.

Figures 3.4(a)-3.4(c) show the three geometries into which polarized light falls: linear polarization, circular polarization, and elliptical polarization, respectively. Consider two light beams of equal frequency moving along the same path and with equal amplitude, but oscillating in orthogonal planes along the direction of propagation (say, the E_x- and E_y-planes of a 3-dimensional Cartesian coordinate system). As the wave frequencies are identical, the maxima of both waves coincide in space and time along the propagation direction, and thus are called *in phase*. The summation of these waves result in a wave oriented at $\pi/4$ to the *x*-*y* plane whose tip traces out a diagonal line along the z-direction. This is known as linear polarization (Figure 3.4(a)). Next, consider two light waves traveling along the z-direction along the same path with the same frequency and amplitude. Again, one is polarized in the E_x-plane and the other is polarized in the E_y-plane. The maxima of the waves are now out of phase by $\pi/2$, however. So, the electric field of the resultant wave will trace out a circle when viewed perpendicular to the propagation axis. This is called circularly polarized light (Figure 3.4(b)). Elliptically polarized light arises whenever two orthogonal light waves are out of phase by anything other than 0 (or π) or $\pi/2$ or the amplitudes of the waves are not the same. Elliptical polarization is the most general form of polarized light; moreover, both linear and circular polarizations are special cases of elliptical polarization (Figure 3.4(c)).

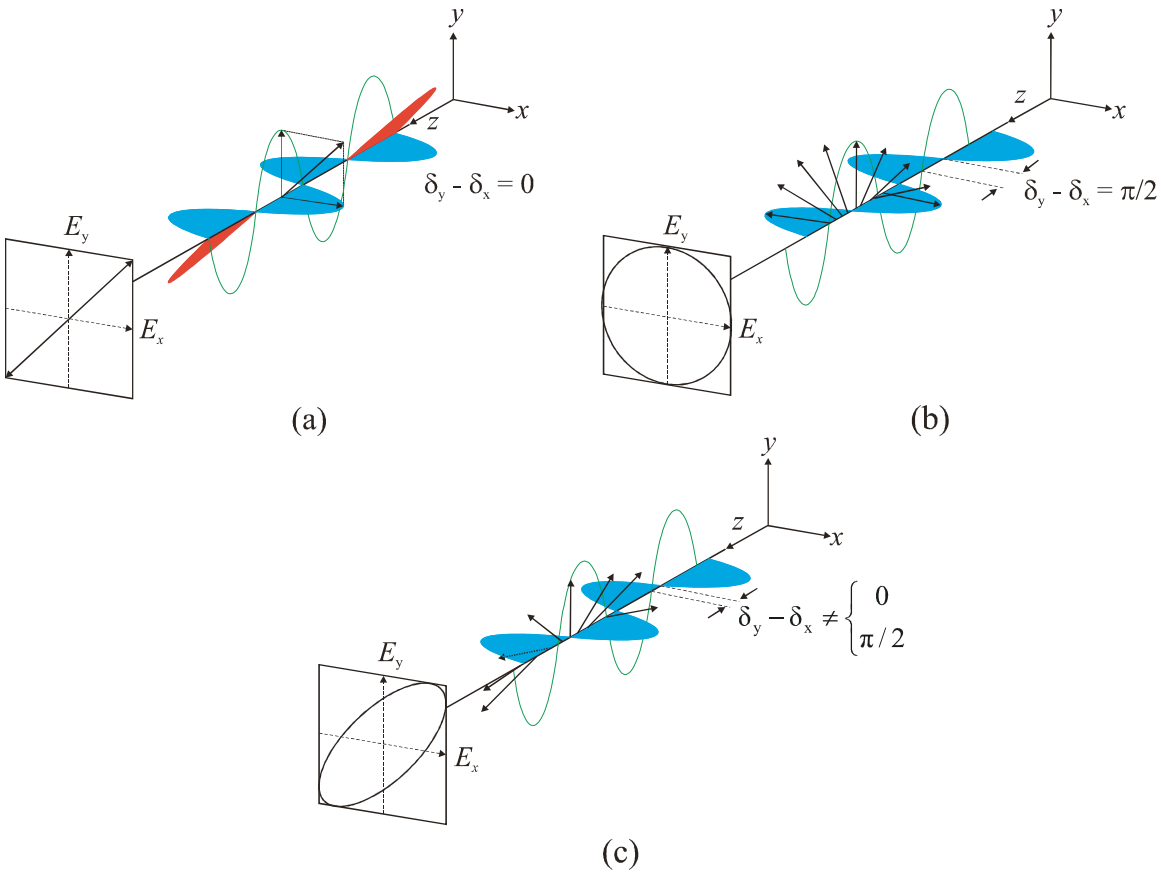

Figure 3.4 Representations of (a) linear polarization, (b) circular polarization, and (c) elliptical polarization. Amplitudes of the electric field components parallel to the *x*- and *y*-axes are equal and their phase differences (δ_x - δ_y) are (a) 0, (b) $\pi/2$, and (c) a value which is not 0 or $\pi/2$.

3.3 Principles of Spectroscopic Ellipsometry

Ellipsometry is a light-based technique used to characterize reflective surfaces. This technique excels at measuring thin-film thicknesses and determining a sample's optical properties. Some of the most important aspects of this technique is that the measurement probe is nondestructive (photons in/out), accurate (thickness resolution on the order of angstroms in practice), and can monitor samples ex-situ (air/sample) as well as in-situ (liquid/sample). However, every technique has drawbacks, and ellipsometry is no different. When the surface roughness of a sample is greater than ~10% of the wavelength of the probing beam, the incident light will reflect from the sample in all directions and not enough will reach the detector, thus making measurement impossible.

Ellipsometry is an indirect form of measurement (which will be discussed below), i.e., a measurement of thickness, for example, is not measured directly. Instead, one must produce an optical model with variable parameters that when fit to the measured data, a layer thickness is obtained. Despite these shortcomings, however, ellipsometry yields very precise measurements of a film's thickness and optical constants and is gaining popularity in many diverse fields.

Modern ellipsometers come in a wide variety of options. Of these instruments, the spectroscopic ellipsometer is one of the best for the research scientist wishing to characterize a thin film sample completely. In the case of these spectroscopic instruments, many wavelengths of light are used to probe a sample's surface, thus allowing for further sensitivity to variable parameters which may exhibit stronger reflections at specific wavelengths. Dalhousie University is home to one of these state-of-the-art spectroscopic instruments manufactured by J.A. Woollam Co., Inc – the M-2000 variable angle spectroscopic ellipsometer. Together with the many probing wavelengths and the ability to vary the incidence angle of the probing light, a colossal amount of data can be obtained from a sample. Thus, by combining the variability in angle and wavelength range, the instrument can be fine-tuned to acquire data which is the most sensitive to the selected model fit parameters and obtain the highest quality results. An additional advantage to spectroscopic ellipsometers over single angle and/or single wavelength instruments is the use of dispersion models; these provide parameterized optical constants of materials using the full range of wavelengths available and can be inferred mathematically in outlying regions.

All ellipsometers are constructed from a series of "optical elements" which aid in getting a beam of light into the correct form to obtain useful data. Most modern spectroscopic instruments can be classified into two major categories: instruments that use rotating optical elements and instruments that use photoelastic modulation. Only the former instruments will be discussed as it is the class of instruments under which category the M-2000 falls. Amongst rotating optical element ellipsometers, the three most common versions are the rotating-analyzer ellipsometer (RAE), the rotating-polarizer ellipsometer (RPE), and the rotating-compensator ellipsometer (RCE). Only the latter will be considered as this is the instrumentation of the ellipsometer at Dalhousie

University. Figure 3.5 shows a block diagramme of the construction of the M-2000 spectroscopic ellipsometer which consists of the following optical elements: a light source, a beam polarizer, a rotating compensator, the sample, an analyzer, and a detector. The proceeding discussion will briefly introduce these elements and their role in a SE measurement.

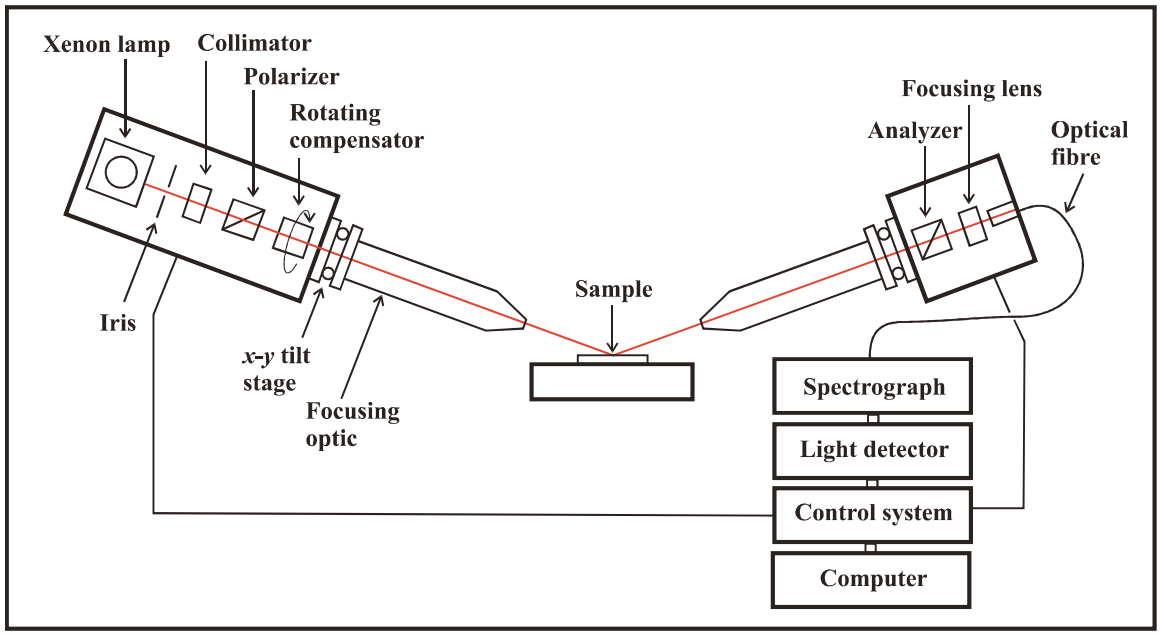

Figure 3.5 Block diagramme of the optical components of the J.A. Woollam M-2000 spectroscopic ellipsometer at Dalhousie University.

For any ellipsometry measurement, the light source is paramount. Single wavelength ellipsometers are able to use very stable lasers for their measurements, but for spectroscopic ellipsometers, a broad-range spectral output is required. This adds further difficulties as the source must be very stable (constant intensity over time) over the full spectral range, but no such sources exist. Typically, a Xe arc lamp is used as it provides adequate stability and emits light in the visible/near UV light range from 190-2000 nm; however, the intensity is low below 260 nm and has very strong emission lines from about 880-1010 nm, which can overload the silicon detector. The actual measurement of the M-2000 consists of 490 wavelengths in the spectral range from 210-1000 nm.

After emission from the arc lamp, the light passes through a polarizer. A polarizer is generally a prism made of calcite ($CaCO_3$). Calcite is a transparent,

birefringent mineral that can be used to control the polarization state of light. A Glan-Taylor prism, as present in a spectroscopic ellipsometer, is made from two calcite prisms and extracts only linearly polarized light from an unpolarized light source. The Glan-Taylor prism in the M-2000 polarizes light to 1 part in 10^6 and can be used in a spectral range from 230-2200 nm. The polarizer is typically set to $\pi/4$ to provide linearly polarized light with equal parts p- and s-polarization contributions incident on the sample.

Next, the linearly polarized beam enters into a rotating compensator. This element is used to convert the light to a circular polarization using a birefringent crystal (either MgF_2 or mica) by inducing a phase difference of $\pi/2$ in the beam. Birefringence is a phenomenon whereby a phase difference between electric field waves is induced as the material allows one polarization direction to move through the material faster than the other. Compensators are used to reduce errors in resolving the phase difference in measurements (known as Δ, where $0^\circ \leq \Delta \leq 360^\circ$ ($0 \leq \Delta \leq 2\pi$)). Without the compensator, sensitivity of Δ near 0° or 180° (0 or π) is lost, thus inducing errors in measurement. Also, the compensator allows accurate determination of depolarization effects of the light as it passes through the system. In some ellipsometer configurations (including the M-2000), the compensator is rotated to induce a variation of circular polarizations in the beam. By rotating this optical element, a more accurate determination of the ellipsometric parameters is attained by determining the handedness of the beam.

Following the compensator, the circularly polarized light beam impinges on the sample. The light interacts with the surface in a similar fashion as described in Section 3.2. The interference incurred by the beam changes its polarization state, inducing a phase shift between 0 and 2π and attenuates the p- and/or s-components. The reflected light then passes an analyzer. The analyzer is physically identical to a polarizer but differs in functionality. Instead of converting unpolarized light to linearly polarized light, the analyzer is used to record the polarization state of the reflected beam whose intensity varies due to the rotating-compensator. It linearizes the elliptically polarized light and compares the variation in intensities of this beam to that of the known input polarization to determine the polarization change caused by the sample reflection. The resultant beam

leaving the analyzer will have a phase difference of $\pi/2$ due to the rotation of the analyzer.

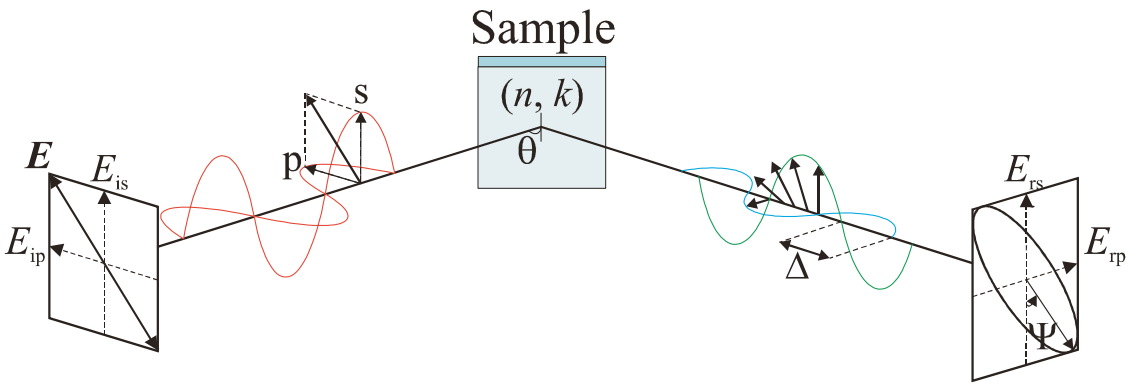

Figure 3.6 Geometry of a typical ellipsometry measurement. Linearly polarized light (described by the components of ***E***) reflects from a sample of (n, k) and becomes elliptically polarized. Changes in the polarization states of light between the incident and reflected beams, known as the phase difference (Δ) and amplitude ratio (Ψ) are measured at the detector.

From this point, the light impinges on the detector and a measurement of intensity is performed. In the M-2000, the beam is reflected from a mirror and directed onto an optical fiber which carries the beam to the detector. The light is then dispersed by a grating onto a charge-coupled device (CCD) silicon photodiode array which records the beam's intensity at all wavelengths in the spectral range simultaneously.

The remainder of this section describes the mathematics and theory explaining the principles of a measurement using SE. Figure 3.6 shows pictorially the geometry of a general ellipsometry measurement. The linearly polarized incident electric field ***E*** is defined by its p- and s-components oriented along the x- and y-axes with ordinates E_{ip} and E_{is}, respectively. Upon reflection from a sample, the light becomes elliptically polarized, as shown on the right side of Figure 3.6 and is described by a similar orthogonal coordinate system defined by ordinates E_{rs} and E_{rp} of the electric field. During an ellipsometry measurement, two parameters are measured. These are the phase difference, Δ, between the p- and s-polarizations of the reflected beam and the amplitude ratio, Ψ, of the p- and s-polarizations as projected onto the detector. These parameters are defined by the ratio of the amplitude reflection coefficients for p- and s-polarizations, expressed as

$$\rho \equiv \tan\Psi \exp(i\Delta) \equiv \frac{r_p}{r_s}. \tag{3.34}$$

In polar coordinates, the ellipsometric parameters can be expressed in terms of the amplitude reflection coefficients by

$$\tan\Psi = \frac{|r_p|}{|r_s|} \tag{3.35a}$$

and

$$\Delta = \delta_{rp} - \delta_{rs} \tag{3.35b}$$

where $\delta_{r(s,p)}$ is the phase of the reflected wave in the p- and s-direction, respectively. By applying Eqs. (3.31a) and (3.31b) to Eq. (3.35a), the amplitude ratio becomes

$$\Psi = \tan^{-1}(|\rho|) = \tan^{-1}\left(\frac{|r_p|}{|r_s|}\right) = \tan^{-1}\left[\left(\frac{R_p}{R_s}\right)^{1/2}\right], \quad 0^o \le \Psi \le 90^o \tag{3.36}$$

where the magnitude of a quantity is defined as $|q| = \sqrt{qq^*}$ where q^* is the complex conjugate of q. The phase difference can be extracted from Eq. (3.34) by taking its argument, that is,

$$\Delta = \arg(\rho) = \begin{cases} \tan^{-1}[\mathrm{Im}(\rho)/\mathrm{Re}(\rho)] & \text{for } \mathrm{Re}(\rho) > 0, \\ \tan^{-1}[\mathrm{Im}(\rho)/\mathrm{Re}(\rho)] + 180^o & \text{for } \mathrm{Re}(\rho) < 0, \quad \mathrm{Im}(\rho) \ge 0 \\ \tan^{-1}[\mathrm{Im}(\rho)/\mathrm{Re}(\rho)] - 180^o & \text{for } \mathrm{Re}(\rho) < 0, \quad \mathrm{Im}(\rho) < 0 \end{cases} \tag{3.37}$$

where Im(ρ) and Re(ρ) are the imaginary and real parts of Eq. (3.34).

The electric field reflected from the sample that reaches the detector can be derived by examining the Stokes vectors and Mueller matrices of each optical element in the system. As the mathematics is tedious and beyond the scope of the current work, only the result is given below:

$$E_{\mathrm{D}} = \left(\cos^2 \mathrm{C} - i \sin^2 \mathrm{C}\right) \sin \Psi \exp(i\Delta) + \left(1 + i\right) \cos \mathrm{C} \sin \mathrm{C} \cos \Psi \tag{3.38}$$

where E_{D} is the electric field at the detector and C is the rotation angle of the compensator. It follows from the electric field that the light intensity at the detector is

$$\begin{aligned} I &= \left|E_{\mathrm{D}}\right|^2 \\ &= I_0 \left(2 - \cos 2\Psi + 2 \sin 2\Psi \sin \Delta \sin 2C - \cos 2\Psi \cos 4C + \sin 2\Psi \cos \Delta \sin 4C\right) \end{aligned} \tag{3.39}$$

where I_0 represents the proportionality constant of the reflected light whose intensity is proportional to the incident light intensity. Typically, Eq. (3.39) is described by the more general formula

$$I(t) = I_0 \left(1 + \alpha_2 \cos 2\omega_{\mathrm{C}} t + \beta_2 \sin 2\omega_{\mathrm{C}} t + \alpha_4 \cos 4\omega_{\mathrm{C}} t + \beta_4 \sin 4\omega_{\mathrm{C}} t\right) \tag{3.40}$$

where $I(t)$ is the time-dependent light intensity at the detector, $\omega_{\mathrm{C}} t$ describes the rotation angle of the compensator ($\mathrm{C} = \omega_{\mathrm{C}} t$), and $\alpha_{(2,\,4)}$ and $\beta_{(2,\,4)}$ are called the normalized Fourier coefficients. From Eq. (3.40), a Fourier analysis leads to the determination of the Fourier coefficients using a very complex Mueller matrix formalism, which yields the solutions of Ψ and Δ. The mathematical description of these calculations is beyond the scope of this thesis, however it should be noted that the SE analysis software CompleteEASE by J.A. Woollam Co., Inc. performs these matrix calculations almost instantaneously yielding very accurate (Ψ, Δ) pairs.

With an accurate knowledge of the ellipsometric parameters, Ψ and Δ, it is a relatively simple task to extract quantitative information from a sample. In general, the modeling process begins with choosing a correct optical model as shown, for example, in Figure 3.3. The preceding steps are followed sequentially to determine the sample's quantities of interest, using an optical model of the form used in Figure 3.3:

1. The phase thickness of the film is calculated using Eq. (3.22).

2. The p-polarized amplitude reflection coefficient is calculated for a beam incident on the film from the ambient using Eq. (3.15) with i = 0 and j = 1.

3. The p-polarized amplitude reflection coefficient for the beam incident on the substrate from the film is calculated using Eq. (3.15) with i = 1 and j = 2.

4. The total amplitude reflection coefficient for the p-polarization direction is calculated from Eq. (3.29).

5. Steps 2-4 are repeated for the s-polarization direction, using Eq. (3.19) instead of Eq. (3.15) in Steps 2 and 3, and Eq. (3.30) in Step 4.

6. The ellipsometric parameters Ψ and Δ are evaluated from the p- and s-polarized total reflection coefficients using Eq. (3.34).

For more complex systems of multi-layers, a similar procedure is followed with the addition of calculating more amplitude reflection coefficients between the various film interfaces.

The match between the model and the measurement is expressed in terms of a weighted mean-squared error (wMSE). It is described mathematically by

$$\mathrm{wMSE} = \sqrt{\frac{1}{2\mathrm{N} - M}\sum_{i=1}^{N}\left[\left(\frac{\Psi_{\mathrm{i}}^{\mathrm{model}} - \Psi_{\mathrm{i}}^{\mathrm{exp}}}{\sigma_{\Psi,\mathrm{i}}^{\mathrm{exp}}}\right)^2 + \left(\frac{\Delta_{\mathrm{i}}^{\mathrm{model}} - \Delta_{\mathrm{i}}^{\mathrm{exp}}}{\sigma_{\Delta,\mathrm{i}}^{\mathrm{exp}}}\right)^2\right]} \tag{3.41}$$

where N is the number of (Ψ, Δ) pairs sampled, M is the number of variable parameters selected in the optical model (superscripts "model" and "exp" indicate whether the parameter was found from the model or from the experimental collected data), and $\sigma_{(\Psi,\Delta),\mathrm{i}}^{\mathrm{exp}}$ are the standard deviations on the collected (Ψ, Δ) values, respectively. However, in the latest editions of SE fitting software, the definition of MSE has been modified. CompleteEASE, for example, uses what is known as the absolute MSE as a default to describe the goodness of fit. This definition is quoted as the MSE instead of Eq. (3.41) as it is more closely related to what the instrument measures – a measurement of light

intensity rather than the ellipsometric parameters (which themselves are measurements of the electric field). The absolute MSE is given by

$$\mathrm{MSE} = 1000 \times \sqrt{\frac{1}{3\mathrm{N} - M} \sum_{i=1}^{N} \left[\left(S_{1(\mathrm{model,i})} - S_{1(\mathrm{exp,i})} \right)^2 + \left(S_{2(\mathrm{model,i})} - S_{2(\mathrm{exp,i})} \right)^2 + \left(S_{3(\mathrm{model,i})} - S_{3(\mathrm{exp,i})} \right)^2 \right]} \tag{3.42}$$

where $S_{1(\mathrm{model,\ exp),i}}$, $S_{2(\mathrm{model,\ exp),i}}$, and $S_{3(\mathrm{model,\ exp),i}}$ are the ellipsometric parameters given in terms of intensities obtained from the model or experimental data, respectively. These values are defined in terms of the ellipsometric parameters through

$$S_1 = \cos 2\Psi \,, \tag{3.43a}$$

$$S_2 = \cos 2\Psi \cos \Delta \,, \tag{3.43b}$$

and

$$S_3 = \sin 2\Psi \sin \Delta \,. \tag{3.43c}$$

A scaling factor of 1000 is included in Eq. (3.42) to force it to appear closer to typical values of Eq. (3.41) for "good" fits. Because uncertainties in S_1, S_2, and S_3 are on the order of 0.001, the scaling factor is there to give an excellent fit an MSE of about 1.

This chapter was intended to give readers an understanding of spectroscopic ellipsometry and the instrument here at Dalhousie University. It should be noted that the typical examples examined here were rather simple in context. Anisotropy and other optical properties were not discussed at all. However, ellipsometry can handle these non-idealities of samples and the analysis is made without too much additional work due to included packages within SE analysis software.

Chapter 4 Other Instrumentation

4.1 Magnetron Sputter Deposition

Sputtering is an economical and rapid method of producing thin film samples of several hundred nanometres in thickness. In general, sputter deposition is the process by which a material, described as the target, is deposited onto a substrate by means of glow discharge, or plasma. The technique is used in both scientific and industrial applications wherever thin film coatings are required (such as antireflective coatings on glass for optical applications). In this thesis, sputter deposition was used to prepare thin film electrodes for study.

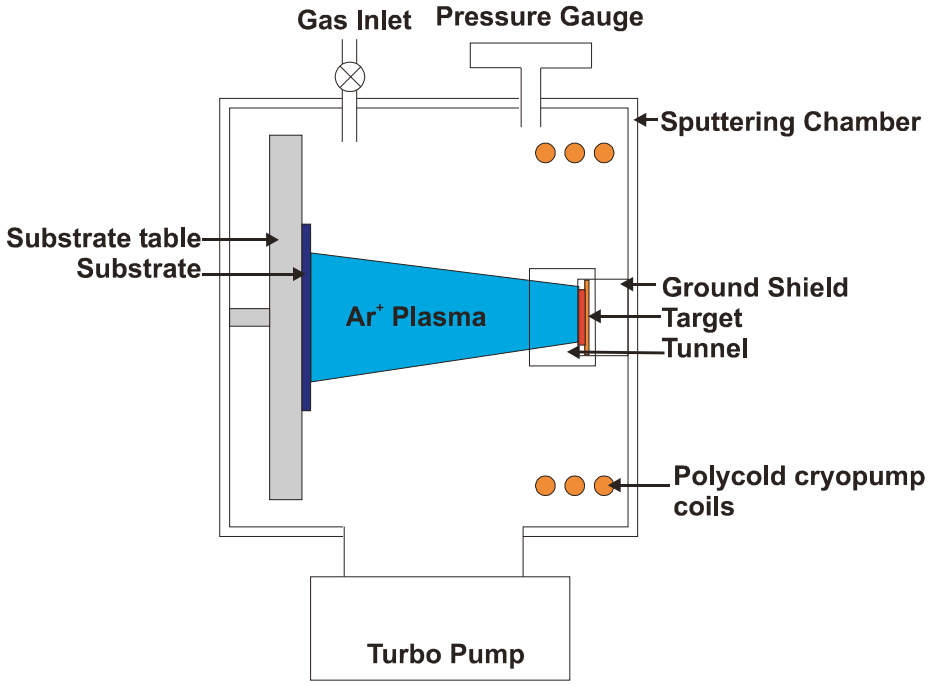

Figure 4.1 Schematic of a top-down cross-sectional view of a sputtering chamber and components during a deposition of a target material.

Figure 4.1 shows a schematic representation of the interior of a vacuum chamber during a typical sputtering deposition. Here, a turntable is depicted opposite the target

material. The target acts as a live cathode (with a very high negative voltage). Once a sufficiently high vacuum within the chamber has been established (~10^{-7} torr), the sputtering process can begin. First, process gas (typically Ar) is flowed into the chamber at millitorr pressures. Then, a large negative voltage is applied to the target material. The neutral atoms of the process gas undergo collisions among themselves and available free electrons which initially ionizes the atoms. These positively charged ions are then accelerated towards and bombard the negatively biased target material. Through a transfer of momentum, neutral atoms (or clusters of neutral atoms) from the target are ejected along with electrons. To maintain charge neutrality, the target material must be conducting. If it is not, then a radio frequency (RF) power supply must be used. These ejected electrons, called secondary electrons, are energetic enough to further ionize the process gas and produce more ion-target interactions, thus increasing the rate of deposition. The ionization of the process gas provokes the release of a photon. This leads to the glowing behaviour characteristic of a plasma.

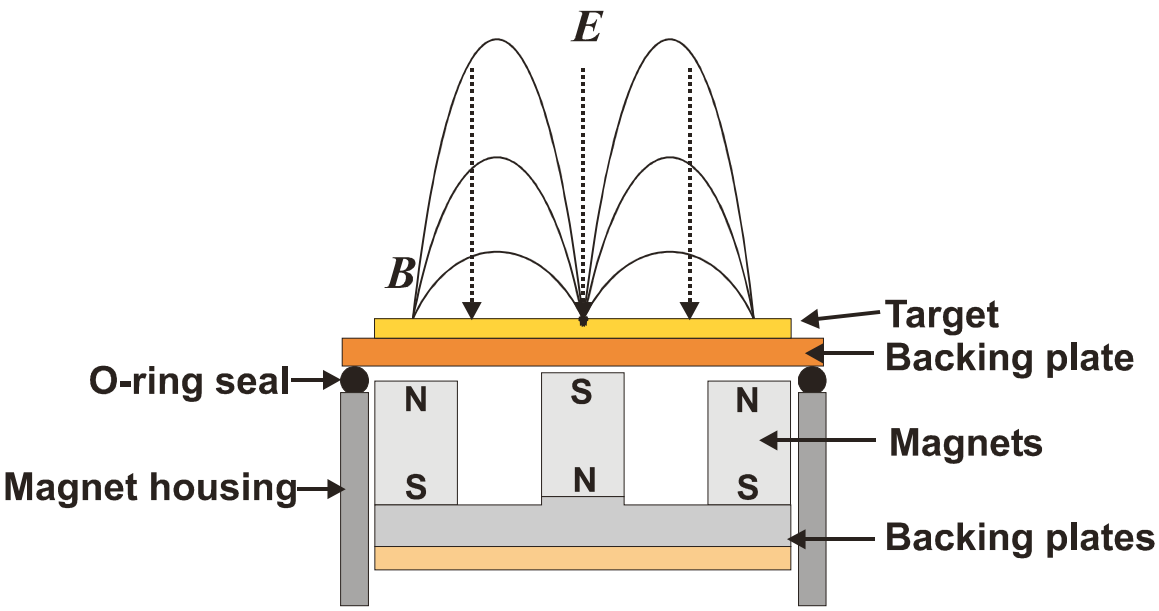

Figure 4.2 Cross-sectional view of a magnet, target material, and Cu backing plate used in magnetron sputter deposition. Magnet polarizations, magnetic field lines, and electric field lines are shown.

Typically, the target material is backed by magnetrons consisting of strong permanent magnets. Figure 4.2 shows a side-on schematic of the magnets, their

polarizations, and resultant magnetic field lines. The magnetic field traps electrons which swirl over the target's surface following the magnetic field lines while at the same time being repelled by the electric field. These electrons can continuously ionize neutral atoms of process gas, thus increasing sputtering efficiency by localizing the electron density near the target and allowing sputtering at lower pressures [64]. The use of magnet-backed targets is called magnetron sputtering.

Figure 4.3 shows a photograph of one of the two magnetron sputtering systems at Dalhousie University. The base system is a Corona Vacuum Coaters V-3T 5-target sputtering machine. The cylindrical vacuum chamber is 46 cm in diameter and holds a 41 cm diameter water-cooled substrate table opposite the magnetrons which rotates about a horizontal axis. Five targets 5.0 cm in diameter backed by water-cooled magnetrons allow for target material deposition. The distance from the substrate table to the target is 5 cm. The system can be evacuated at high vacuum to roughly 3.2×10^{-7} Torr using a series of 3 pumps: a Varian 500 L/s turbo pump, a rotary vane pump for roughing and backing of the turbo, and a Polycold refrigeration unit. This last pump is supplied with a coolant which cycles through metallic pipes and traps excess moisture. The sputtering system is equipped with both direct current (DC) and RF power supplies to provide the high voltage to the target cathodes. In addition, the system has 3 pressure gauges for various pressure ranges: a capacitance diaphragm gauge for 0.1-20 mTorr, convector gauges for pressures above 0.1 mTorr, and an ion gauge for pressures below 10^{-4} Torr. The system also has two mass-flow controllers which accurately introduce process gas into the chamber for ionization. These process gases include Ar, O_2, and N_2. A ground shield and 10.2 cm diameter tunnel can be placed over each target to define the sputtering track, a 7.6 cm band centred 13.3 cm from the centre of the sputtering table, along which the target material is deposited.

To create variable thin film chemistries, several modifications must be made in terms of the flux of deposited atoms from the target material. For a fixed table position, the "open tunnel" system deposits an approximately Gaussian mass (and thickness) profile, whereby the most massive (thick) portion of the film occurs directly opposite the target in the centre of the sputtering track and falls off accordingly. When the table is rotated in the same open tunnel configuration, the deposition profile occurs as an annulus.

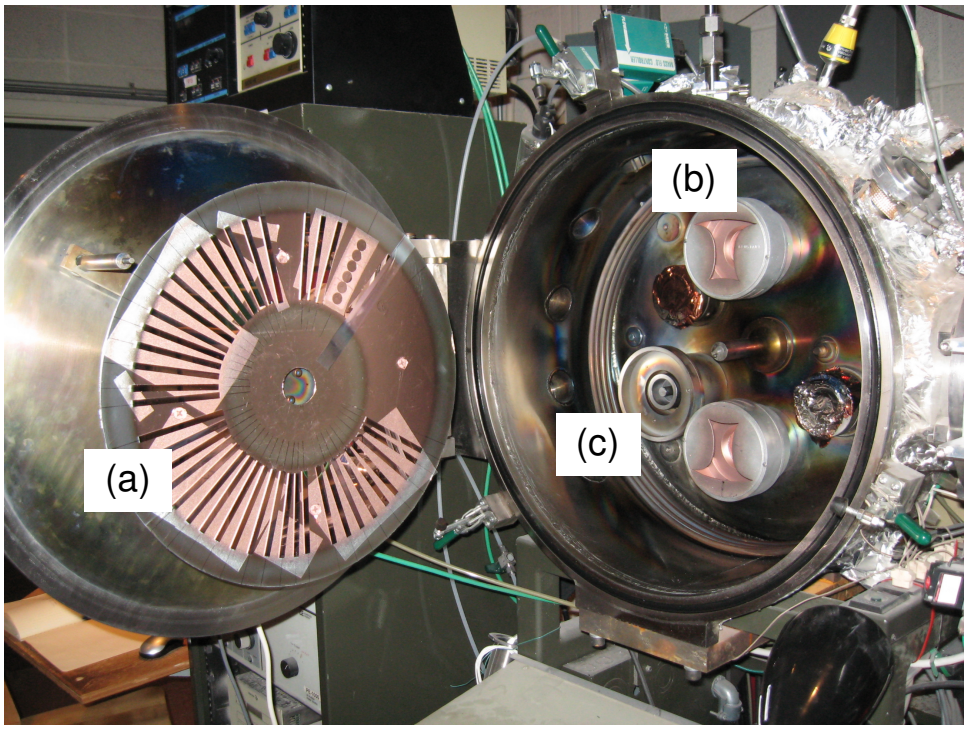

Figure 4.3 Photograph of the magnetron sputter deposition machine used to prepare thin film electrodes for electrochemical testing. The particular sputtering run shown is for a Cu film deposited on glass substrates similar to the preparation of the electrodes used for in-situ electrochemical testing. The rotating table (a), mask-covered targets (b), and Cr plasma cleaner (c) can be seen, as well as other components described in Figure 4.1.

To provide a stylized radial deposition profile as the table rotates, masks with specific shapes were calculated and machined to fit over the tunnels to produce the proper flux of deposited atoms [65]. Figures 4.4(a)-4.4(c) show a schematic of the masks that were calculated which exhibit various mass deposition patterns. Figure 4.4(a) allows for an approximately constant mass per unit area along the radial direction of the sputtering track ("constant" mask). The mask shown in Figure 4.4(b) produces a deposition profile whose mass per unit area increases linearly towards the inside edge of the sputtering track ("linear-in" mask). The mask shown in Figure 4.4(c) produces a deposition profile whose mass per unit area linearly increases towards the outside edge of the sputtering track ("linear-out" mask).

In the current work, only the "constant" mask was used; however, other more exotic films can be produced as follows. Figure 4.4(d) shows an example of a co-deposited 2-material binary film. Consider, for example, two target materials A and B

which were covered by a "linear-in" mask and a "linear-out" mask, respectively. Were both targets to be simultaneously energized and the substrate table was allowed to rotate, a binary film whose composition varied as A_xB_{1-x} ($0 \leq x \leq 1$) would be produced (where x is the amount of A in the material). A 3-component ternary (or 4-component quaternary) system can be produced by including three (or four) targets and using a special substrate table described elsewhere [65, 66]. These combinatorial methods are useful for high-throughput screening of new materials for a variety of applications.

In summary, magnetron sputtering is a useful way to produce many reproducible thin film samples efficiently and quickly.

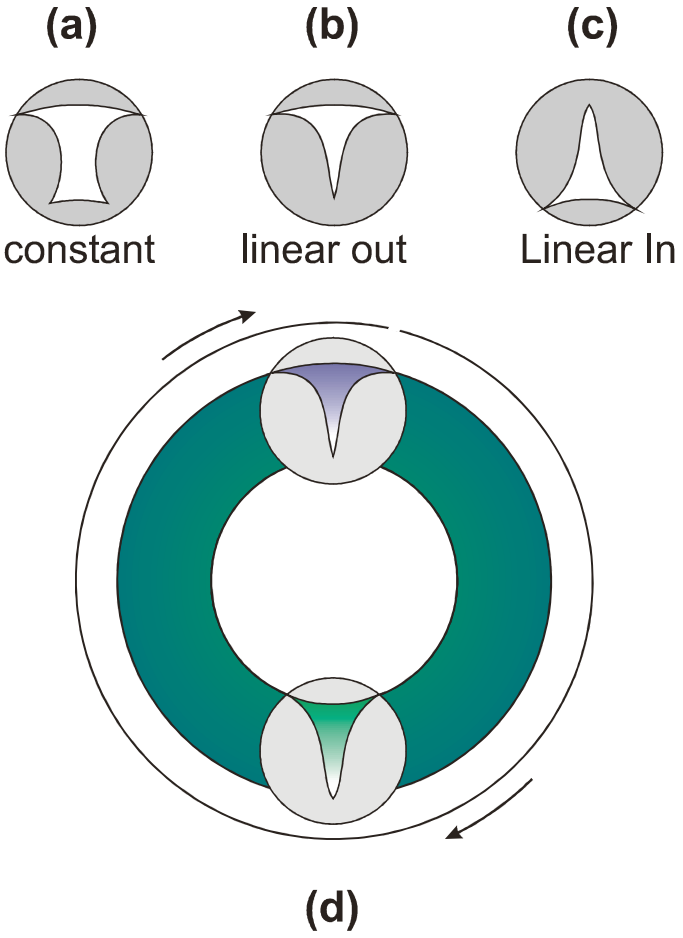

Figure 4.4 Schematic of various sputtering masks including: a constant mask (a), a "linear out" mask (b), and a "linear in" mask (c). An example of a binary 2-component linear composition gradient is shown in (d) using the "linear out" and "linear in" masks.

4.2 In-situ Electrochemical Cell

To perform high quality in-situ electrochemical and optical measurements, an in-situ cell is required. This section discusses the design of the cell and considerations involved in its construction.

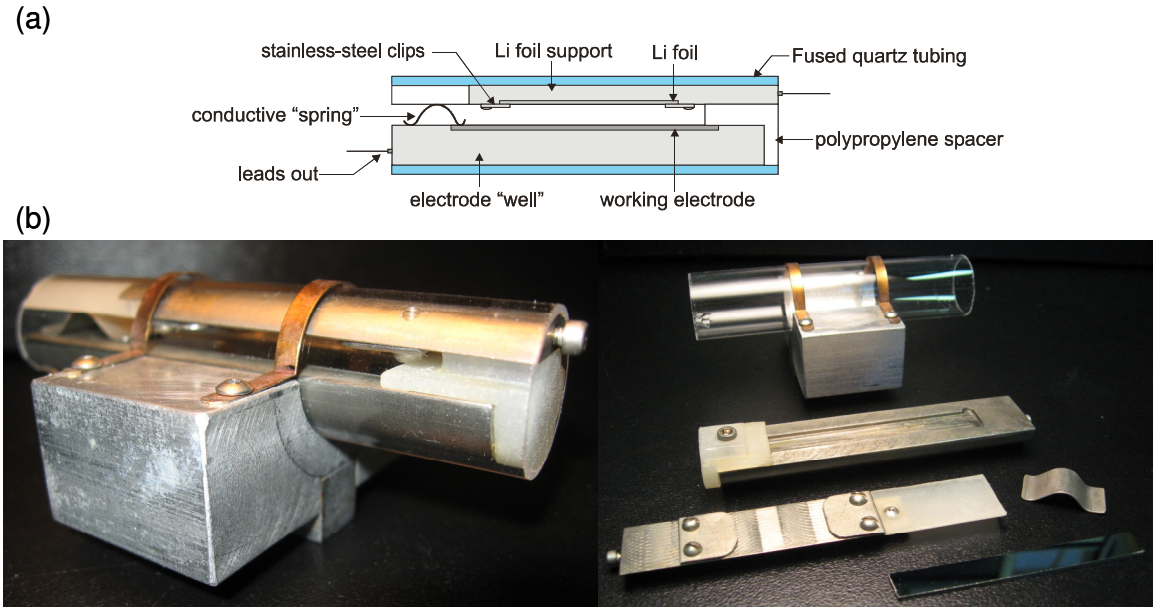

Figure 4.5 Schematic (a) and photographs (b) of the in-situ electrochemical cell used for study with spectroscopic ellipsometry.

The in-situ electrochemical cell was made to be large enough to assemble using the bulky gloves of a laboratory glove box, yet small enough to minimize assembly costs (less electrolyte and Li foil used). The design for the in-situ electrochemical cell was based on a modification to an in-situ cell for studying protein adsorption on sputtered metal films using SE [67]. Figures 4.5(a) and 4.5(b) show a schematic and photographs of the fused quartz in-situ cell, respectively. The main body of the cell was made from an 8.3 cm long fused quartz round tube from Technical Glass Products, Inc. (Ohio, USA) (cut down from a 1.2 m length with a diamond saw). This tube had a 17 mm inside diameter and a 19 mm outside diameter. Fused quartz was chosen as it is optically transparent over a broad wavelength range [68], it is electrochemically inert, has low stress, and is compatible with a variety of optical experiments. The negative electrode

material to be studied was fixed in a 5.7 cm x 0.6 cm x 0.1 cm "well" machined within an 8.3 cm long stainless steel half-rod (8.5 mm radius) which could be inserted within the fused quartz tubing. The counter/reference electrode holder was a flat, roughened 8.3 cm long stainless steel semi-rod which shared the same curvature as the fused quartz tube and was only 4 mm thick. A piece of Li foil was fixed to the flat part of the holder by two flat stainless steel clips held by screws. The counter/reference electrode was held above the negative electrode "well" by a stainless steel spring clip which applied pressure to both the counter/reference electrode support as well as to the negative electrode material in its stainless steel "well" (the spring clip also ensured there was good electrical contact between the negative electrode and its well). A portion of the counter/reference electrode support was made from insulating polypropylene to avoid electrical contact between the electrodes.

Stainless steel was chosen as the cell component material as it is electrochemically inert within the voltage range considered (less than 3 V vs Li/Li^+) and is electrically conductive. Stainless steel vacuum fittings were used to enclose the tube body and provide a liquid-tight and air-free environment. Kalrez® o-rings were used to make the seal as they are resistant to decomposition and swelling from organic solvents. To minimize the volume of the vacuum fittings, polypropylene filler was machined and inserted inside of the fittings. Leads were fixed to both the working electrode "well" and the Li-foil support which were attached to terminals at the far ends of the vacuum fittings. The vacuum fittings served as electrical contacts to the outside of the cell. An aluminum support block with phosphor-bronze tie-downs and a steel key was machined to hold the fused quartz tubing in a corresponding keyway on the ellipsometer mounting stage during a measurement. When fully constructed, the in-situ cell held ~8 mL of electrolyte.

The cell design shown in Figure 4.5 does not include a separator as is found in most Li-ion cells. An ionically conducting separator is not required as the electrodes are spatially separated by a large 8 mm gap. As the cell is tested for a week at a time, dendritic Li does not form and make electrical contact with the negative electrode material, thus shorting the cell. Also, with such a large gap between the electrodes, it is important to ensure the electrodes are directly across from one another to minimize solution resistance effects from excessive ion transport path lengths.

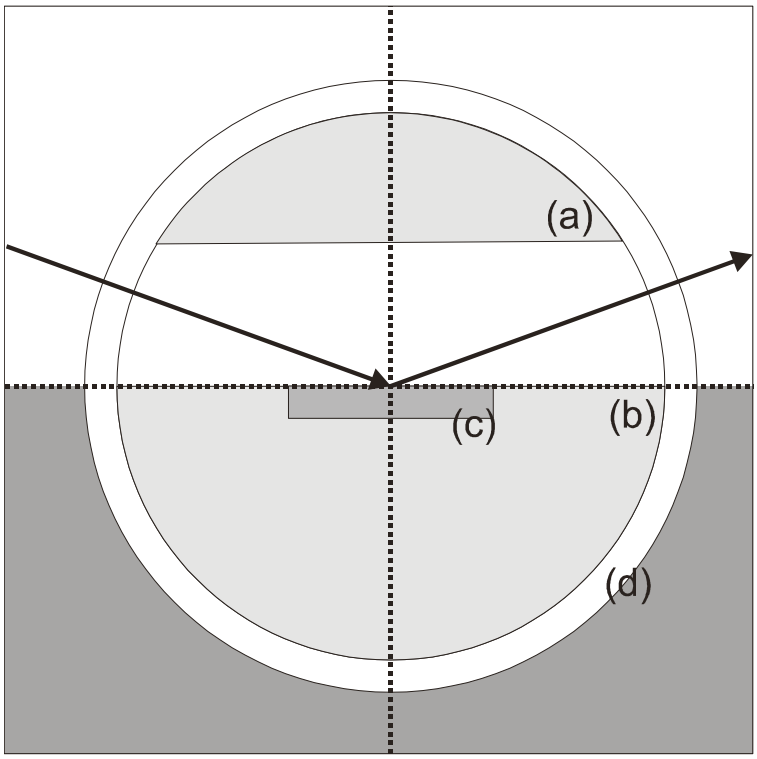

Figure 4.6 Cross-section of the in-situ electrochemical cell, including the Li electrode support (a), the working electrode material "well" (b), the working electrode material (c), and the fused quartz tube body (d). The incident and reflected light beams are depicted as heavy arrows impinging onto/reflecting from the working electrode material.

Figure 4.6 shows a cross-section of the in-situ cell as well as the path the ellipsometer beam takes as it enters and exits the in-situ cell. Ideally, the wall thickness of the quartz tube should be zero. However, as the tube has a physical thickness, it is essential to control the in-situ cell alignment on the ellipsometer mounting stage. The working electrode material under study must lie along the centerline of the quartz tube. If not, then the incident and reflected beam path lengths could vary, thus yielding systematic errors in the measurements of both Ψ and Δ parameters. Since the tube is curved, it is essential that the beam enter and exit at normal incidence. In this geometry, the air/quartz and quartz/electrolyte interfaces can be ignored in the modeling as only the surface chemistry occurring on the thin film electrode is observed.

The light beam must be focused to a spot as small as possible. Consider a (circularly) curved glass tube with some physical thickness and an index of refraction which differs from the local ambient. The tube wall acts as a lens and a beam of light

entering will refract at the ambient/quartz interface and bend towards normal. Similarly, at the quartz/ambient interface, the beam will refract back to the original incident angle and subsequently impinge on a different location than the unrefracted beam. In the system used in this thesis, focusing optics were used to shrink a 4 mm nominal spot size to ~150 μm. By doing so, any refraction effects due to the curved quartz tube were deemed negligible.

Chapter 5 Experimental Details

5.1 Electrode Preparation

Three different thin film electrodes were prepared by sputter deposition (see Section 4.1) for electrochemical testing using the method of Dahn et al. [65]. These included Si (p-type, 99.999% pure, Kurt J. Lesker Co.), Ni (99.9%, Advent Research Materials), and TiN (99.5%, Kurt J. Lesker Co.). All films were deposited onto cleaned 5.7 cm x 0.6 cm x 0.1 cm glass plate substrates (S.I. Howard Glass, MA, USA). The glass plates were cleaned in acetone, ethanol, and reverse osmosis water (NanoPure, 18.2 MΩ·cm) for 30 min each prior to deposition. Along with the glass substrates, 1.3 cm diameter Cu or Al foil discs and an 8.9 cm x 1.3 cm x 0.05 cm Si wafer ((100) orientation) were supplied for mass density and total film thickness characterization measurements, respectively.

To improve adhesion between the glass substrate and the thin film electrode, the substrates were plasma cleaned using a Cr plasma cleaner in O_2. The plasma cleaner bombards the substrate surface with an oxygen plasma and effectively removes any further organic contaminants present on the substrate surface through oxidation reactions. As the sputtering process is still occurring, however, a thin Cr layer is deposited onto the substrate. This Cr film is advantageous as it improves adhesion between the substrate and any sputtered layers above it (a "tie-layer"). An RF power supply was used to supply 50 W to the Cr plasma cleaner under a pressure greater than 10 mTorr of inflowing O_2 gas for a period of 10 min.

A constant amount of Ni (distributed radially over the length of the sputtering track) was deposited onto the glass plates after plasma cleaning. This ~700 nm thick film increased the conductivity of the electrodes during electrochemical testing and lowered the cell impedance.

Table 5.1 summarizes the sputtering targets used, the power supply provided (DC or RF), the pressure at which sputtering occurred, the process gas used, the power

supplied to the target, and the sputtering time for the three materials considered in this study. With the exception of the pure Ni electrode, an additional Ni layer was included for reasons listed above. The TiN target was sputtered in N_2 to increase the chance of TiN formation instead of elemental Ti.

Table 5.1 Sputtering conditions for the listed target materials. X (Si, TiN)/Ni indicates the sputtering conditions for the top layer X and the Ni layer, respectively.

Target Material	Power Supply Used	Target Power (W)	Process Gas	Sputtering Pressure (mTorr)	Sputtering Time (h)
Cr Plasma Cleaner	RF	50	O_2	>10	10 *min
Si/Ni	DC/DC	200/100	Ar/Ar	1.00/0.99	1/5
TiN/Ni	DC/DC	88/100	N_2/Ar	1.00/1.00	20.5/5
Ni	DC	100	Ar	1.00	5

*NB: different units

5.2 Electrode Characterization

After sputter deposition, several tests were performed to characterize the physical properties of the thin film electrodes. These included measurements of the deposited mass density from the weigh discs, measurements of the total film thickness of the film stack by profilometry, and the powder diffraction pattern obtained by x-ray diffraction (XRD). Figures 5.1-5.3 show the profilometry film thicknesses (a) and mass densities (b) for the Si, Ni, and TiN electrode materials, respectively. Also shown in Figures 5.1(a)-5.3(a) are calculated film thicknesses from the mass per unit area data (described below) and from SE measurements. Vertical dashed lines in the figures indicate the length of the glass substrate centred about the sputtering track. The profilometry measurements were performed with a Dektak 8 Advanced Development Profiler (Veeco Instruments Inc., USA) which dragged a 12.5 μm stylus across a Si wafer and recorded the variation in thickness. Half of a Si wafer was masked lengthways to produce a thickness "step" which could be analyzed by the profilometer. Mass densities of the deposited films were

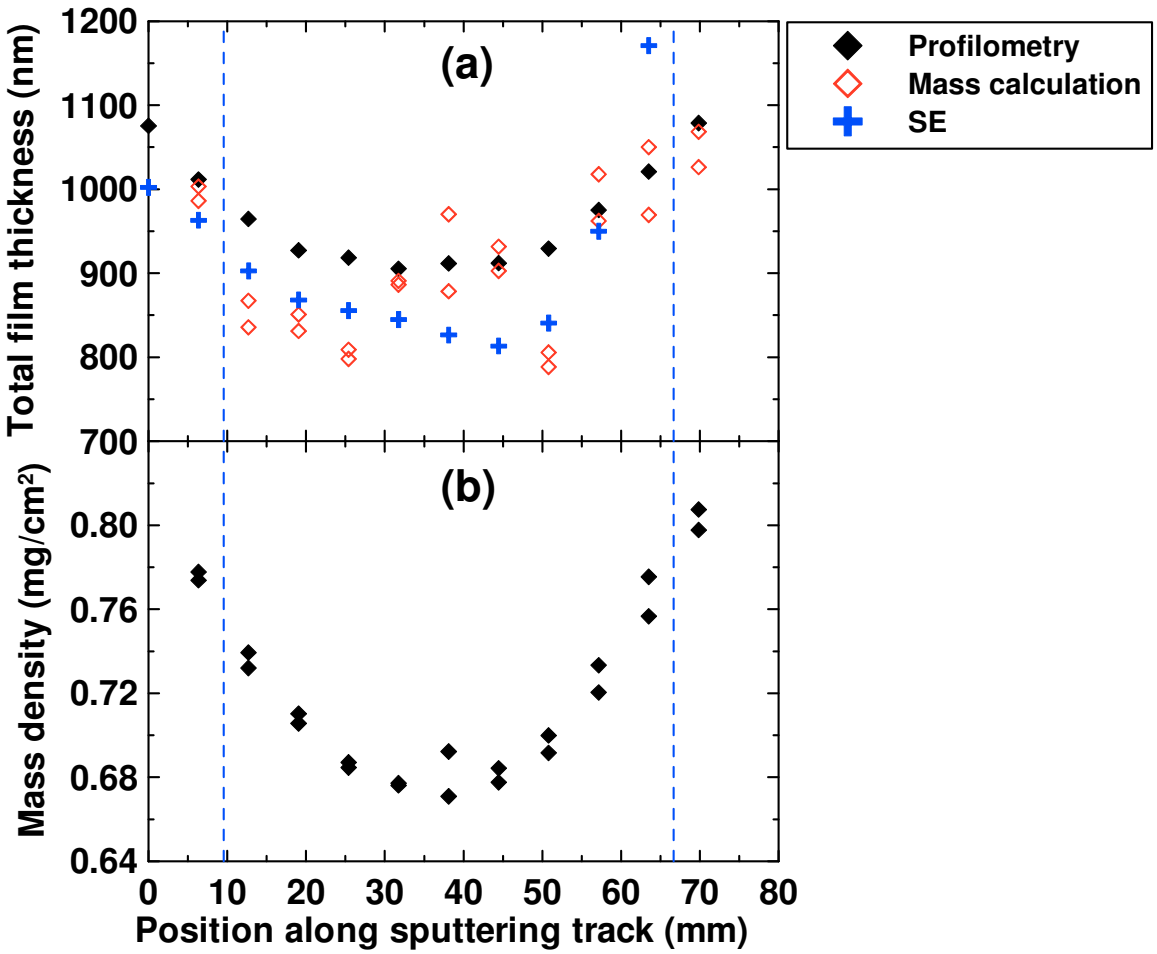

Figure 5.1 Total film thickness (a) and mass densities (b) of a a-Si sputter deposition along the length of the sputtering track. In (a), solid diamonds come from profilometry measurements, red open diamonds come from a calculation of electrode thickness using the bulk densities of a-Si and Ni and the mass densities, and blue crosses come from a SE measurement of a-Si thicknesses and profilometry thicknesses of a Ni film. Vertical dashed lines indicate the length of the glass substrates.

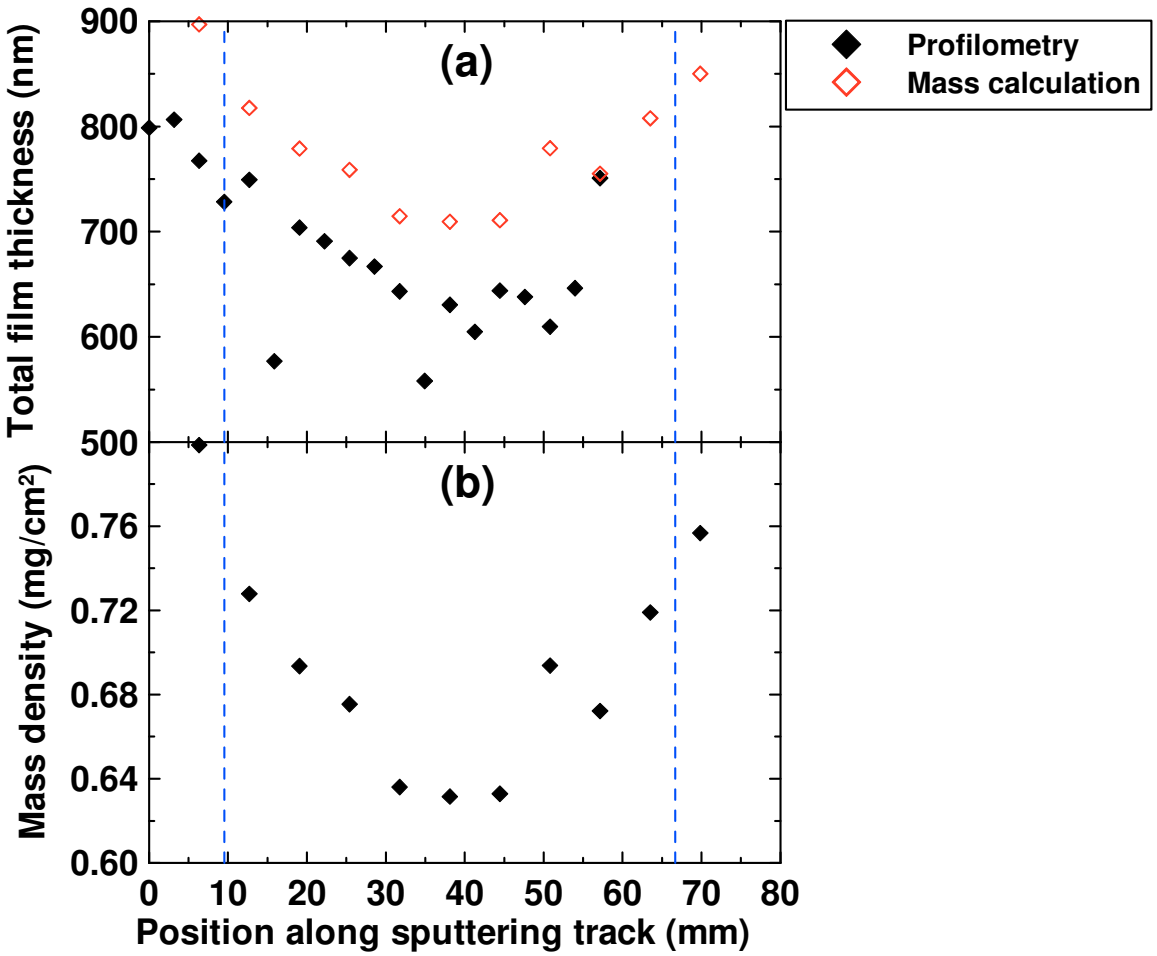

Figure 5.2 Total film thickness (a) and mass densities (b) of a Ni sputter deposition along the length of the sputtering track. Red open diamonds in (a) come from a calculation of electrode thickness using the bulk density of Ni applied and the mass densities. Vertical dashed lines indicate the length of the glass substrates.

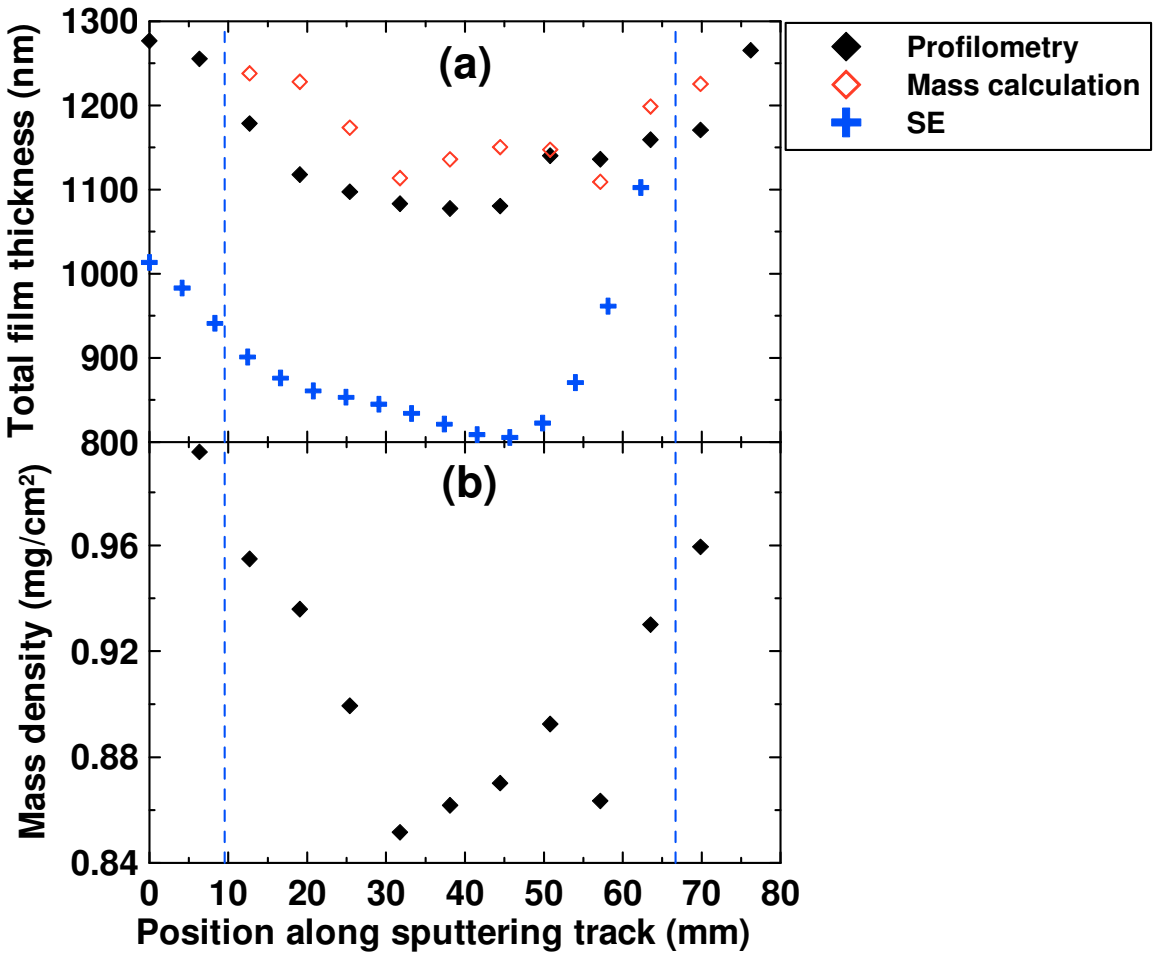

Figure 5.3 Total film thickness (a) and mass densities (b) of a TiN sputter deposition along the length of the sputtering track. In (a), solid diamonds come from profilometry measurements, red open diamonds come from a calculation of electrode thickness using the bulk densities of TiN and Ni and the mass densities, and blue crosses come from a SE measurement of TiN thicknesses and profilometry thicknesses of a Ni film. Vertical dashed lines indicate the length of the glass substrates.

determined by comparing the mass of 1.3 cm diameter Cu or Al foil discs before and after deposition. These discs were weighed using a Sartorius SE-2 microbalance with a resolution of ±0.1 μg.

In Figures 5.1-5.3, both the deposited mass densities and profilometry thicknesses exhibit a dip towards the centre of the sputtering track which is no more than ~15% of the original values. This matches many other sputter depositions using the "constant" mask and is merely a consequence of the calculated shape of the mask. The red open diamonds in Figures 5.1-5.3 show the expected film thicknesses based on the materials' bulk densities and the radial mass densities (it should be noted that a lot of materials do not sputter at their bulk densities, so this assumption is a great simplification). The blue crosses in Figures 5.1(a) and 5.3(c) are film thickness measurements based on SE measurements of the surface film and the profilometry measurements of the Ni film. In Figures 5.1(a) and 5.3(a), there is some mismatch between profilometry measurements and calculated thicknesses from mass. This mismatch arises from simplifying assumptions made in the calculation. In Figure 5.1(a), the mass per unit area results of the elemental Ni electrodes were subtracted from the mass per unit area of the Si/Ni thin films. The difference was assumed to be the mass per unit area of deposited Si. From the mass data, the thickness of the Ni and Si components were calculated separately and summed. Clearly, the Ni thicknesses between depositions differ and do not reflect the true thickness of the Si/Ni electrode. In Figure 5.3(a), the thickness measurement using SE underestimates the total film thickness from profilometry measurements. Again, the thickness of the Ni layer in Figure 5.3 is not guaranteed to be the same as the Ni thickness in Figure 5.2(a). This gives rise to the observed discrepancy.

Figures 5.4(a)-5.4(c) show XRD data taken from the Si (a), Ni (b), and TiN (c) thin film electrodes with appropriately labeled Miller indices. These data were taken using an INEL CPS120 x-ray diffractometer emitting Cu Kα radiation equipped with a curved detector and translation stage. Counts were collected for 1200 s per point. In Figures 5.4(a) and 5.4(c), Ni peaks dominated the XRD patterns. The overlying films were very thin, thus the x-rays penetrated through and diffracted largely from the Ni film. It has been shown (for example, Ref. [69]) that Si deposited by magnetron sputtering is amorphous with very broad XRD powder patterns. In Figure 5.4(a), only the Ni peaks

are observed as the amorphous-Si (a-Si) does not diffract strongly relative to Ni. It is interesting to see several diffraction peaks in Figure 5.4(c) corresponding to the (111), (220), and (222) reflections of the cubic TiN structure. It is reasonable to conclude that crystalline TiN was formed during deposition by the presence of these peaks.

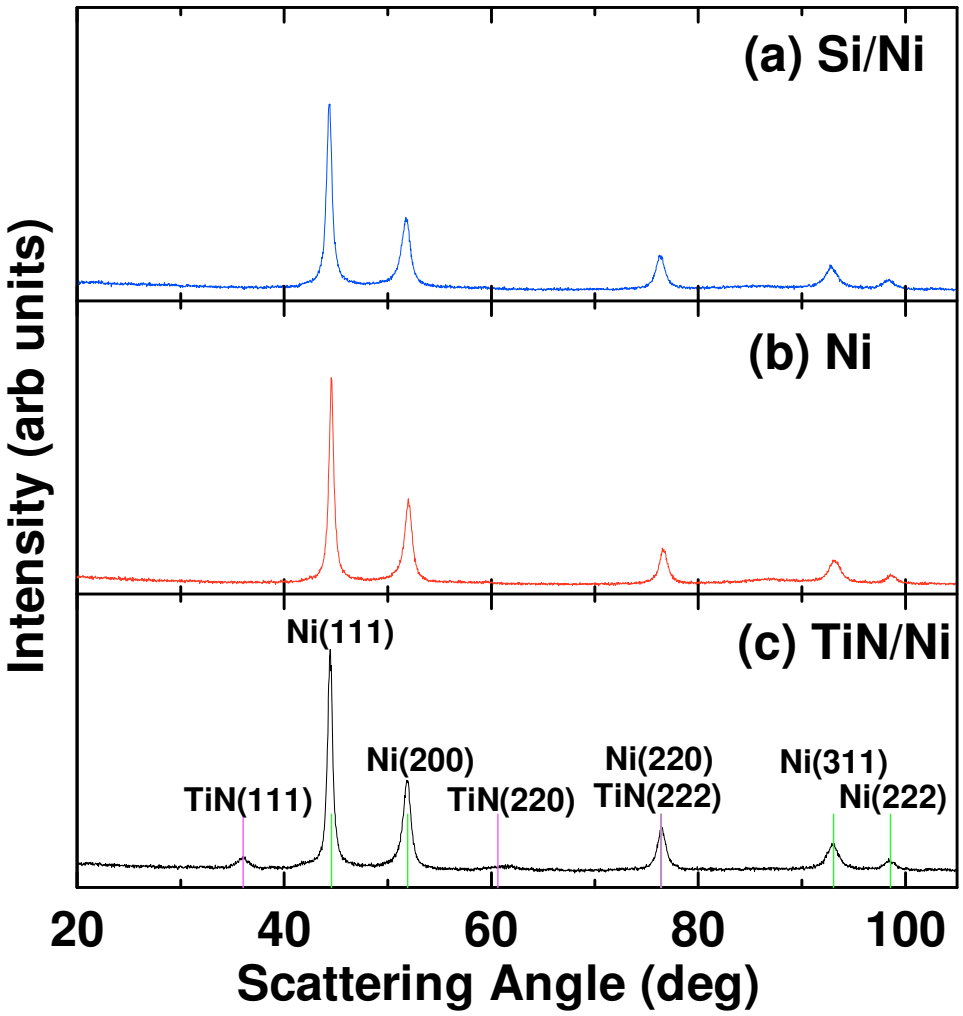

Figure 5.4 X-ray diffraction data for three electrodes used for SEI investigations. From (a)-(c), these include a sputtered Si electrode on Ni, a sputtered Ni electrode, and a sputtered TiN electrode on Ni. The Ni peaks are prevalent in both (a) and (c) and very little presence of the overlying layer was observed.

5.3 Electrochemical and Spectroscopic Ellipsometry Testing

The in-situ cell was carefully constructed within an Ar-filled glove box to minimize exposure to air and/or moisture. The cell was then filled with one of four electrolytes: 0.1 M $LiPF_6$/EC:DEC (1:2), 1 M $LiPF_6$/EC:DEC (1:2), 1 M $LiPF_6$/EC:DEC (1:2)/2 wt.% VC, or 1 M $LiPF_6$/EC:DEC (1:2)/2 wt.% FEC (Novalyte Technologies, USA). Once filled, the cell was carefully removed from the glove box and fixed to the custom-machined ellipsometer mounting stage by key and keyway combination and a

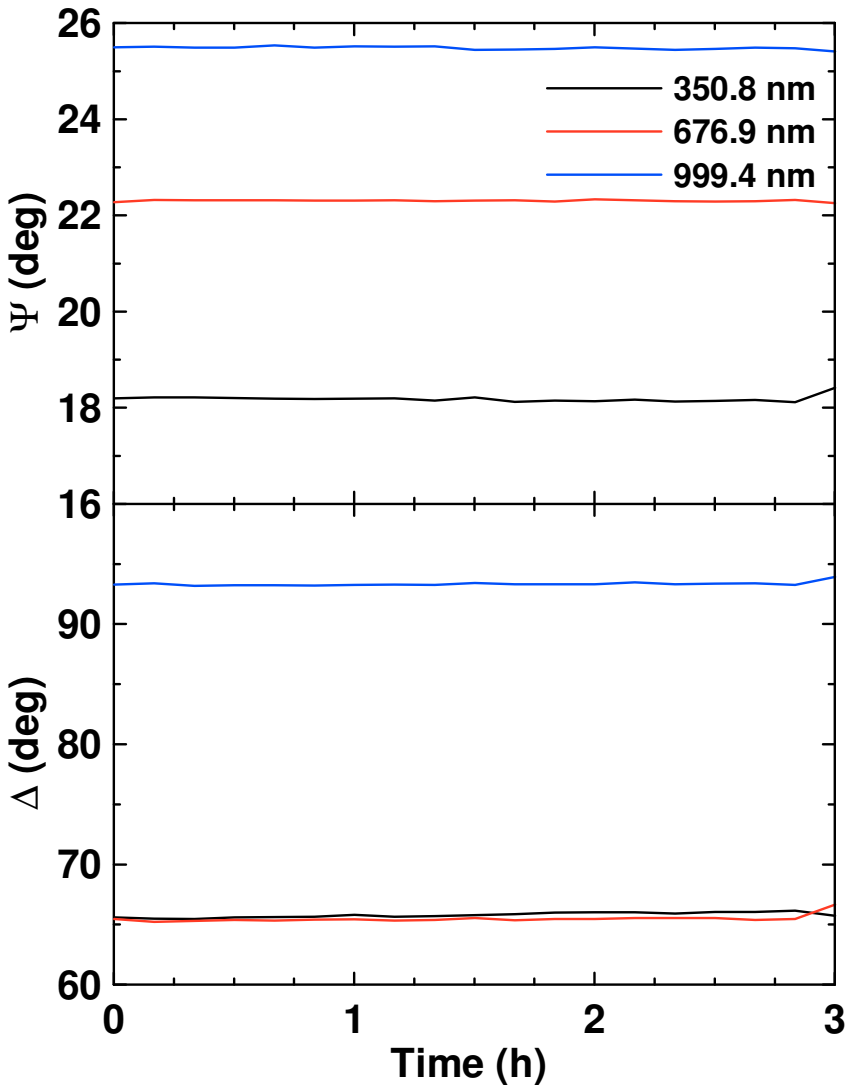

Figure 5.5 Time dependence of the ellipsometric parameters, Ψ and Δ, for 3 wavelengths during a 3 hour equilibrium period for an in-situ cell with a TiN working electrode at open circuit.

clamp system. The software CompleteEASE [70] was then used to align to a single spot on the electrode using the ellipsometer. A continuously measuring scan was set up to perform an ellipsometric measurement every 10 min. The thin film electrode and cell were left at open circuit for 3 hours to ensure the electrode and electrolyte came to equilibrium. Figure 5.5 shows the time dependence of the ellipsometric parameters, Ψ and Δ, of a TiN working electrode in contact with 1 M $LiPF_6$/EC:DEC (1:2) during the 3 hour equilibration period for 3 wavelengths. This equilibrium period was found to be necessary as the film's optical characteristics changed after exposure to a liquid medium, as was found in previous in-situ SE work [71]. In the case of the TiN working electrode, there was very little change observed in the optical properties of the material at open circuit. Following the equilibrium period, one of two electrochemical studies began. These tests included cycling the in-situ cell with a constant current or holding the cell at a constant potential. The next two subsections discuss each in greater detail.

5.3.1 Constant Current Testing

The constant current testing of the in-situ electrochemical cell was performed using a Keithley 220 programmable current source and a Keithley 2000 digital multimeter in a similar fashion as the high precision battery charger system located at Dalhousie University [72]. These devices were controlled using LabView software. The constant current measurements were performed at room temperature (between 20-25ºC) as follows:

> The positive and negative terminals of the in-situ cell were connected in series to the current source. A digital multimeter read the voltage across the cell leads in parallel. The setpoint current was chosen to provide a 10 hour charge and 10 hour discharge (C/10) cycle as calculated based on the specific capacities of the electrode materials. When energized, the load current was applied and the cell's voltage, as recorded by the digital multimeter, was allowed to vary between two predetermined limits (typically between 0.005 V-1.2 V). Once the lower voltage

limit was reached, the current source reversed, charging the cell until the upper voltage limit was reached. The process was repeated until several complete discharge/charge cycles were performed. The voltage-time data was simultaneously logged by the in-house software and saved for future analysis. Using additional in-house software, the voltage-time data was converted to voltage-capacity data.

5.3.2 Constant Potential Testing

The constant potential testing of the working electrode within the in-situ cell was performed using a Keithley 236 source-measure unit. Similar to the constant current testing, these experiments were conducted at room temperature (20-25ºC). The measurements were performed as follows:

The in-situ cell was connected to the negative and positive leads of the source-measure unit. Using in-house software, a series of potential hold "steps" and their durations were set, as well as the data acquisition rate. Once initialized, the Keithley 236 held the cell at the setpoint potential and varied the current to maintain a constant potential for the indicated duration. After this time, the source-measure unit stepped to the next setpoint potential and varied the current for the indicated duration. This process repeated for 6 steps in total and the current-time data were exported to a spreadsheet for future analysis. Typically, potential steps varied from 1.0 V, 0.5 V, 0.1 V, 1.0 V, 2.0 V, and 3.0 V in that order for 10 hours each while ellipsometric data was recorded simultaneously. This test was performed to study the behaviour of electrolyte additives on the growth of the SEI layer formed on a TiN thin film working electrode versus Li-metal.

5.4 Optically Modeling SE Data

Spectroscopic ellipsometry is an indirect form of measuring thicknesses or optical constants (as well as several other physical properties) of thin film materials. From a measurement of Ψ and Δ, it is necessary to build the proper optical model to extract physically meaningful quantities of interest. The process of selecting, developing, and refining the model is nontrivial. These models work best when many properties of the system in question are known, such as composition, roughness, etc. Unfortunately, in an in-situ-type experiment, every detail about the system is not readily available. In this section, a discussion of the methods used in selecting the proper optical models is presented. In later chapters, the validity of these optical models will be discussed.

Generally, modeling of ellipsometric data is performed using sophisticated SE software such as CompleteEASE. For the case of CompleteEASE, the Marquardt-Levenberg algorithm (whose method is best described in mathematical texts on data fitting [73, 74]) is employed to find the best agreement between the model and experimental data. An optical model is best described visually as a cross-section of the sample made of "rectangular slabs" of thickness x which represent the (n, k) optical constant pairs of the material. These slabs can be stacked in such a way to describe the sample completely. Figure 5.6 depicts an example of a 2-phase optical model for a Si wafer and its native oxide. Here, the optical constants are depicted as functions which depend on the wavelength of the probing beam.

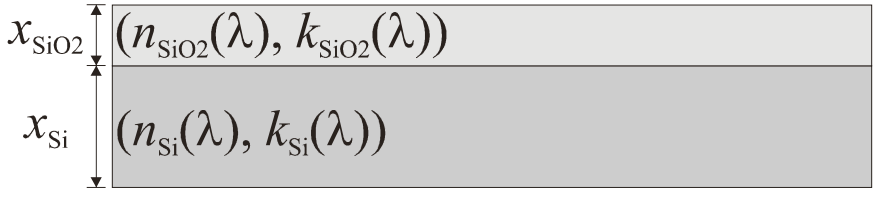

Figure 5.6 A simple 2-phase optical model consisting of a Si substrate and its native SiO_2 oxide. The thicknesses and wavelength-dependent optical constants of each layer are given by $x_{(SiO2,\ Si)}$ and $(n_{(SiO2,\ Si)}(\lambda), k_{(SiO2,\ Si)}(\lambda))$ for SiO_2 and Si, respectively.

For thin, optically transparent media, such as a surface film grown during an electrochemical reaction, a set of optical constants can be determined from the ellipsometric Ψ and Δ parameters. These films can be described by a dispersion relation, whereby the optical constants are allowed to vary with wavelength in a very specific way. One of the most simple and most useful dispersion relations used for modeling SE data is known as the Cauchy dispersion model. A Cauchy layer can be applied whenever a transparent surface layer with unknown refractive index or thickness is required to properly model a sample.

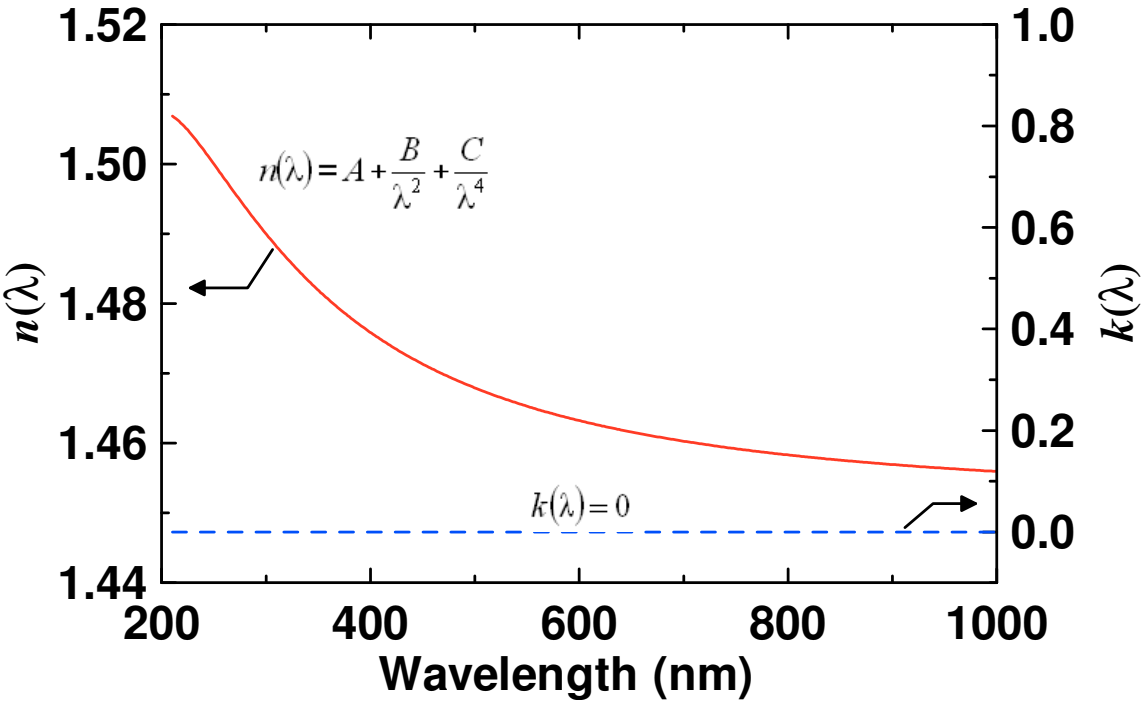

Figure 5.7 Cauchy dispersion curve describing the real part of the refractive index of a transparent SiO_2 film with respect to wavelength. The *A*, *B*, and *C* parameters used in the Cauchy equation (Eq. (5.1)) are 1.452, 0.00443 nm^2, and -8.78×10^{-5} nm^4, respectively. The film is assumed to be completely transparent such that $k \sim 0$ for all wavelengths.

Figure 5.7 shows a typical Cauchy dispersion curve for SiO_2 with the real part of the refractive index given by the full red curve and the imaginary part of the refractive index given by the dashed blue curve. Typically, a 3- (or more-) parameter dispersion relation is used with the functional form

$$n(\lambda) = A + \frac{B}{\lambda^2} + \frac{C}{\lambda^4} \tag{5.1}$$

where $n(\lambda)$ is the real part of the refractive index as a function of wavelength and A, B, and C are adjustable parameters which shape the curvature of $n(\lambda)$. In Figure 5.7, A, B, and C are given by 1.452, 0.00443 nm^2, and -8.78×10^{-5} nm^4, respectively. A Cauchy relation such as Eq. (5.1) can be written for the imaginary part of the index of refraction; however, as Eq. (5.1) is used to describe transparent films, it follows that $k\sim0$ for all wavelengths. It is possible to determine some information about k using a Cauchy model using other complex methods beyond the scope of this thesis. Suffice it to say, however, that these complexities are handled easily as additional adjustable parameters within SE analysis software.

The general modeling procedure for measurements performed in this thesis was as follows:

1. the (n, k) pairs for the liquid ambient electrolyte were measured,
2. the (n, k) pairs for the surface film (SEI) were measured,
   a. the in-situ cell was constructed with a TiN electrode with 1 M $LiPF_6$/EC:DEC (1:2) as the electrolyte,
   b. the (n, k) pairs for the baseline TiN electrode were measured after a 3 hour equilibrium period,
   c. the cell voltage was held constant at 0.1 V for 48 hours, and
   d. a Cauchy dispersion layer was used to fit both thickness and the real part of the refractive index, n, simultaneously.
3. the (n, k) pairs for the baseline electrode material were measured after a 3 hour equilibrium period,
4. a surface layer described Eq. (5.1) with optical constants from Step 2(d) was added to the model whose thickness could be fit for the duration of the experiment.

5.4.1 Refractive Indices of Nonaqueous Electrolyte

To determine the refractive indices of the liquid electrolyte, roughly 1-2 mL of electrolyte was placed onto a roughened glass plate. The plate was roughened to ensure no back-side reflections were observed by the reflected ellipsometer probe beam causing unwanted interferences and hence inaccurate optical measurements. For this measurement, the ellipsometer focusing optics were removed to maximize the intensity of the reflected beam from the surface of the electrolyte droplet. The ellipsometric parameters were modeled using a simple Cauchy dispersion layer, allowing the *A* and *B* parameters to vary (with $C = 0$). This measurement was performed for electrolytes with and without additives.

5.4.2 Refractive Indices of the SEI

To determine the optical constants of the SEI film, the in-situ cell was constructed and filled with 1 M $LiPF_6$/EC:DEC (1:2). During a 3 hour equilibrium period where the cell rested at open-circuit, the ellipsometer performed a measurement in 10 min intervals. After the equilibrium period, the cell was held at 0.1 V for 40 hours. The data point just before the 0.1 V hold was analyzed to extract the set of optical constants for the TiN working electrode.

To model the TiN working electrode, a dispersion relation called a Lorentz oscillator model was used. An oscillator layer models response of a material's dielectric polarization to an oscillating electric field. The mathematics of oscillator models is very similar to that of the solution for mechanical oscillators and many named oscillator functions are available in SE analysis software packages. For the TiN films under study, a series of three Lorentz oscillators adequately describes the interactions with the probing beam in the optical model [75, 76]. Mathematically, these oscillators are of the form

$$\varepsilon(\mathrm{En}) = \varepsilon_1 - i\varepsilon_2 = \varepsilon_\infty - \frac{\mathrm{A}_1}{\mathrm{En}^2 - i\gamma_1 \mathrm{En}} + \sum_{j=2}^{3} \frac{\mathrm{A}_j}{\mathrm{En}_{0j}^2 - \mathrm{En}^2 + i\gamma_j \mathrm{En}} \tag{5.2}$$

where $\varepsilon(En)$ is the complex dielectric constant as a function of photon energy, En ($En = \hbar\omega$), and ε_∞ is an offset dielectric constant and is a variable parameter. The other terms are the Lorentz oscillators with adjustable parameters $A_{(1, 2, 3)}$, $\gamma_{(1, 2, 3)}$, and $En_{0(2, 3)}$ which are the oscillator amplitudes, broadening, and oscillator positions, respectively. Note that the second term has $En_{01} = 0$. This is the general form of a Drude oscillator and takes into account conduction electrons and free carriers in the low energy range of conductive dielectrics. The remaining Lorentz terms account for higher energy photon absorption in the material. Once the TiN baseline optical constants were determined, they were fixed for the duration of the measurement. This is a reasonable assumption as it has been shown that TiN is relatively inert with Li [20, 21].

To model the SEI component in the optical model, a Cauchy dispersion layer was used. In the model, parameters corresponding the *A* and *B* in Eq. (5.1) were varied simultaneously with the thickness of the layer. In this way, both the real part of the refractive index as well as the thickness of the SEI could be established. This analysis was performed after a potential hold at 0.1 V for roughly 48 hrs. It was assumed that after this time, the SEI would be at its thickest and that the refractive index-thickness coupling affect could be resolved to allow for an accurate determination of both quantities in the multi-parameter fit. These values obtained for the Cauchy parameters were used for the duration of the study.

5.4.3 Modeling the Baseline and Extracting Surface Film Thickness

The baseline of each working electrode material was matched after the 3 h equilibrium period at open-circuit within the in-situ cell. For each material, a different baseline model was chosen.

For the sputtered a-Si, a general oscillator layer was selected, consisting of two Tauc-Lorentz oscillators [77, 78]. These oscillators are more general versions of Lortenz oscillators as described above, with additional adjustable parameters. It should be noted, however, that the Si system is much more complex than other simple systems such as Ni and TiN. During lithiation, Si exhibits a large volume expansion, thus the thickness of

the Si layer is always changing during cycling. Also, as the Li-Si alloy is formed, the electrode's optical properties change from a material which is partially optically transparent to a material with metallic character. These properties alone make modeling of any surface layer developed during cycling very challenging. However, useful information can still be gained from the Si electrode measurements; this will be discussed in greater detail in Chapter 6.

The Ni electrode was modeled simply using a basis (B)-spline layer [79]. This specialized layer is used to obtain optical constant information based on user-defined control points (nodes) matched to the measured ellipsometric parameters. Optical constants are matched by varying the nodes in such a way as to maintain smooth and continuous wavelength dependence. The B-spline layer is typically used to determine the optical constants of a metal thin film [79]. It should be noted that any metal oxide present is difficult to model using the B-spline and that the recorded optical constants include contributions from both the metal and its oxide. Conveniently, the optical constants of metals such as Ni do not vary greatly with or without the presence of their native oxide layer.

Modeling of the TiN electrode baseline was described above, as was the modeling of the SEI layer. During the charge/discharge cycling and voltage holds, the Cauchy parameters of the SEI film were fixed and the SEI layer thickness was allowed to vary. In this way, a plot of SEI thickness versus time was extracted from the data.

Chapter 6 Results and Discussion

6.1 Preliminary Optical Measurements

6.1.1 Optical Properties of Bare Electrode Materials

To obtain the best fitting results using the SE analysis software, it was necessary to examine each component of an optical model separately. Ellipsometry is an indirect form of measurement and requires a great deal of preliminary knowledge about the sample to extract meaningful results. Fitting parameters can be extracted from the ellipsometric data by determining the optical properties of each component within the full model. This section will address issues pertaining to extracting physical results for further data analyses.

Figure 6.1 shows data for the amplitude ratio, Ψ, and phase difference, Δ, of an a-Si thin film electrode measured in air (open circles). Every third data point is shown for clarity. The red and blue curves show the results of a fit using two different optical models (Model 1 and Model 2, respectively). As introduced in Chapter 5, both models use the Tauc-Lorentz oscillator relation to model the a-Si layer on top of a Ni film. Model 1 uses a single oscillator whereas Model 2 uses two Tauc-Lorentz oscillators. Table 6.1 shows the results of the adjustable parameters after the fit and their MSEs. The thicknesses of the a-Si and SiO_2 films from Model 1 are 202.2 ± 0.3 nm and 1.95 ± 0.06 nm, respectively. From Model 2, these thicknesses are 201.6 ± 0.2 nm and 1.93 ± 0.03 nm for a-Si and SiO_2, respectively. These film thicknesses are the same within error. However, in Figure 6.1, there is some mismatch between the fit and the data for Model 1 at longer wavelengths (above ~860 nm). An MSE of 12.3 is obtained for Model 1 compared to an MSE of 5.9 for Model 2. Because of the MSE reduction of roughly half with only a minor adjustment to the a-Si layer, Model 2 is preferred. Moreover, with the addition of further Tauc-Lorentz oscillators, only a modest decrease in the MSE is

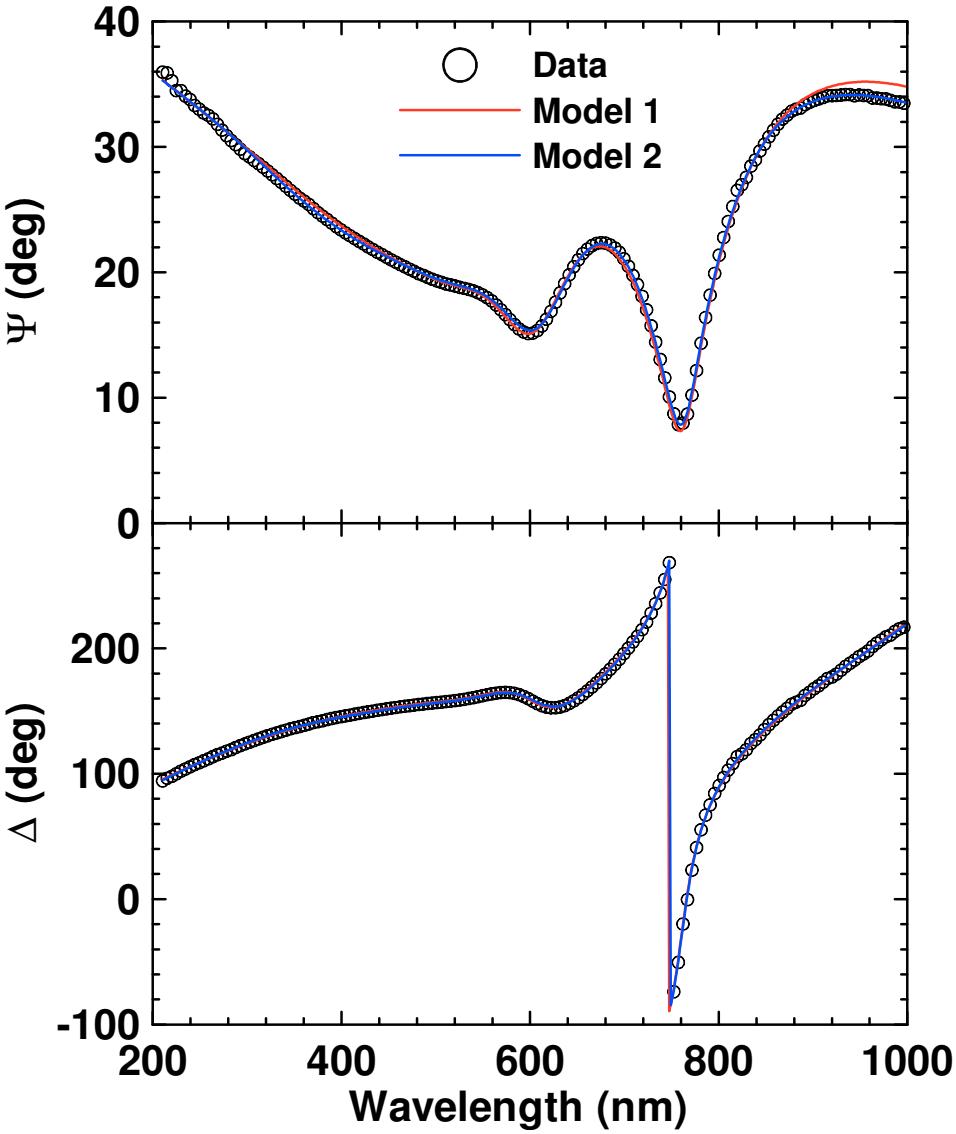

Figure 6.1 Ellipsometric parameters (open circles), Ψ and Δ, and the corresponding fitting results from two optical models for a bare a-Si thin film electrode measured in air. Model 1 (red curve) uses a single Tauc-Lorentz oscillator whereas Model 2 (blue curve) uses a 2-term Tauc-Lorentz oscillator. Every third data point is shown for clarity.

observed (fits not shown). Therefore, Model 2 allows for physical thickness results and an MSE which is minimized with a reasonably simple model.

In a study by Jellison and Modine, it was shown that the Tauc-Lorentz oscillator models the ellipsometric parameters of amorphous semiconductors excellently [77]. In

particular, two data sets of a-Si films were measured and analyzed using 3 optical models, including the Tauc-Lorentz oscillator. It was found that the MSEs of the fits to the a-Si data sets using the Tauc-Lorentz oscillator model were very low (5.2 and 1.0 for the data sets from Ref. [80] and Ref. [81], respectively). It should be noted that Jellison and Modine only used a single oscillator to obtain their excellent agreement. Also, in Ref. [80], for example, a-Si thin film samples were prepared by chemical vapour deposition on oxidized Si wafers. In this thesis, a-Si thin films were prepared by magnetron sputtering on a thick layer of Ni. As the sample preparation was not identical, other variables may be required to correctly model the a-Si layer. This was done by inclusion of the second Tauc-Lorentz oscillator which dramatically reduced the MSE.

Table 6.1 Fitting parameters for two models from bare a-Si thin film electrodes measured using spectroscopic ellipsometry in air. Model 1 gives parameters from a single Tauc-Lorentz oscillator. Model 2 gives the parameters from a 2-term Tauc-Lorentz oscillator.

Parameter (unit)	Model 1	Model 2
MSE	12.3	5.9
SiO_2 Thickness (nm)	1.95 ± 0.06	1.93 ± 0.03
a-Si Thickness (nm)	202.2 ± 0.3	201.6 ± 0.2
ε_∞	0.99 ± 0.05	1.18 ± 0.04
A_1 (eV)	142.8 ± 0.9	83 ± 4
C_1 (eV)	2.37 ± 0.02	2.62 ± 0.06
E_{01} (eV)	3.523 ± 0.007	3.04 ± 0.03
E_{g1} (eV)	1.130 ± 0.002	1.392 ± 0.009
A_2 (eV)		70 ± 3
C_2 (eV)		2.12 ± 0.02
E_{02} (eV)		3.72 ± 0.01
E_{g2} (eV)		0.92 ± 0.01

Figure 6.2 shows the ellipsometric parameters, Ψ and Δ, (open circles) and fitting results (red curve) to a Ni film prepared by magnetron sputtering. Every third data point is shown for clarity. A B-spline was used to model the optical constants of the layer with an overall MSE of 1.3. The B-spline model is useful when determining optical constant information alone, as is the case for the Ni electrodes prepared in this thesis. This is

particularly useful for thick reflective metals as typically only refractive index information can be gained. The B-spline model matches ellipsometric data by varying polynomial splines while maintaining smoothness [79]. The B-spline model is a mathematics-based fitting approach (whereas the oscillator models are based on the physical interaction of the material with light). However, it is useful for determining the

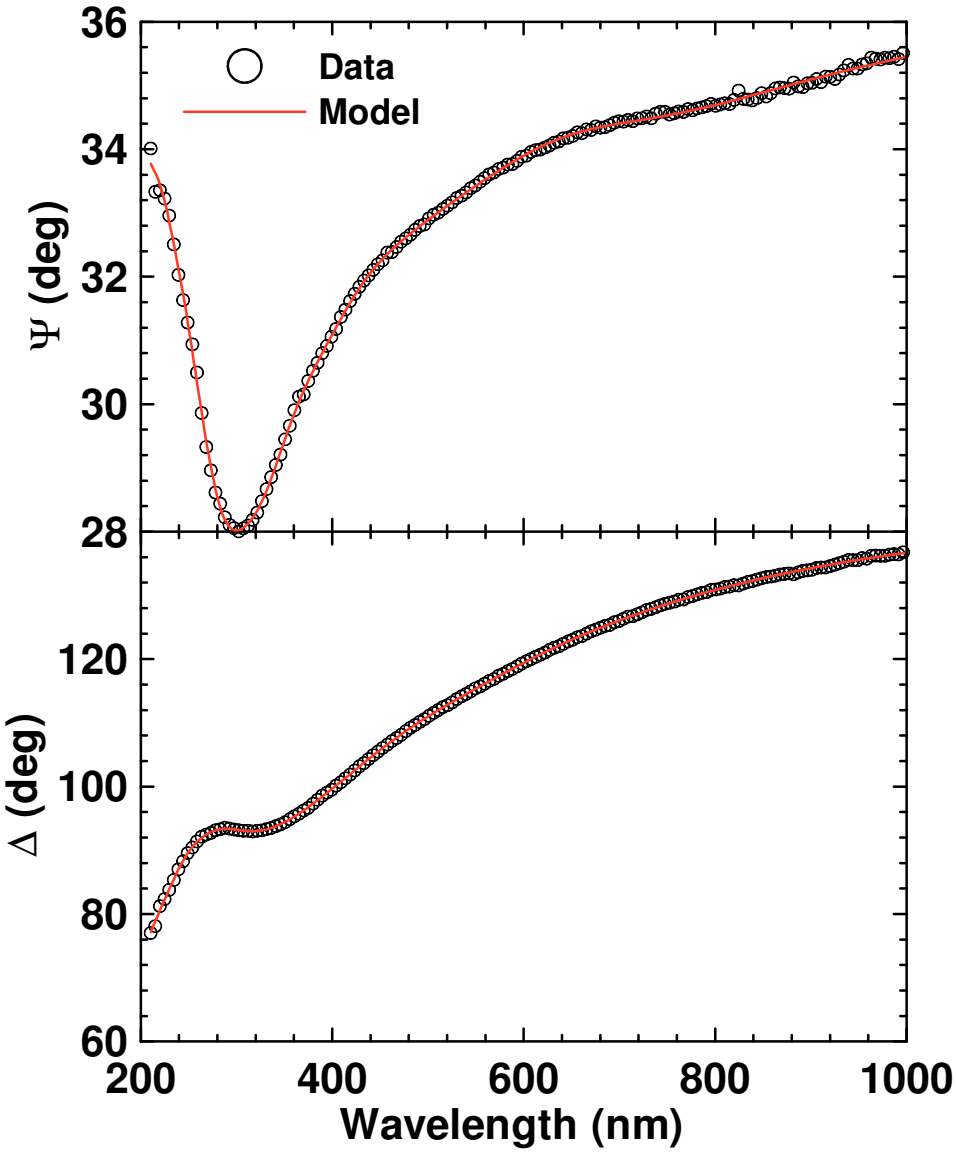

Figure 6.2 Ellipsometric parameters (open circles), Ψ and Δ, and the corresponding fitting results from an optical model for a bare Ni thin film electrode measured in air. The model (red curve) uses the basis- (B-)spline method to determine the complex indices of refraction of the Ni film. Every third data point is shown for clarity.

complex refractive indices of a sample quickly and easily. Because the technique varies control nodes to mathematically match the data at every wavelength, a very low MSE is expected. From the fit, the underlying (n, k) pairs for the Ni layer were extracted and used to model the Ni layer in further optical models.

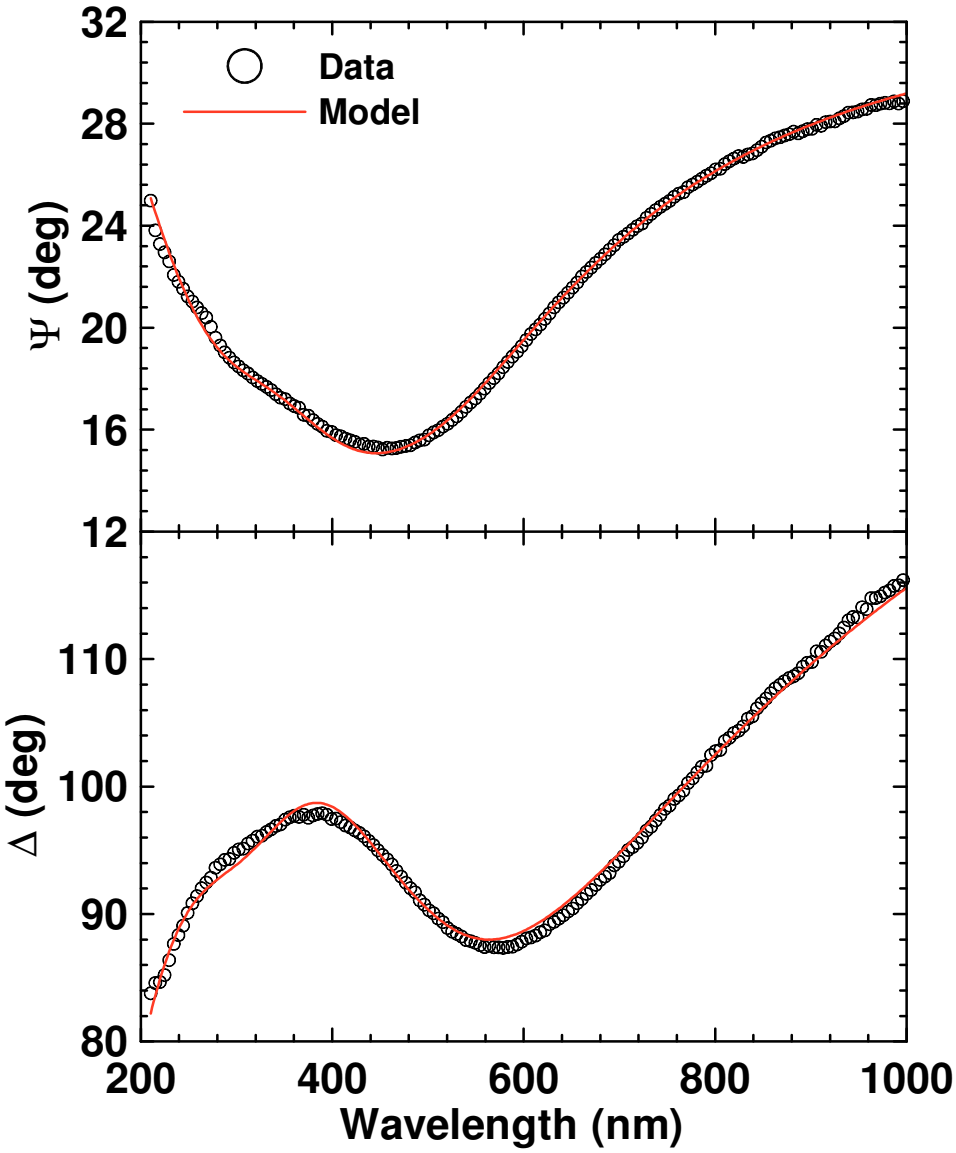

Figure 6.3 Ellipsometric parameters (open circles), Ψ and Δ, and the corresponding fitting results from an optical model for a bare TiN thin film electrode measured in air. The model (red curve) uses a single Drude oscillator and two Lorentz oscillators to determine the complex indices of refraction and thickness of the TiN film. Every third data point is shown for clarity.

Figure 6.3 shows the ellipsometric parameters, Ψ and Δ, (open circles) and fitting results (red curve) to a TiN film prepared by magnetron sputtering. Every third data point is shown for clarity. A Drude oscillator was used in series with two Lorentz oscillators to model the TiN film correctly. It has been shown by Patsalas and Logothetidis that this model describes the ellipsometric data excellently [75, 76]. In the studies of Patsalas and Logothetidis, TiN_x thin films were prepared by reactive magnetron sputtering (essentially, sputtering a Ti target in N_2 gas to produce TiN_x films) to determine physical and optical properties using SE. The optical model described above was used to extract information about the band structure of the deposited film. The Drude term in the model was included to describe the optical response of the metallic Ti 3*d* conduction electrons, whereas the two Lorentz oscillators were used to extract information about the TiN_x interband transitions. These properties of TiN are interesting, however beyond the scope of this thesis. The information pertinent to the current study was the film thickness and optical constants of the TiN electrode, which were determined accurately by the model. Table 6.2 summarizes the fitting results from the optical model. The MSE of the model was typically no more than 6 which is reflected by very good

Table 6.2 Fitting parameters for a model used to determine the optical properties and thickness of a bare TiN thin film electrode measured by spectroscopic ellipsometry in air. To model the TiN electrode, a single Drude-type and two Lorentz-type oscillators were used.

Parameter (unit)	Value
MSE	5.5
TiN Thickness (nm)	200 ± 17
ε_∞	2.57 ± 0.03
A_1 (eV)	37.5 ± 0.1
γ_1 (eV)	1.160 ± 0.006
A_2 (eV)	133 ± 5
γ_2 (eV)	4.4 ± 0.1
E_{02} (eV)	5.41 ± 0.02
A_3 (eV)	16 ± 2
γ_3 (eV)	1.87 ± 0.09
E_{03} (eV)	3.41 ± 0.02

agreement between the experimental data and the model curve in Figure 6.3. A MSE of 5.5 was determined for the data point on the TiN film presented in Table 6.2. At the position measured, a TiN thickness of 200 ± 17 nm was obtained. The background constant, ε_∞, was determined to be greater than 1. This is due to contributions of higher-energy transitions not taken into account in the Lorentz terms [76].

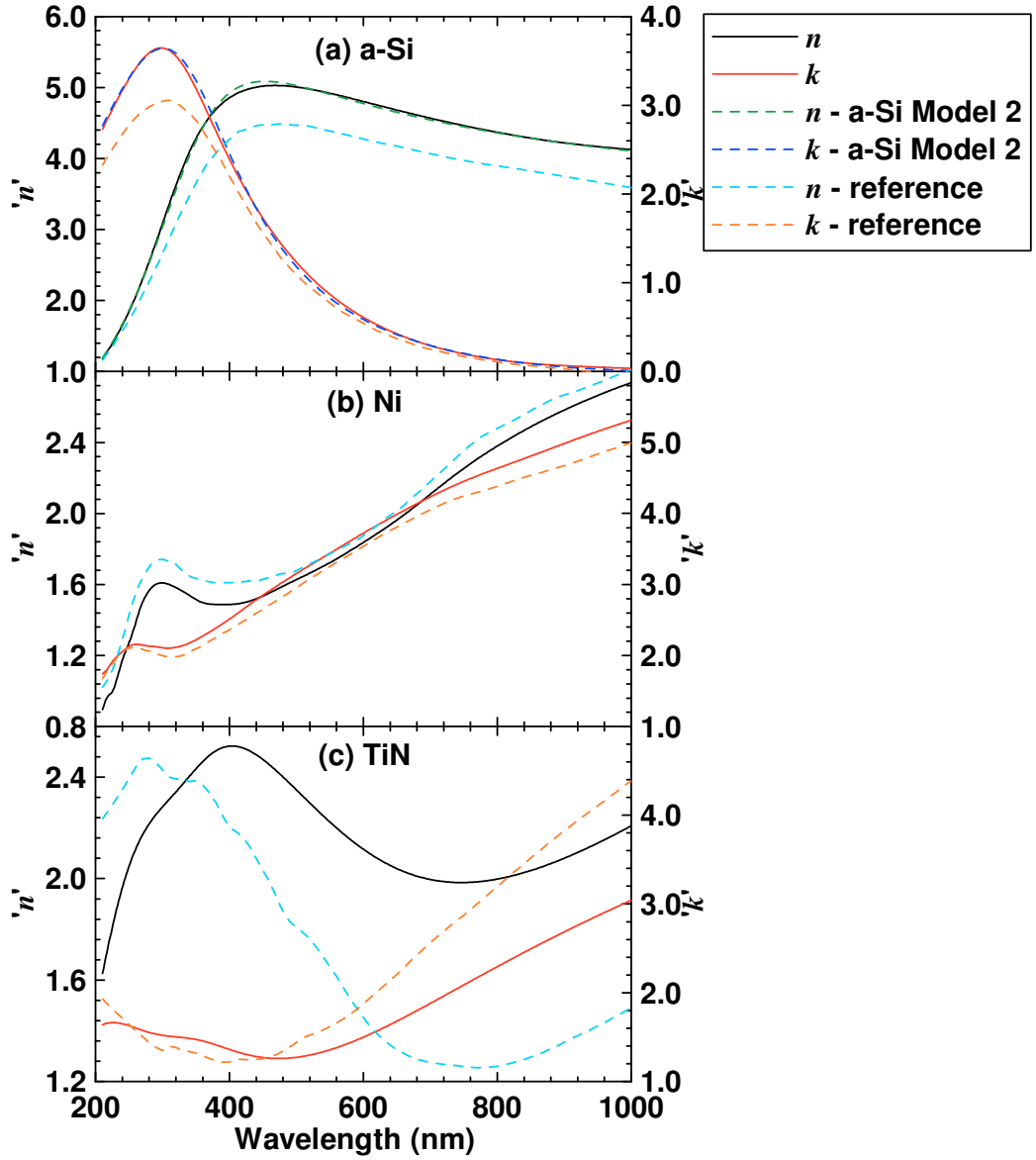

Figure 6.4 Optical constant (n, k) for the a-Si (a), Ni (b), and TiN (c) thin film electrodes determined from the optical models for each electrode in air. For the a-Si electrode, the results for two different optical models are shown. Dashed blue and orange curves indicate the optical constant values from reference materials incorporated within the CompleteEASE SE analysis software.

Figures 6.4(a)-6.4(c) summarize the results of the complex refractive indices from the optical models for a-Si (a), Ni (b), and TiN (c) thin film electrodes. In the case of a-Si, the results of Model 1 and Model 2 are shown (as dashed green and dark blue curves for n and k, respectively). For comparison, the (n, k) pairs of reference materials are shown (as dashed light blue and orange curves for n and k, respectively) for each electrode. The reference values came from a material library built into the SE analysis software [70]. There is some discrepancy between the measured and the reference values. Typically, the reference complex refractive indices come from bulk materials or films which have been produced under different conditions than those produced in this study. Therefore, one would not expect to obtain the exact values unless the sample conditions were identical. However, it is reassuring to observe the same general shape between the reference and experimental ($n(\lambda)$, $k(\lambda)$) pairs. In Figure 6.4(a), the refractive indices obtained for both Models 1 and 2 are nearly identical. This further validates the use of either model to fit data from the a-Si electrode. For the case of the Ni thin film in Figure 6.4(b), the observed shift in the (n, k) pairs away from the reference may be due to any surface oxide present. Typically, it is difficult to resolve the contributions to Ψ and Δ from a metal and its native oxide; as such, both are included together in the optical model (such as the B-spline). In Figure 6.4(c), a large refractive index mismatch between measured and reference (n, k) pairs is observed. The refractive index of TiN films is apparently dependent on sputtering conditions (pressure, gas flow rate, etc.) and film thickness [75, 76, 82] and as such, the index mismatch is not problematic for further data analyses.

6.1.2 Optical Properties of Electrolyte and SEI

Figure 6.5 shows the index of refraction and extinction coefficient of the various electrolytes used throughout the electrochemical testing. These curves were determined using a Cauchy dispersion relation by measuring 1-2 mL of electrolyte on a roughened glass plate by SE. The refractive index of 0.1 M $LiPF_6$/EC:DEC (1:2), 1 M $LiPF_6$/EC:DEC (1:2), and 1 M $LiPF_6$/EC:DEC (1:2)/additive (additive is 2% by weight

VC or 2% by weight FEC) electrolytes varied between 1.391-1.409, 1.410-1.433, and 1.411-1.438, respectively. Table 6.3 shows the fitting parameters used to determine the real part of the refractive index for the electrolytes. Only *A* and *B* parameters were varied in the Cauchy dispersion relation (Eq. (5.1)). In the Cauchy model, the extinction coefficient was taken as zero for all wavelengths, as emphasized in Figure 6.5 by a dashed horizontal line and in the rightmost column of Table 6.3. From Figure 6.5, it is clear that the index of refraction increases with Li-salt concentration. This is a well-established consequence of solutions at elevated concentrations [83, 84]. Also, the presence of electrolyte additives also produces a shift in *n* to higher values.

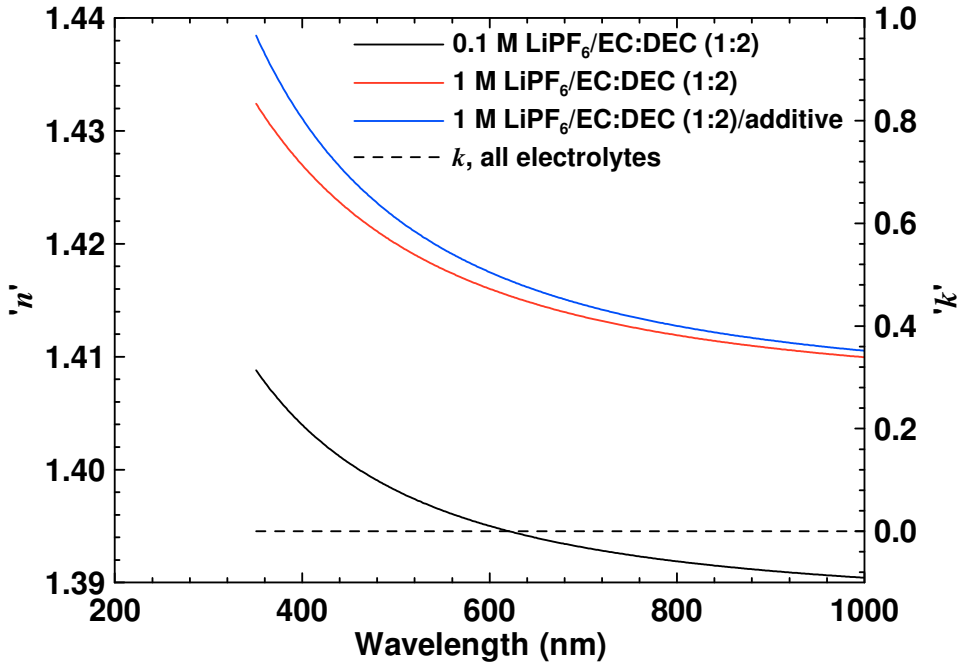

Figure 6.5 Optical constants for the electrolytes used with the in-situ electrochemical cell. (*n*, *k*) pairs were determined using a Cauchy dispersion relation. Additives are either 2% by weight VC or FEC.

In a study by Lei et al., SEI growth on $LiMn_2O_4$ thin film positive electrode materials was measured in-situ using ellipsometrically. A 1.0 M $LiPF_6$/EC:DMC (1:1) electrolyte was used and its refractive index and extinction coefficient were determined to be 1.401 and 0, respectively [85]. No formal explanation was given as to how these values were determined, nor to which wavelength they pertained. Lei et al. performed

Table 6.3 Cauchy parameters used to determine the real part of the refractive index for various electrolytes and the SEI used in all in-situ electrochemical testing. Note that *k* for all wavelengths is fixed at 0 in the Cauchy dispersion model.

	A	B (nm^2)	*k* (at all λ)
0.1 M $LiPF_6$/EC:DEC (1:2)	1.388	0.00258	0
1.0 M $LiPF_6$/EC:DEC (1:2)	1.406	0.0036	0
1.0 M $LiPF_6$/EC:DEC (1:2)/*additive	1.407	0.00392	0
Solid Electrolyte Interphase	1.422	0.0104	0

*additive = 2% VC or 2% FEC

measurements over the spectral range from 389-550 nm using a spectroscopic ellipsometer. The electrolyte used in this thesis has a refractive index which is only slightly above 1.401 at λ = 1000 nm using an EC:DEC (1:2) solvent rather than an EC:DMC (1:1) solvent. It is felt that the values of our own (*n*, *k*) pairs for electrolyte are more robust than those presented by Lei et al. as they are wavelength dependent over an appreciably large wavelength range (350-1000 nm).

In a study by Kong et al. [42], SEI growth was investigated on various carbon electrodes in-situ using SE. A Li/C in-situ cell was constructed using 1 M $LiPF_6$/EC:DMC (1:1) as electrolyte. Ellipsometric spectra were measured between 330-730 nm. The Li/C cells were simultaneously studied by cyclic voltammetry between 0 V and 3.5 V at sweep rates between 1-5 mV/s. Kong et al. used an optical model which incorporated the surface roughness of the carbon films. However, no fits to the ellipsometric parameters were given in the study, nor were there any indicators of the goodness-of-fit, such as MSE. From ellipsometric modeling, the index of refraction of the SEI was determined to be within the range of 1.41-1.52 with an extinction coefficient of roughly 0. Presumably, a Cauchy dispersion layer was used to determine the optical properties of the SEI as typically $k = 0$ in the model (no fitting details were given in the publication). In the study, the thickness of the SEI on a carbon film electrode was 60 nm after the first cycle and the thickness did not change appreciably in further cycles. Similarly, for a highly ordered pyrolytic graphite (HOPG) electrode, the SEI grew to 36 nm after the first two cycles. Again, no details about the ellipsometric analysis were given.

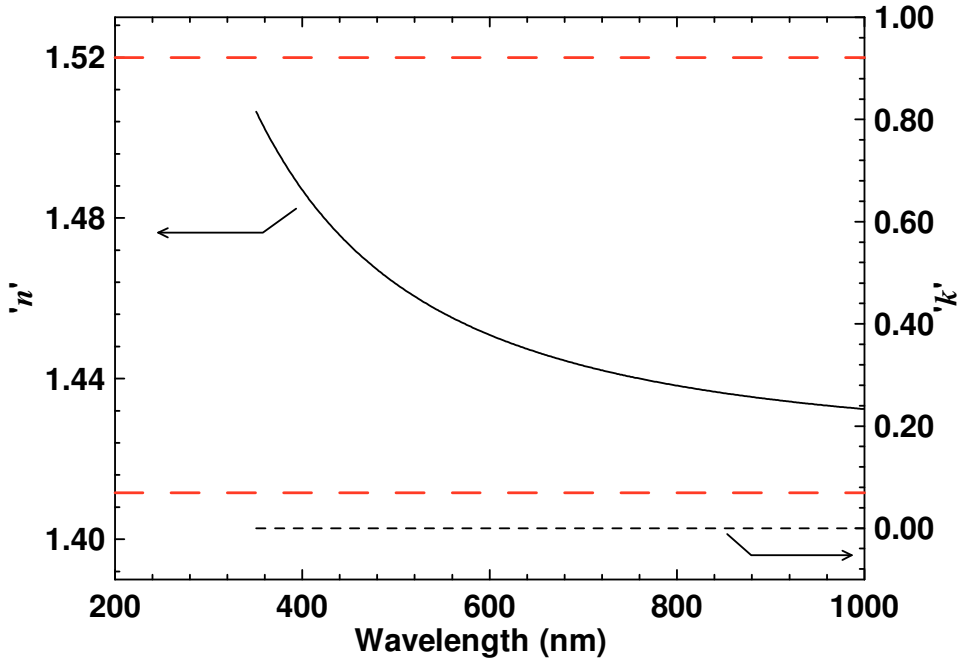

Figure 6.6 Optical constants for the SEI layer determined by potentiostatic chronoamperometry using a Li/TiN electrode. Red dashed lines indicate the range in which the refractive index falls for the SEI from Kong et al. [42].

Figure 6.6 shows the index of refraction and extinction coefficient of the SEI measured on a TiN electrode in a 1 M $LiPF_6$/EC:DEC (1:2) electrolyte. Dashed horizontal lines in Figure 6.6 represent the range of values for the index of refraction as determined by Kong et al. [42]. Table 6.3 summarizes the Cauchy dispersion parameters of the fit. The refractive index of the SEI varies from 1.43 to 1.51 over the wavelength range from 350-1000 nm. It is beneficial to use the (n, k) values of the SEI determined by Kong et al. [42] as a quick verification of our own values. As our own values fall in the range given by Kong et al., it is reasonable to assume our values are correct. Again, due to the methodical approach used to measure the refractive indices of the SEI, our values are believed to be more robust than those obtained in previous work [42].

6.2 In-situ Electrochemical Measurements

The materials used to construct the in-situ cell were selected such that they did not react with Li. Figure 6.7 shows the voltage-time curve of an in-situ cell in 0.1 M

$LiPF_6$/EC:DEC (1:2) cycled between 0.005 V and 1.2 V with a discharge/charge current of 80 μA. A glass plate of the same dimensions as a sputtered electrode was placed in the stainless steel electrode "well". In this "blank" cell, the electrode "well" acted as the working electrode. This "blank" cell was cycled against Li to determine the effects of the cell components on the observed capacities. The first discharge of the "blank" in-situ cell was very long. The lengthy discharge times can be explained by the reduction of electrolyte on the conductive stainless steel electrode "well", the stainless steel vacuum fittings, and reactions of Li with oxides. In the in-situ cell, upwards of 8 mL of electrolyte is used. In a similar coin-type cell, only 8 drops from a syringe (~32 μL) of electrolyte are used. In both the in-situ and coin cells,

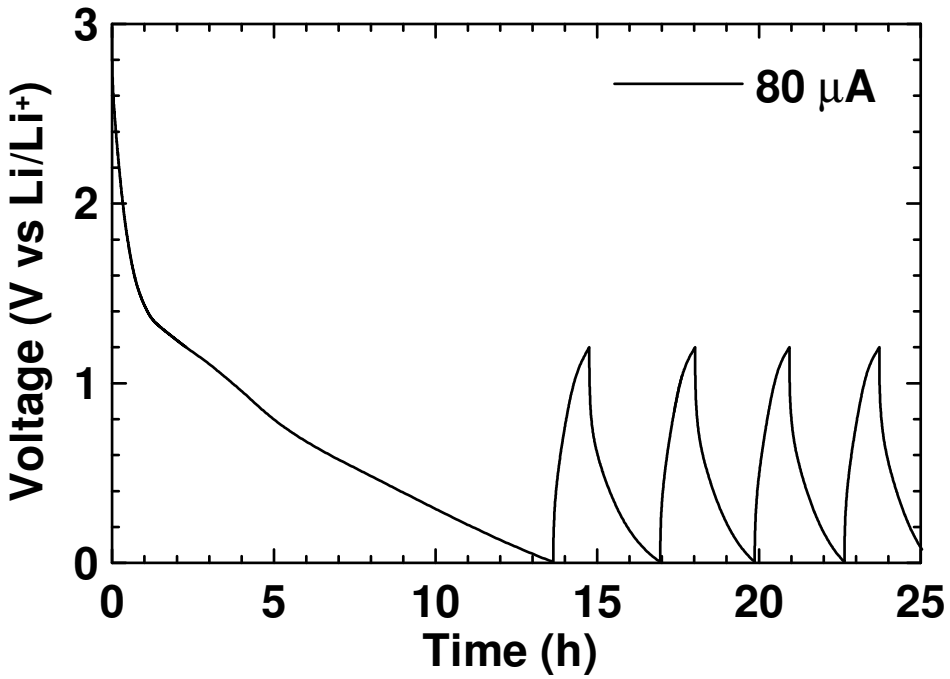

Figure 6.7 Voltage-time curve of an in-situ cell constructed with no active working electrode material. A glass plate was placed in the working electrode "well" for spacing purposes. The in-situ cell was cycled between 0.005 V and 1.2 V at a discharge/charge current of 80 μA (C rate). 0.1 M $LiPF_6$/EC:DEC (1:2) electrolyte was used.

there is a large excess of electrolyte. A passivating SEI layer should therefore be the same in both cases. However, due to the difference in electrolyte volume between the cells, the absolute amount of impurities (such as H_2O and HF) is different. These could lead to an excess current and an overly thick and different film in the in-situ cell which

yield long discharge times. During the charge cycles, the voltage of the cell increased very rapidly to the upper voltage limit (1.2 V). There was very little curvature in the charge, indicating that the cell components added only a very small contribution to the charge capacity. Similarly, during subsequent cell discharges, the voltage decreased rapidly to the lower voltage limit (0.005 V). It should be noted that the time taken to complete the second discharge was slightly longer than the second charge. Subsequent discharge cycles were on the same order as the charge cycles.

6.2.1 a-Si Thin Film Electrodes

Figure 6.8 shows the time dependence of Ψ, Δ, and cell voltage for 5 different wavelengths during cycling between 0.005 V and 1.2 V for two Li/a-Si in-situ cells (solid curves (cell identifier 101021) and dashed curves (cell identifier 101210)). The electrolyte used was 0.1 M $LiPF_6$/EC:DEC (1:2). For the cell labeled 101021, the discharge/charge current was chosen to provide a C/10 cycle rate (64 μA) until $t \approx 95$ h and was then reduced by half to C/20 (32 μA). For the cell labeled 101210, the discharge/charge current was chosen to provide a C/10 cycle rate (64 μA). The 5 wavelengths were equally spaced between 350-1000 nm. No data below 350 nm was analyzed as the electrolyte strongly adsorbed light in this region. There is excellent repeatability between runs both in terms of the voltage curve and the ellipsometric parameters. Large variations in Ψ and Δ follow the voltage curve of the Li/a-Si in-situ cell very closely.

After examination of the voltage-time curves of Figure 6.8, it is obvious that a C/10 discharge was not attained on the first discharge. The first discharge of both Li/a-Si in-situ cells was ~35 h. During the discharge of the in-situ cell, the a-Si electrode is lithiated. Simultaneously, however, the electrolyte is reduced, causing the formation of the passivating SEI layer. Electrolyte reduction causes delithiation of the lithiated electrode to occur. Therefore, the discharge of the in-situ cell was very long. Similarly, subsequent discharges were longer than the charge cycles due to the reduction of electrolyte species.

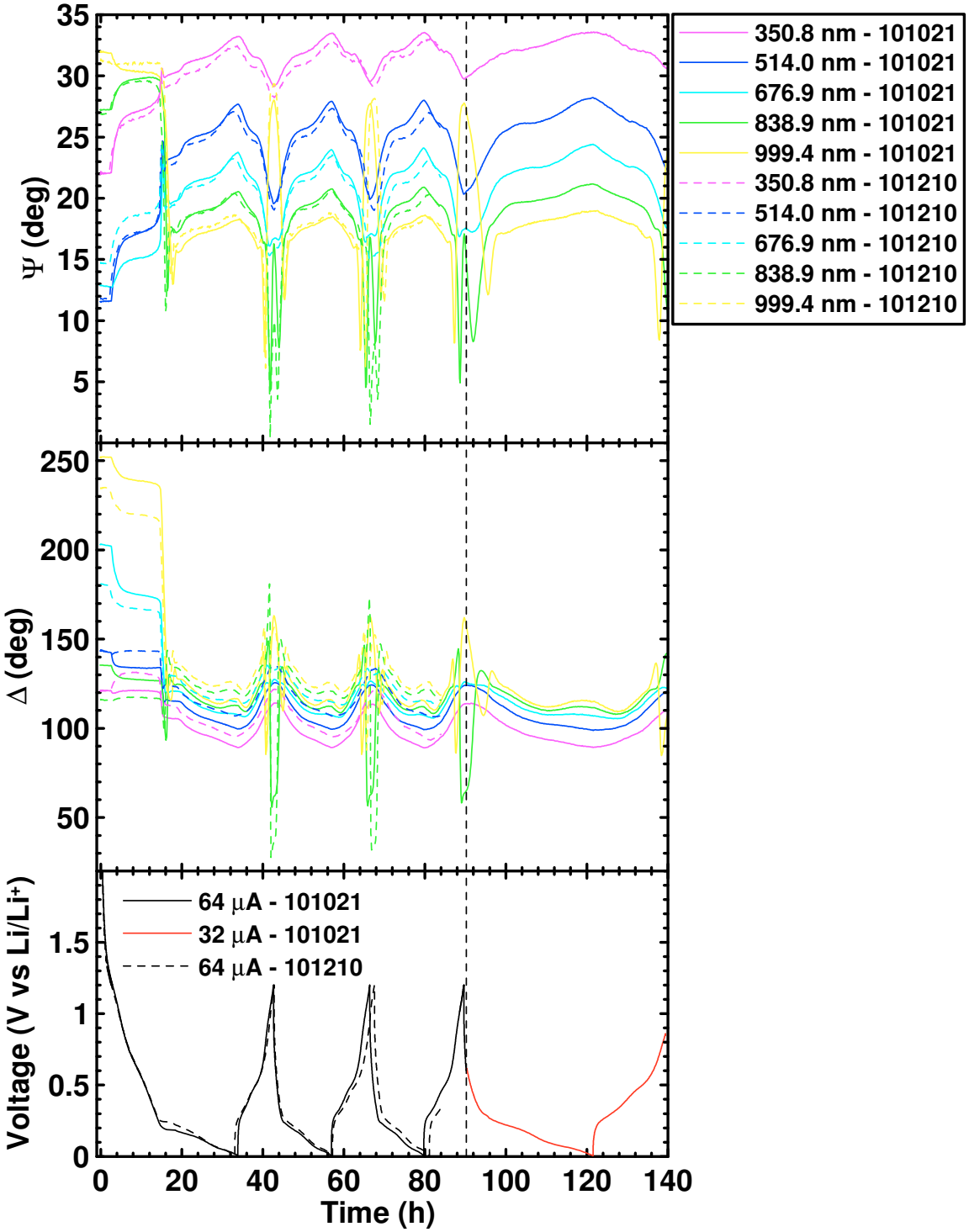

Figure 6.8 Time dependence of the ellipsometric parameters, Ψ and Δ, for 5 wavelengths during cycling of two Li/a-Si in-situ cells at constant current. Cells were cycled between 0.005 V and 1.2 V begins at a C/10 rate (64 µA). For cell 101021, the cycling switched to a C/20 rate (32 µA) at t = 95 h. The switch in current is indicated by a vertical dashed line. The cells were cycled in a 0.1 M $LiPF_6$/EC:DEC (1:2) electrolyte.

During the first discharge of the Li/a-Si in-situ cell, two very short, sloping plateaus were observed. These were located at roughly 0.2 V and 0.1 V. During the first charge, the voltage increased almost immediately to roughly 0.3 V and then sloped gently to about 0.6 V. After which, the voltage quickly increased towards the upper voltage limit (1.2 V). For the second (and all other discharges), the sharp plateau at 0.2 V was no longer observed. Instead, the voltage curve gently sloped down to about 0.1 V. At 0.1 V, there was a slight change in slope to the lower voltage limit (0.005 V). Subsequent charges were similar to the first charge.

In a study by Hatchard and Dahn [69], the reaction between Li and a-Si electrodes was studied in-situ using x-ray diffraction (XRD). In the study, special Li/a-Si in-situ XRD cells were prepared. These cells were cycled at a rate of C/48 and the cell voltage was measured while XRD patterns were simultaneously recorded. The in-situ XRD cell was cycled to an upper voltage limit of 1.2 V. During the first discharge, the lower voltage limit was set to 0 V. Subsequent discharge voltage limits were set to 0.1 V. The a-Si negative electrodes were prepared by magnetron sputtering in similar fashion to the a-Si electrodes prepared in this thesis. Therefore, it is expected that the cycling characteristics of the in-situ ellipsometry cell should be similar to the in-situ XRD cell. During the first discharge of the in-situ XRD cell of Hatchard and Dahn, broad, gently sloping plateaus were observed at roughly 0.2 V and 0.1 V. During the first charge of the in-situ XRD cell, the voltage rapidly increased to 0.4 V where a broad plateau was observed. After which, the voltage rapidly sloped to the upper voltage limit (1.2 V). Subsequent discharges only exhibited a gentle sloping towards the lower voltage limit (0.1 V). During subsequent charges, the cell voltage immediately increased to about 0.3 V and then rapidly increased to the upper voltage limit. As expected, the cycling characteristics of the in-situ XRD cell are very similar to those observed in the in-situ ellipsometry cell. This is useful as the analysis of the in-situ XRD study on the Li/a-Si cell can be applied to the ellipsometry cell.

For the Li/a-Si in-situ cell, the brief plateau at 0.2 V arises from the insertion of Li into the a-Si electrode. The electrode material increases in volume as Li is inserted and the resultant Li_xSi alloy remains amorphous (a-Li_xSi) [69]. At cell voltages below 0.03 V, a change in slope of the discharge voltage is observed in the in-situ XRD cell.

Hatchard and Dahn showed that the a-Li_xSi alloy electrode crystallizes in this region forming $Li_{15}Si_4$. From the in-situ ellipsometry cell, a change in slope is not observed. As shown by Hatchard and Dahn, the thickness of the a-Si electrode apparently dictates whether the lithiated electrode will crystallize [69].

The Li/a-Si electrochemical system is rather complicated. There are multiple variables which continuously change as described below. As a result, it is nearly impossible to properly model the electrode ellipsometrically. a-Si is an optically transparent medium above roughly 450 nm (where *k* is near 0). However, during lithiation, a metallic a-Li_xSi alloy is formed. Metals are typically reflective and opaque. Not only is the electrode changing its optical properties (from a transparent film to a reflective opaque film), insertion of Li into the a-Si produces a volume expansion of 280% [16, 86]. Moreover, during cell cycling, the electrolyte species decompose to form the SEI on the electrode surface. Thus, it is nearly impossible to determine a single "grand" optical model which incorporates all of these variables. However, one can still analyze the raw Ψ and Δ parameters as they vary during the cycling of the in-situ cell to obtain qualitative information.

The ellipsometric parameters Ψ and Δ changed depending on the state of charge of the Li/a-Si in-situ ellipsometry cell. Figure 6.9 shows the ellipsometric parameters at several time slices from the Li/a-Si in-situ cell shown in Figure 6.8 (cell identifier 101021). At t = 0 h, the Ψ spectra sloped gently until ~520 nm. At ~520 nm, a feature consisting of two local minima was observed, where the first local minimum was deeper than the second. At ~760 nm, the Ψ curve sloped gently upwards. For Δ, the curve gently sloped upward to ~560 nm. Above ~560 nm, a feature was observed where the Δ parameter abruptly changed directions (almost vertical). This is a consequence of the Δ parameter increasing past 360º. Instead of continuously increasing to higher values, Δ wraps around to negative values (due to the rotating compensator element). Above ~720 nm, Δ steadily sloped upward.

Figure 6.8 shows that the first changes in Ψ and Δ occurred at t = 4 h. In Figure 6.9, these changes correspond to a shift in Ψ to higher values and a shift in Δ to lower values. Also, the local minimum in Ψ shifted to higher wavelengths as the first local minimum became shallower than the second. In Δ, the feature also shifted to higher

wavelength. From the voltage curves, this change occurred after a transition from a rapid decrease in voltage to a gently sloping region. The ellipsometric parameters remained relatively constant until the cell reached roughly 0.2 V at t = 14 h. Here, a transition from transparent a-Si to reflective a-Li_xSi was observed during lithiation. In Figure 6.9, this corresponds to a shift of Ψ and Δ to higher and lower values, respectively. The features also shifted to higher wavelengths. For Ψ, the second local minimum was much deeper than the first local minimum. At t = 16 h, the Ψ and Δ curves increased and decreased further. The two local minima in Ψ have merged into a single local minimum and has shifted to higher wavelengths. Similarly, the feature in Δ has decreased in amplitude and has shifted to higher wavelengths still. This behaviour corresponds to a smoothing of the Ψ and Δ curves in Figure 6.8 between t = 14 h and t = 32 h during the formation of the a-Li_xSi alloy.

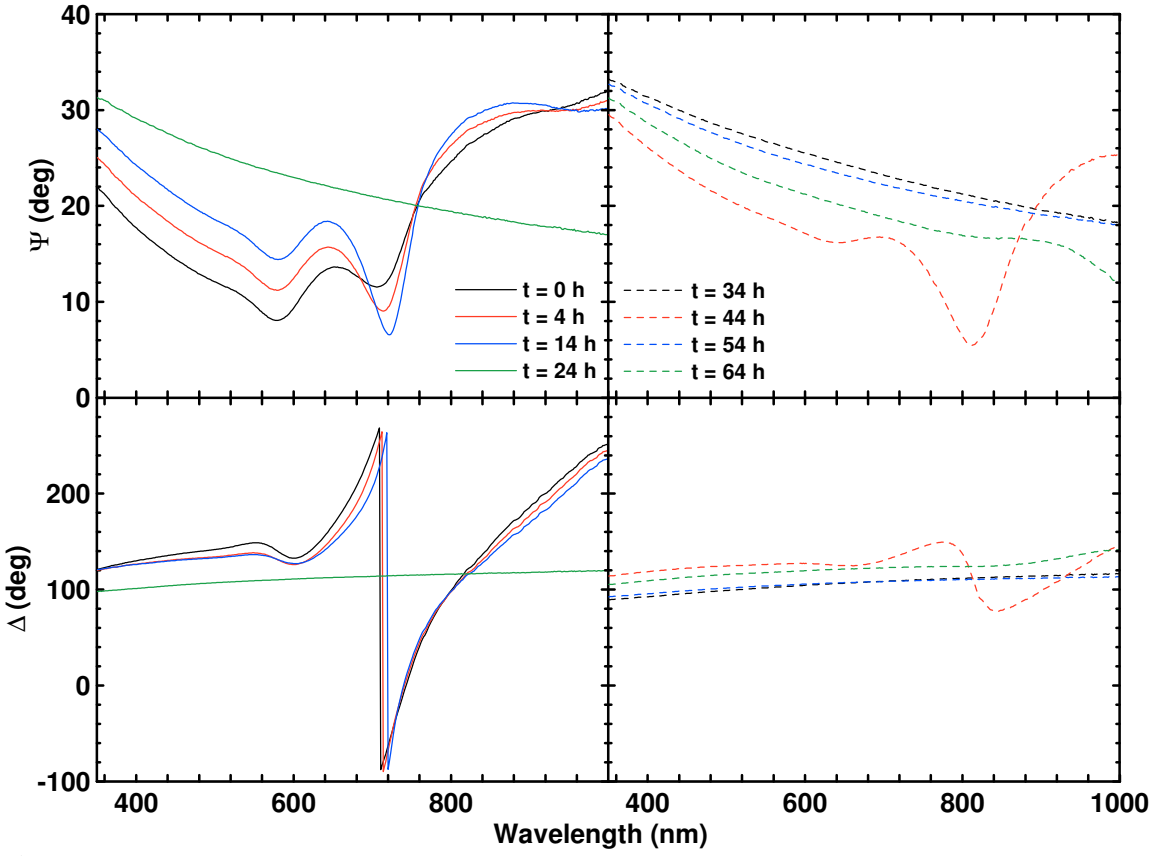

Figure 6.9 Time slices of the ellipsometric parameters during cycling of a Li/a-Si in-situ cell. A C/10 rate of charge was used. Electrolyte used was 0.1 M $LiPF_6$/EC:DEC (1:2). Data presented corresponds to in-situ cell 101021 in Figure 6.8.

At t = 18 h, the features in both Ψ and Δ have all but disappeared, reflecting the metal-like behaviour of the lithiated electrode. Figure 6.8 shows a gradual increase/decrease in Ψ/Δ until the lower voltage limit was reached between t = 14 h and t = 33 h. From previous in-situ experiments dealing with adsorbed protein layers on metallic thin films, it is known that an increase in Ψ and a decrease in Δ correspond to thickening or growth of a film [71]. The ellipsometric parameters suggest that the electrode remains reflective after the lower discharge limit is reached.

It is believed that the changes in Ψ and Δ correspond to the growth of a surface film (presumably the SEI). A reflective metal-like surface is formed during discharge. Measurements of metal thickness are difficult as the light beam cannot penetrate through the film to observe interferences in Ψ and Δ. The light can penetrate a thin transparent surface film, however, yielding a measurement of surface layer thickness. It is probable that the change in the ellipsometric parameters is due to SEI formation; however, there is another contribution from the formation of the a-Li_xSi alloy itself. Figure 6.10 shows predicted SE parameters from a simple calculation assuming a Ni substrate and an a-Li_xSi_{1-x} layer submerged in a 0.1 M $LiPF_6$/EC:DEC (1:2) ambient. The a-Li_xSi_{1-x} layer was modeled using an effective medium approximation (EMA). This approximation mixes the optical constants of two materials linearly. So, using the EMA layer, variable amounts of Li can be mixed into the a-Si layer. As x in a-Li_xSi_{1-x} increased to x = 0.1, both Ψ and Δ decreased across the spectrum and the amplitude of their features was reduced. Above x = 0.1, the Ψ and Δ curves lost their features (local minima, abrupt change of value, etc.) and became smooth over the wavelength range. Ψ increased to higher values over the spectrum as the Li content was increased. Similarly, Δ decreased slightly with Li content. It is probable that a thin transparent film formed on the electrode surface as the cell voltage was decreased. However, the changes in Ψ and Δ are also attributed to the change of the a-Li_xSi alloy as the Li content of the electrode increased.

During the charge, the electrode remained reflective until roughly 0.6 V at about t = 40 h. Between t = 33 h and t = 40 h, the reflective Ψ and Δ spectra sloped in the opposite directions (Ψ decreased and Δ increased). Figure 6.9 clearly shows the

decrease/increase in Ψ/Δ. This may be a thinning of a transparent layer on the electrode, a decrease in Li content of the alloy electrode, or a combination of both. Near 0.6 V, the

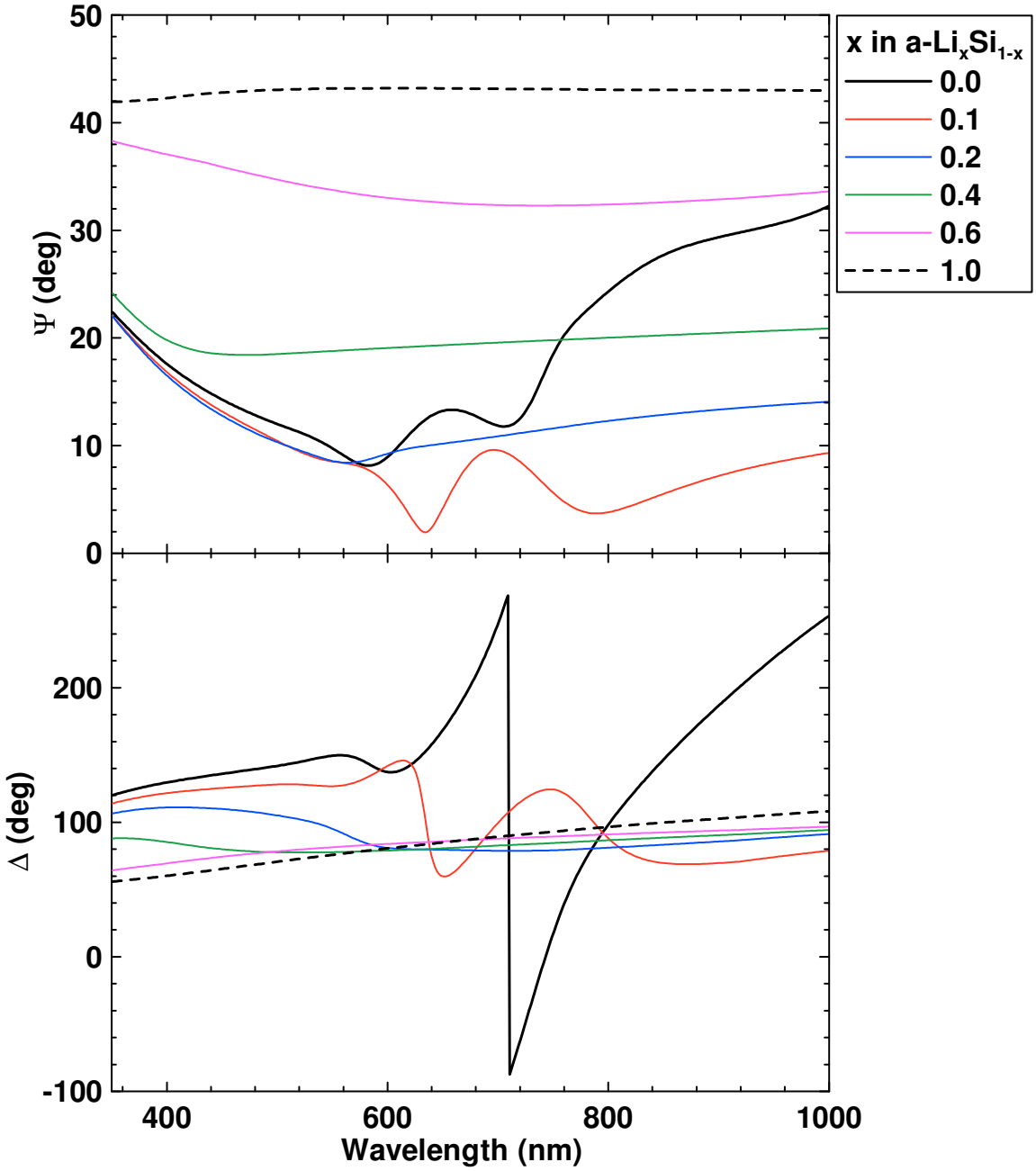

Figure 6.10 Predicted ellipsometric parameters of an a-Li_xSi_{1-x} alloy electrode in 0.1 M $LiPF_6$/EC:DEC (1:2) as x varies from 0.0 to 1.0. Data were generated using an optical model with a Ni substrate, an a-Si layer with variable Li content (using the effective medium approximation (EMA)), and the electrolyte ambient.

ellipsometric parameters suggest that the electrode became transparent once again and spectra which resembled the original values were recovered at the top of charge. This is reflected in Figure 6.9 by the blue dashed curve at t = 44 h. A single local minimum is seen in Ψ and the strong change in Δ is observed near 800 nm. These changes in the ellipsometric parameters continue during cycling and appear to be very reversible. At the change in current at t = 95 h (cell 101021), the same features in Ψ and Δ are observed. However, as the current was halved (C/20 discharge from C/10), these features repeated with a period that was twice as long. Again, this reflects the excellent reversibility in the ellipsometric parameters during cycling of the cell.

From the change in ellipsometric parameters with the state of charge of the Li/a-Si in-situ cell, several key processes were observed. As the cell cycled, the a-Si electrode underwent a very clear, reversible transition between a semiconductor to a metal as the electrode was delithiated and lithiated, respectively. Also, no cracking of the a-Si electrode was observed during delithiation. Were cracking to occur, the underlying Ni film would be observed ellipsometrically. It was not. This suggests that the electrode expanded and contracted uniformly in the vertical direction with good adhesion to the Ni layer. Good film adhesion is supported by visual inspection of the a-Si electrodes after disassembly of the cells. Visually, the electrodes had a "dull grey" colouration typical of sputtered Si instead of a silvery luster characteristic to sputtered Ni.

6.2.2 Ni Thin Film Electrodes

To reduce complications involved with determining the correct optical model, materials which do not react with Li were used. From Figure 2.5, it is clear that Ni does not form an alloy with Li at room temperature. It was thought that a Li/Ni in-situ cell could be used to determine the optical constants of a SEI layer from which a correct optical model could be "reverse engineered". Figure 6.11 shows the time dependence of the ellipsometric parameters during cycling of a Li/Ni in-situ cell between 0.005 V and 3.0 V in 0.1 M $LiPF_6$/EC:DEC (1:2) as well as the corresponding voltage curve. The discharge/charge current was set to 80 μA (C/5 rate).

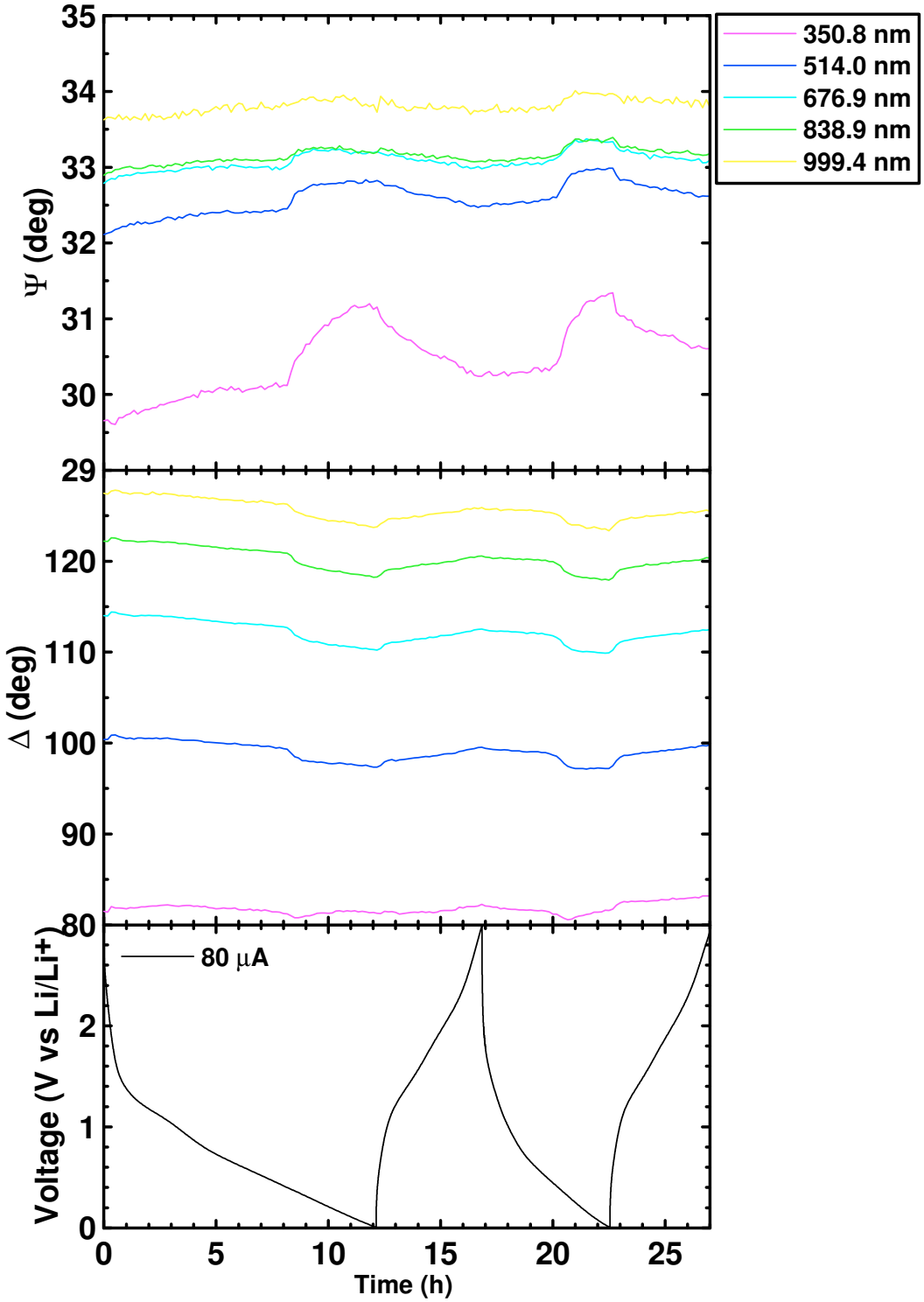

Figure 6.11 Time dependence of the ellipsometric parameters, Ψ and Δ, for 5 wavelengths during cycling of a Li/Ni in-situ cell between 0.005 V and 3.0 V. Discharge/charge current used was 80 μA (C/5 rate) in 0.1 M $LiPF_6$/EC:DEC (1:2) electrolyte.

As was observed in Figure 6.8, the first discharge of the Li/Ni in-situ cell was very slow relative to the charge cycles due to electrolyte reduction. During the first discharge, the voltage curve slopes gently to the lower voltage limit with no obvious plateaus. A slight change in slope was observed near 1 V during the discharge; however, there was only a slight change in the ellipsometric parameters. During discharge, Ψ and Δ increased and decreased smoothly until about 0.4 V. At this point, a small "step" was observed in which the parameters quickly changed and then gently sloped until the lower voltage limit was reached. During the charge cycle, the ellipsometric parameters quickly "stepped" back in the opposite direction.

Although Ni is inert to Li, its oxide, NiO is not. The presence of NiO is an unfortunate consequence of removing the Ni electrodes from the sputtering chamber. It was thought that the effect of NiO on the cycling of the cell was negligible. It will be shown that this may not be the case. When exposed to air, Ni readily forms a thin native layer of NiO. In a study by Wang and Qin, NiO thin film negative electrodes were prepared by pulsed laser ablation and cycled between 0.01 V and 3 V against Li-metal [87]. The electrolyte used was 1 M $LiPF_6$/EC:DMC (1:1) and the charge/discharge current was 10 $\mu A/cm^2$. NiO has a theoretical specific capacity of 700 mAh/g and reacts with Li by displacement following

$$NiO + 2Li \underset{\text{charge}}{\overset{\text{discharge}}{\rightleftharpoons}} Li_2O + Ni\,. \tag{6.1}$$

Figure 6.12 shows the voltage curve of the Li/NiO cell adapted from [87]. In the first discharge of the Li/NiO cell, a broad sloping plateau was observed at around 0.4 V. It was determined by Wang and Qin that this plateau corresponds to the formation of Li_2O, Ni, and SEI on the electrode surface.

Figure 6.13 shows the differential capacity of the Li/Ni in-situ cell for the first (black curve) and second (red curve) cycles. Plateaus in a voltage-time (voltage-capacity) curve appear as humps (or spikes) in a differential capacity plot due to an abrupt change in the derivative. Thus, plots of differential capacity are useful to magnify any plateaus in a voltage-time (voltage-capacity) curve. So, if there was a plateau in the voltage-time curve near 0.4 V in Figure 6.11, it would appear as a hump in the plot of

differential capacity. Figure 6.12 shows no clear evidence of a peak or hump at 0.4 V. However, the displacement reaction in Eq. (6.1) may still take place as there is only a thin

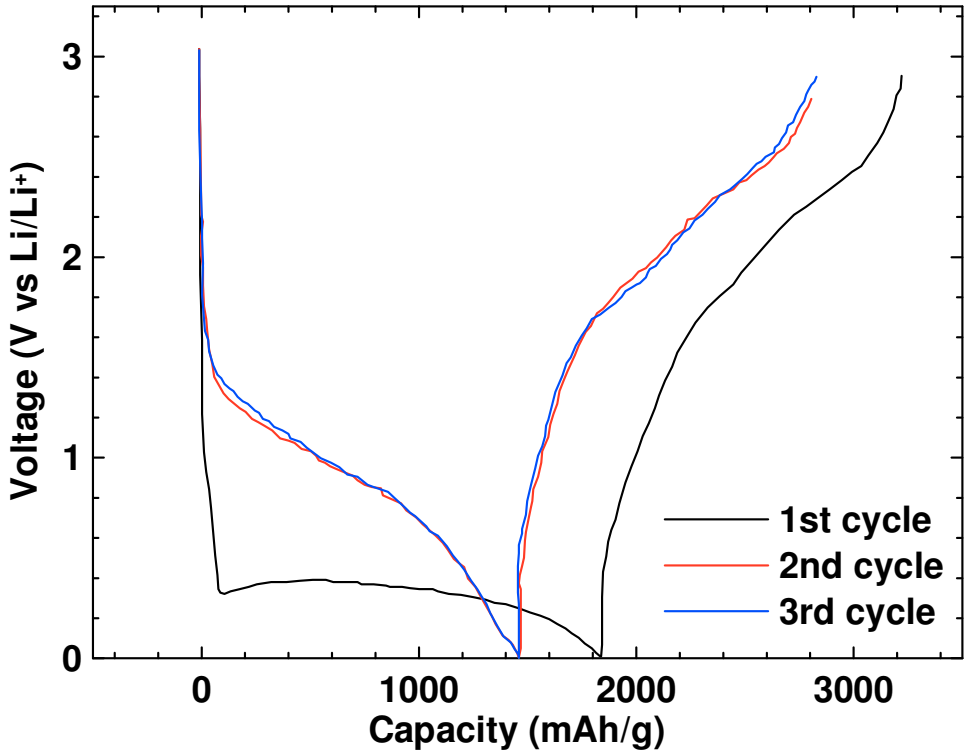

Figure 6.12 Voltage curve of the first 3 cycles of a Li/NiO cell. The cell was cycled between 0.01 V and 3 V in 1 M $LiPF_6$/EC:DMC (1:1) at 10 $\mu A/cm^2$. (Adapted from [87]).

native oxide on the electrode surface. It is clear from Figure 6.11 that there is some change in the electrode surface from the ellipsometric parameters at 0.4 V. This change is possibly due to a displacement reaction.

Figure 6.14 shows the thickness of the surface layer and the MSE of the fit of the optical model determined from ellipsometry measurements with respect to time during cycling. The optical model used to determine the thickness of the surface layer cannot distinguish between SEI species and reaction products in Eq. (6.1). As such, the term "surface layer" has been used to include Li_2O, Ni, and the SEI. To correctly model both components of the surface layer, an additional model is required which contrasts the optical properties of both media. However, this analysis is very difficult in the current setup. The optical constants of a known Li_2O layer must be measured separately from SEI species. As these are intimately coupled during the cycling of the Li/Ni in-situ cell,

such a model is impossible. Still, MSEs of no more than 16 were observed for the match of surface layer thickness. During discharge, the thickness of a surface layer increased linearly with a constant slope until roughly t = 8.5 h and 0.4 V. After this time, the

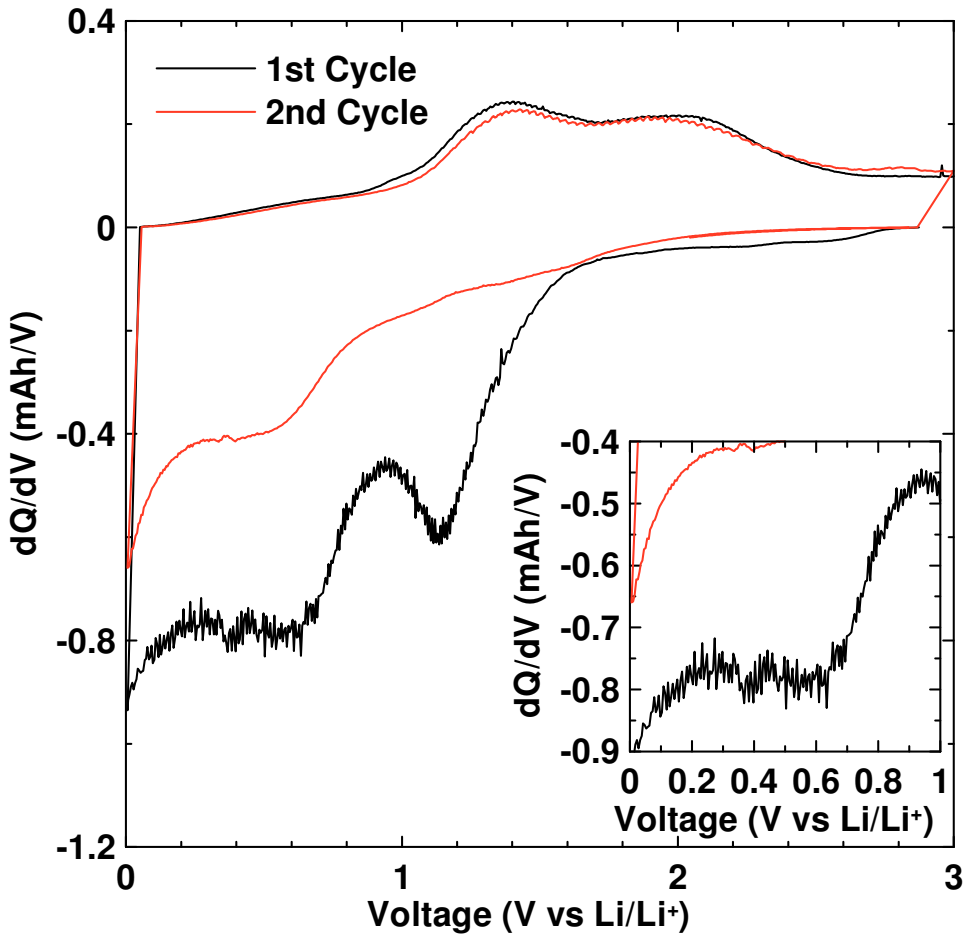

Figure 6.13 Differential capacity curve for 2 cycles of a Li/Ni in-situ cell cycled between 0.005 V and 3.0 V at a C/5 rate. The electrolyte used was 0.1 M $LiPF_6$/EC:DEC (1:2). The inset shows a zoomed-in view of the differential capacity below 1 V.

surface layer thickness increased rapidly to its maximum of ~17 nm at the bottom of the first discharge at t = 12 h. At the start of the first charge, the surface layer thickness decreased rapidly to ~13 nm at t = 13 h and ~1.2 V. After this time, the layer thickness sloped down smoothly to its minimum value of ~5 nm at the bottom of the first charge at t = 17 h and 3 V. Note that the surface layer did not return to the baseline at this potential and remained on the Ni electrode surface. During the second discharge, again, a gradual increase in the surface layer thickness was observed until ~0.4 V at t = 20 h. Above this

time, the surface layer thickness increased rapidly to its maximum value of ~19 nm at the bottom of the second discharge at t = 22.5 h. The process continued during subsequent discharge/charge cycles.

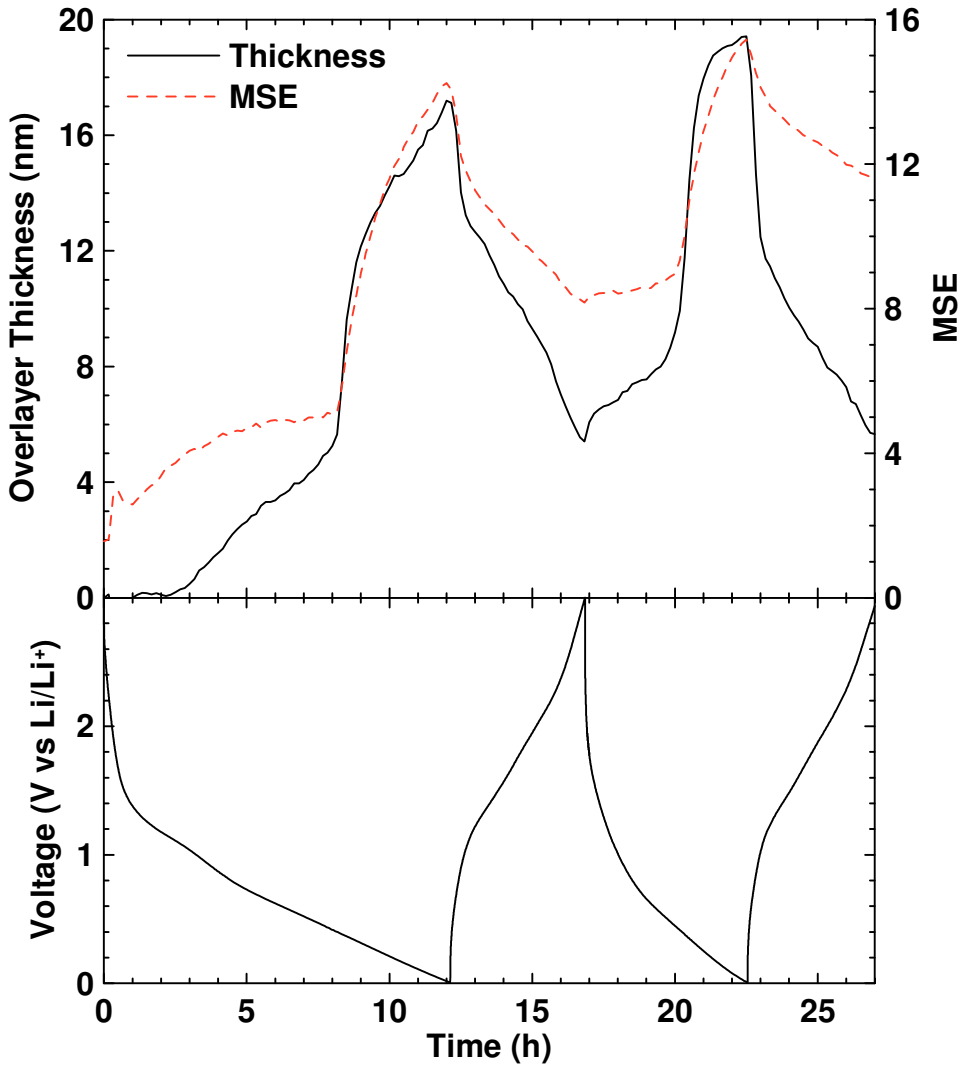

Figure 6.14 Time dependence of the surface film thickness, MSE to the fit of the optical model to the ellipsometric data, and corresponding voltage curve of a Li/Ni in-situ cell cycled at C/5 (80 μA). Electrolyte used was 0.1 M $LiPF_6$/EC:DEC (1:2).

Recall that the displacement reaction between Li and NiO occurs near 0.4 V [87]. In Figure 6.14, a rapid increase in the surface layer thickness was observed at and below 0.4 V. The rapid increase in layer thickness can be attributed to a combination of both the SEI and Li_2O formation on the Ni electrode surface. At the beginning of the first

charge of the cell, about 4 nm of the surface film was immediately stripped away. One can conclude that even at a relatively high potential of 3 V, the SEI and Li_2O cannot be stripped completely from the electrode surface. Even when the potential was increased to 4 V, a surface film remained on the Ni electrode (data not shown). Thus, one can conclude that surface film formation is irreversible to some degree at typical Li-battery operation potentials. During the second discharge, the surface layer again gradually increased until ~0.4 V. Once this potential was reached, the displacement reaction occurred forming a very thick film on the Ni electrode. The stripping of the surface layer during charge is attributed to a removal of the SEI (destabilization) and the backwards reaction of Eq. (6.1). The destabilization and thinning of the SEI is similar to the destabilization of the SEI on mesocarbon microbead (MCMB) electrodes as observed by Zheng et al. [88].

6.2.3 TiN Thin Film Electrodes

Figures 6.15-6.17 show typical results of the time dependence of the ellipsometric parameters for 3 wavelengths (350.8 nm, 514.0 nm, and 676.9 nm) and current during potential hold experiments for Li/TiN in-situ cells. The electrolytes used were 1 M $LiPF_6$/EC:DEC (control), 1 M $LiPF_6$/EC:DEC/2 wt.% VC, and 1 M $LiPF_6$/EC:DEC/2 wt.% FEC (in Figures 6.15-6.17, respectively) and the potential "steps" were, in order, 1.0 V, 0.5 V, 0.1 V, 1.0 V, 2.0 V, and 3.0 V. Each hold in potential lasted for 10 h. For holds going from a more positive potential to a less positive potential (3.1 V to 1.0 V, for example), a negative current was registered. The reverse was also observed. This behaviour is similar to a discharge/charge cycle where during a discharge (going from a high voltage to a lower voltage) a negative current is required. Similarly, a positive current is required to go from a low potential to a higher potential. The sign of the currents was reflected in the integrated area under the curves to obtain the total charge of the in-situ cell during the potential holds. In Figures 6.15-6.17, some noise due to limit switching of the source-measure unit is observed.

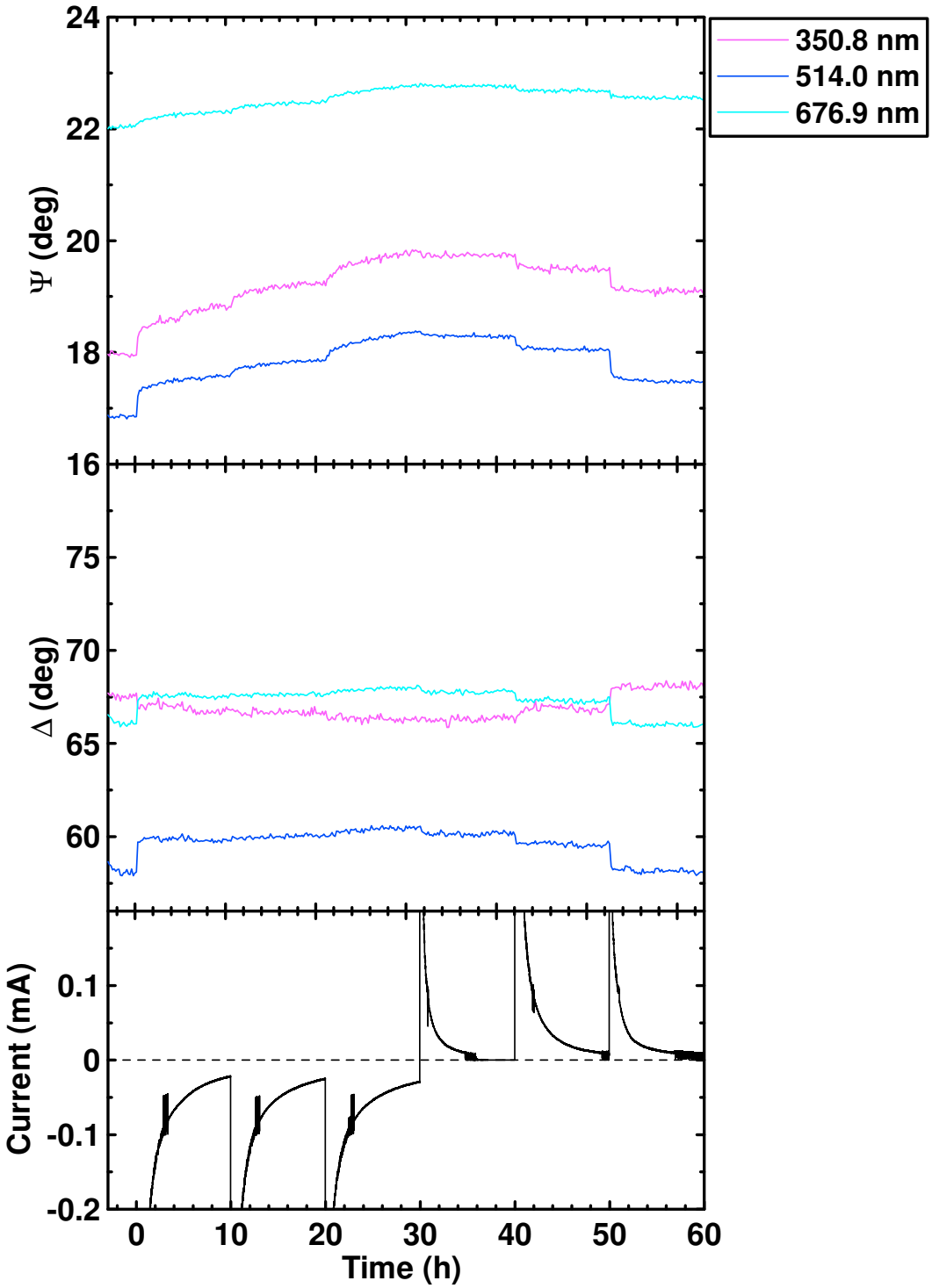

Figure 6.15 Time dependence of the ellipsometric parameters, Ψ and Δ, for 3 wavelengths during a potential hold study of a Li/TiN in-situ cell using 1 M $LiPF_6$/EC:DEC electrolyte. In the bottom panel, the cell current is shown. Potential "steps" were, in order, 1.0 V, 0.5 V, 0.1 V, 1.0 V, 2.0 V, and 3.0 V. The beginning of the transition to another potential "step" is shown as a steep change in slope.

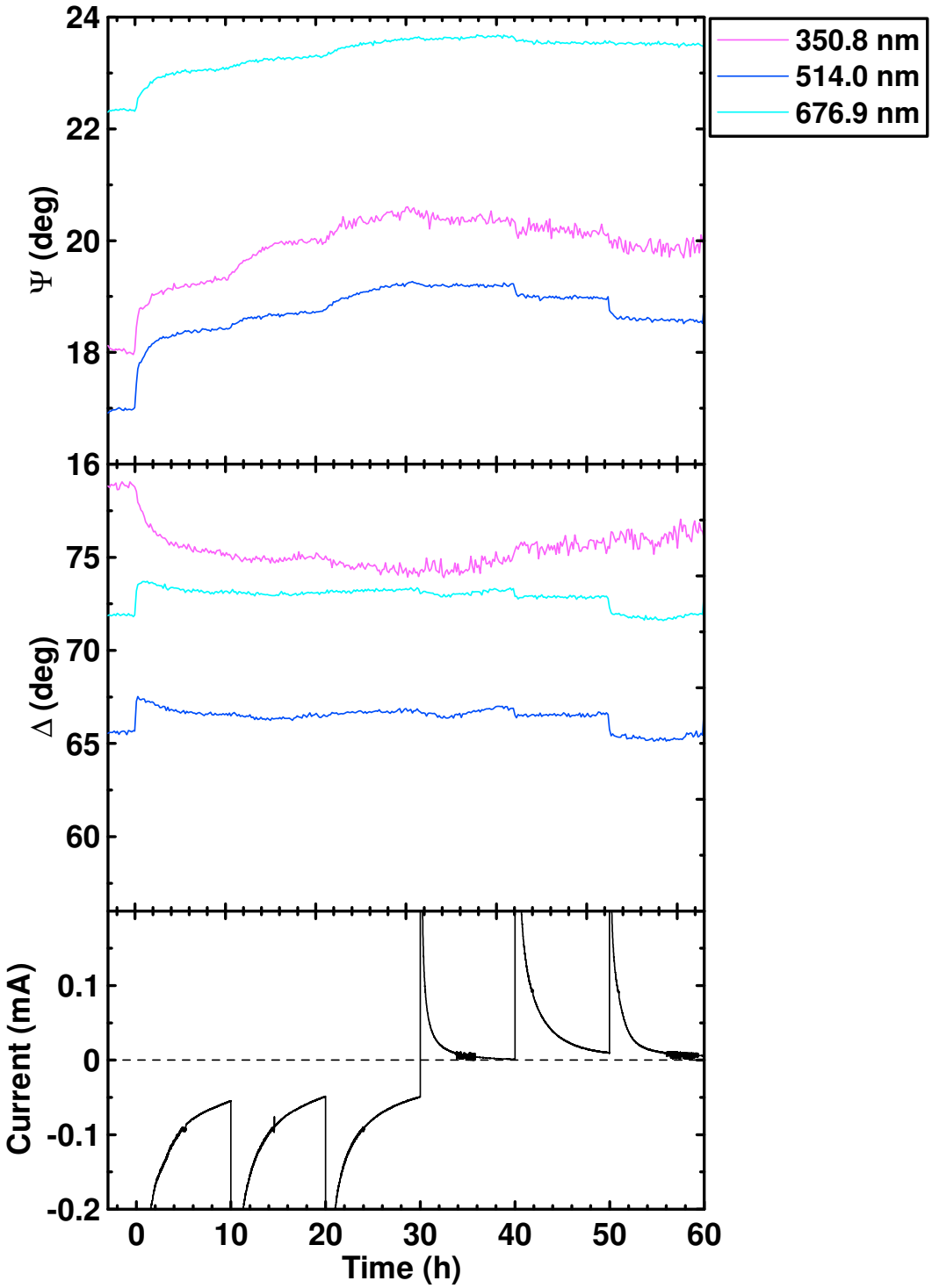

Figure 6.16 Time dependence of the ellipsometric parameters, Ψ and Δ, for 3 wavelengths during a potential hold study of a Li/TiN in-situ cell using 1 M $LiPF_6$/EC:DEC/2 wt.% VC electrolyte. In the bottom panel, the cell current is shown. Potential "steps" were, in order, 1.0 V, 0.5 V, 0.1 V, 1.0 V, 2.0 V, and 3.0 V. The beginning of the transition to another potential "step" is shown as a steep change in slope.

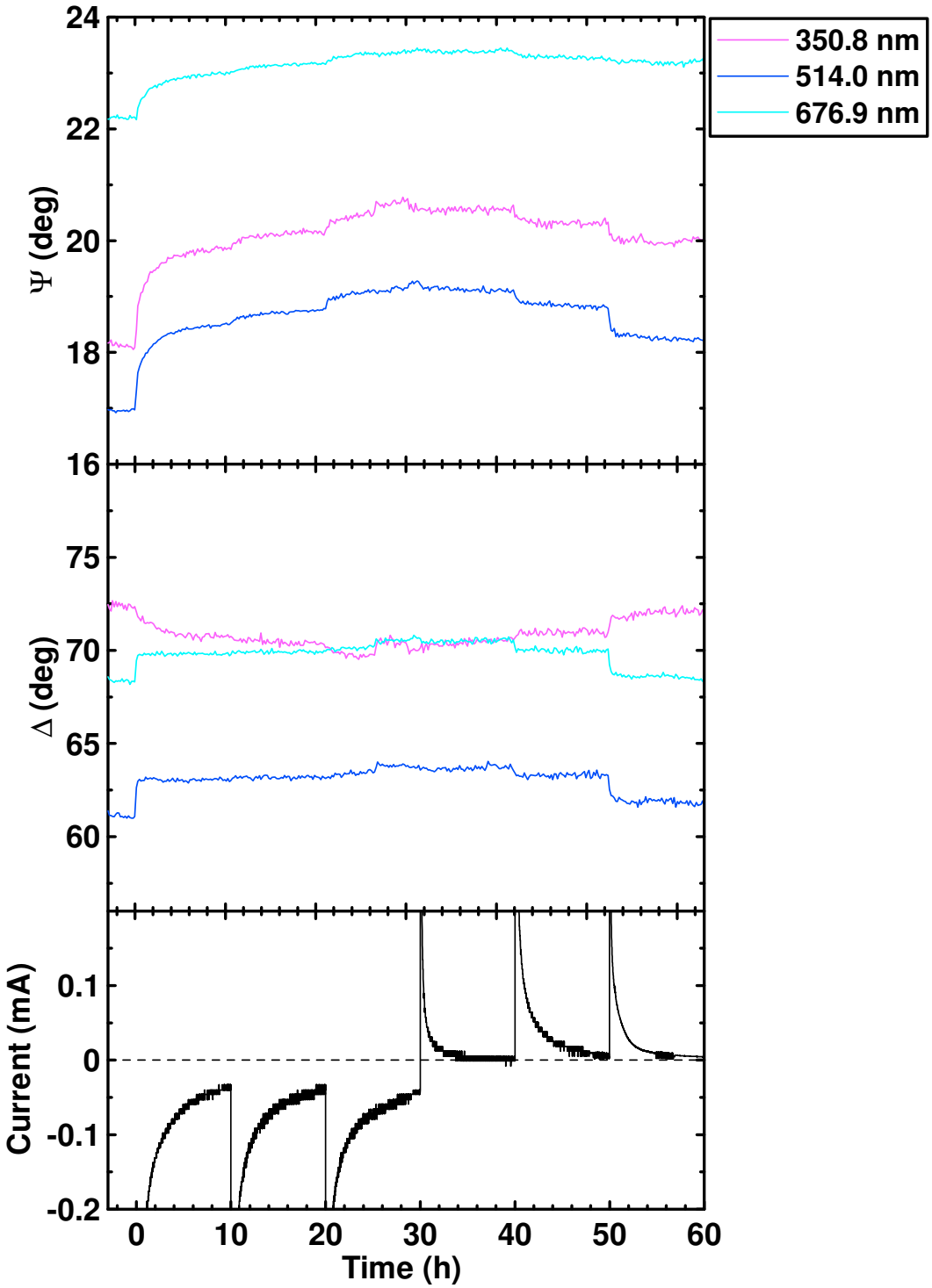

Figure 6.17 Time dependence of the ellipsometric parameters, Ψ and Δ, for 3 wavelengths during a potential hold study of a Li/TiN in-situ cell using 1 M $LiPF_6$/EC:DEC/2 wt.% FEC electrolyte. In the bottom panel, the cell current is shown. Potential "steps" were, in order, 1.0 V, 0.5 V, 0.1 V, 1.0 V, 2.0 V, and 3.0 V. The beginning of the transition to another potential "step" is shown as a steep change in slope.

Figure 6.15 shows the time dependence of the ellipsometric parameters and current during a potentiostatic chronoamerometry measurement. The electrolyte used was 1 M $LiPF_6$/EC:DEC. Ψ for all 3 wavelengths increased smoothly in prominent steps as the potential was decreased. The change in Δ, however, is only very slight up until the potential holds went from a low voltage to a high voltage near t = 30 h. Each step in potential produced an asymptote in current towards 0 mA.

Figure 6.16 shows the time dependence of the ellipsometric parameters and current during a potentiostatic chronoamperometry measurement. The electrolyte used was 1 M $LiPF_6$/EC:DEC/2 wt.% VC. The values of both Ψ and Δ for the 3 wavelengths displayed were on average higher than those in Figure 6.15. The step-like changes in both parameters were also more pronounced with the presence of 2 wt.% VC. The measured currents during the first 1.0 V, 0.5 V, and 0.1 V potential holds did not asymptote as close to 0 mA over the same time period as the control cell. However, the observed currents for the 1.0 V, 2.0 V, and 3.0 V potential holds were similar to those of the control cell.

Figure 6.17 shows the time dependence of the ellipsometric parameters and current during a potentiostatic chronoamperometry measurement. The electrolyte used was 1 M $LiPF_6$/EC:DEC/2 wt.% FEC. The Ψ and Δ values were all greater than the control for the 3 wavelengths. The abrupt changes in the ellipsometric parameters due to the transition to a new potential were also more prominent with the presence of the FEC additive. In terms of current, there was very little difference between the cell with FEC and the control. It should be noted that the currents displayed in Figure 6.17 are discretized. This is a consequence of a minor malfunction of the auto-ranging function of the source-measure unit. The malfunction was corrected for all other experiments.

To determine the optical constants of the SEI, a measurement was performed on a Li/TiN in-situ cell using 1 M $LiPF_6$/EC:DEC with a modified potential hold protocol (see Section 5.4.2). Figure 6.18 shows the ellipsometric parameters for 2 wavelengths (514.0 nm and 676.9 nm) and the current during this study. The potential was held for only 2.5 h for 1.0 V, 0.5 V, 1.0 V, 2.0 V, and 3.0 V and roughly 48 h at 0.1 V. Consistent with Figures 6.15-6.17, prominent steps in Ψ and Δ were observed for each change in potential. Over the 0.1 V hold, Ψ increased smoothly for both wavelengths. In the same

region, Δ was relatively constant until t = 28 h and then increased smoothly. During the 2.5 h potential holds, the current asymptoted towards 0 mA, but broke away abruptly during the transition to the next step. Because of the short duration, the currents only approached ~-0.1 mA, -0.15 mA, 0.5 mA, and 0.1 mA for the 1.0 V, 0.5 V, 1.0 V, and 2.0 V holds, respectively. The vertical dashed lines in Figure 6.18 indicate the time slices used to analyze the ellipsometric parameters for the TiN film (green dashed line) and the SEI film (red dashed line). Figure 6.19 shows the fit results of the t = 53 h time slice (red dashed line) used to determine the optical constants of the SEI. For this time slice, an SEI thickness of 27.0 ± 0.8 nm was determined from optical modeling of Ψ and Δ. The fit shown in Figure 6.19 had a MSE of 16.4. Although the MSE is relatively large, the fit still provided values for SEI optical constants similar to other studies [42] and should be adequate for further data analyses. As will be shown, the MSE obtained for the fit of the SEI optical constants is comparable to other fits to ellipsometric data.

Figures 6.20(a)-6.20(c) show the thickness of the SEI layer formed on various TiN electrodes in Li/TiN in-situ cells plotted against time. Colours are used to distinguish between repeat trials. Table 6.4 summarizes the cell identifier and the electrolyte additive used (if any). Clearly, there were two different processes occurring which depended on whether the cell was in a discharge- or charge-like state (going from a high to low or low to high potential). There were two distinct regions of SEI growth for each hold in potential in each in-situ cell prior to the switch in direction of current at t = 30 h. At the beginning of each hold, there was a rapid film growth characterized by a steep slope. After which, the slope decreased in steepness. These changes in thickness most likely arose from rapid reduction of electrolyte species to initially form the SEI. After the surface of the electrode had been completely passivated, the reaction slowed. At lower potentials, the electrolyte species further reduced to form a thicker SEI film. Subsequent regions of rapid SEI thickening occurred for a shorter duration than during the first potential hold as the SEI had already formed and was being "topped up". On the "charge", the thickness of the SEI decreased almost instantaneously with the change in potential (at least within the 10 min data acquisition rate of the ellipsometer). After which, the film thickness stayed relatively constant for the duration of the 10 h hold. At the elevated potentials, a portion of the SEI was stripped from the surface. The initial

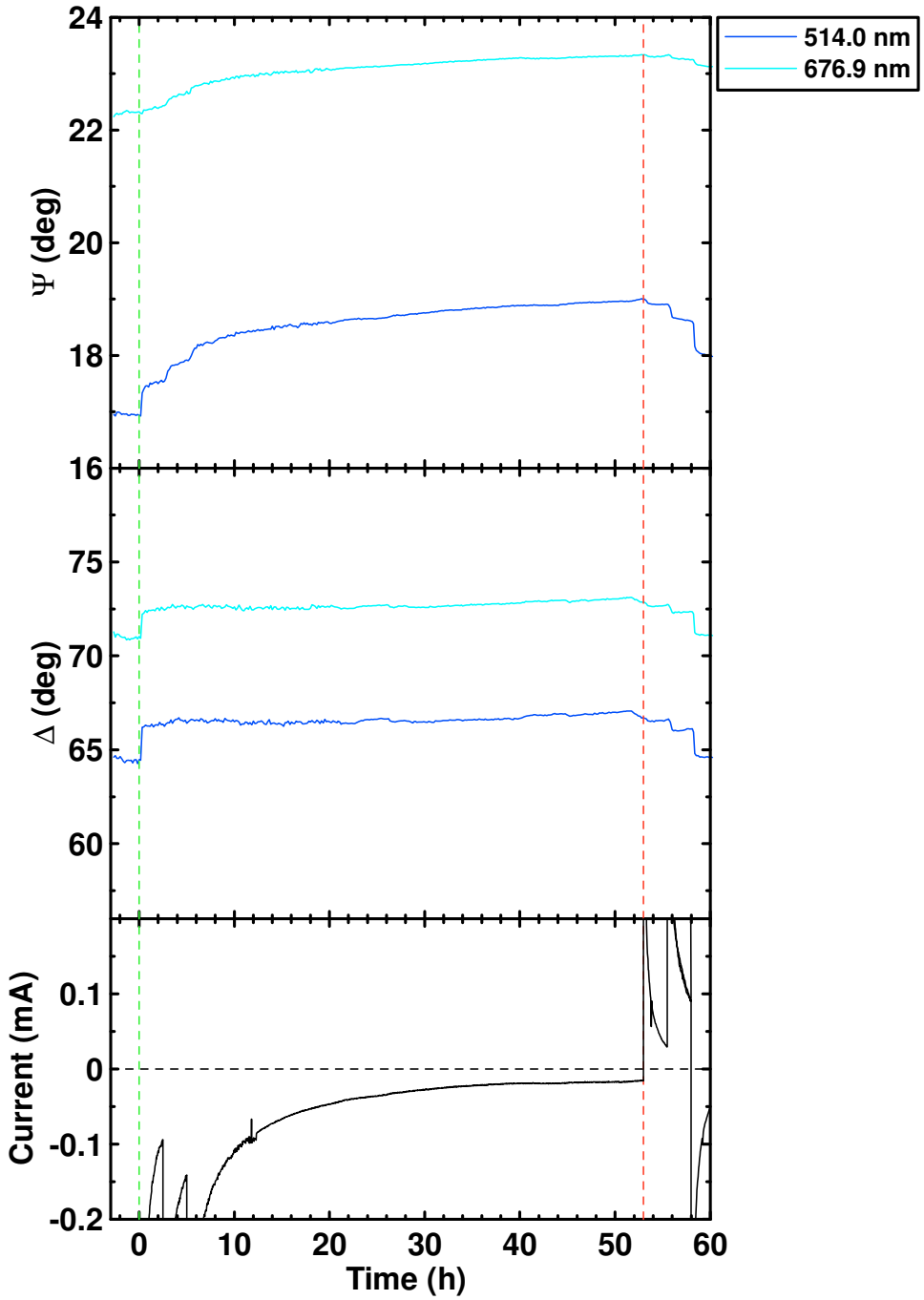

Figure 6.18 Time dependence of the ellipsometric parameters, Ψ and Δ, for 2 wavelengths during a potential hold study of a Li/TiN in-situ cell using 1 M $LiPF_6$/EC:DEC electrolyte. In the bottom panel, the cell current is shown. These data were used to determine the optical constants of the SEI. A modified potential hold protocol with a ~48 h hold at 0.1 V was used. Potential hold "steps" were, in order, 1.0 V, 0.5 V, 0.1 V, 1.0 V, 2.0 V, and 3.0 V. The the transition to another potential "step" is shown as a steep change in slope. Vertical dashed lines indicate the time slice used to obtain: the optical constants of the TiN film (green line) and the optical constants of the SEI film (red line).

stripping only affected the first few nanometers of the surface film. No further stripping of the SEI was observed until the next step in potential.

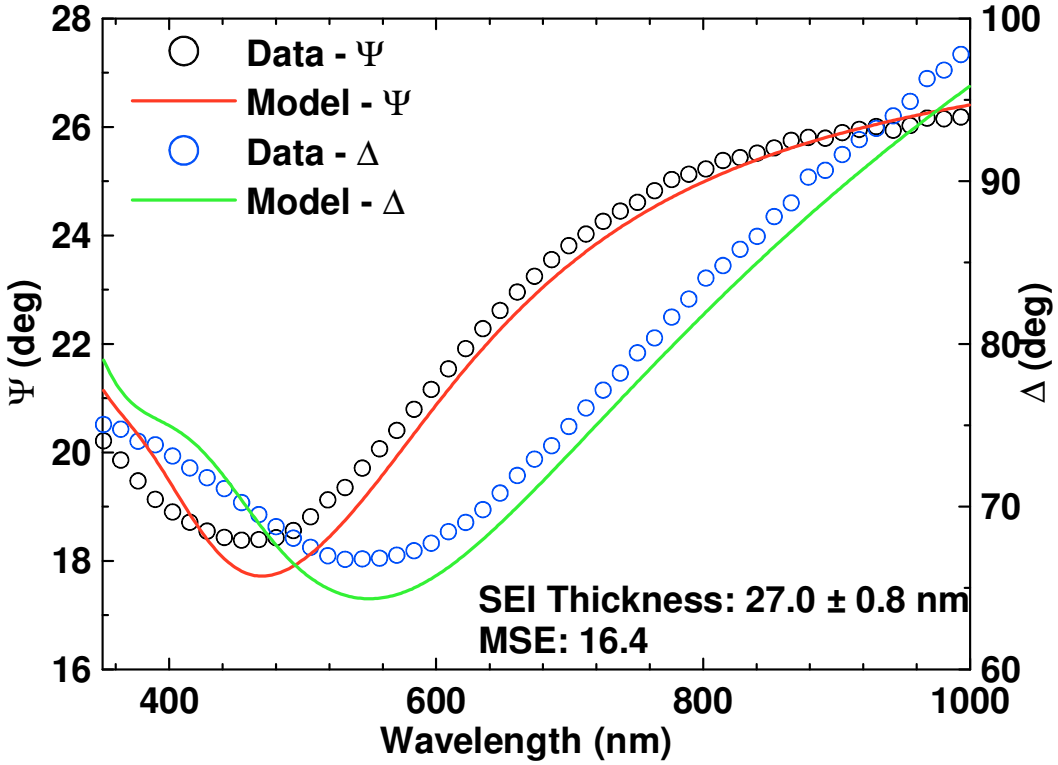

Figure 6.19 Fit of the ellipsometric data from t = 53 hrs of the potential hold study to determine the optical constants of the SEI (Figure 6.18). A Li/TiN in-situ cell with 1 M $LiPF_6$/EC:DEC was used to determine the optical constants of the SEI. The resultant SEI thickness at this time slice is 27.0 ± 0.8 nm and the fit had an MSE of 16.4.

Figure 6.20(a) shows that the thickness of the SEI peaked at ~9 nm, 13 nm, 20 nm, 19 nm, 16 nm, and 11 nm for the potential holds of 1.0 V, 0.5 V, 0.1 V, 1.0 V, 2.0 V, and 3.0 V, respectively. Figures 6.20(b) and 6.20(c) show that the SEI thicknesses peaked at ~17 nm, 23.5 nm, 30 nm, 29.5 nm, 27 nm, and 24 nm and 21 nm, 25 nm, 31 nm, 29 nm, 26 nm, and 20.5 nm for the various potential steps. Clearly, the SEI formed with the presence of additives was thicker than without.

Figures 6.20(d)-6.20(f) show the MSE of the fit of the ellipsometric data to the given optical model. The colours of the curves in Figures 6.20(d)-6.20(f) correspond to the thicknesses in Figures 6.20(a)-6.20(c). The MSE is the indicator of the goodness of fit. In general, the MSEs were all less than 25 except for one of the trials with VC.

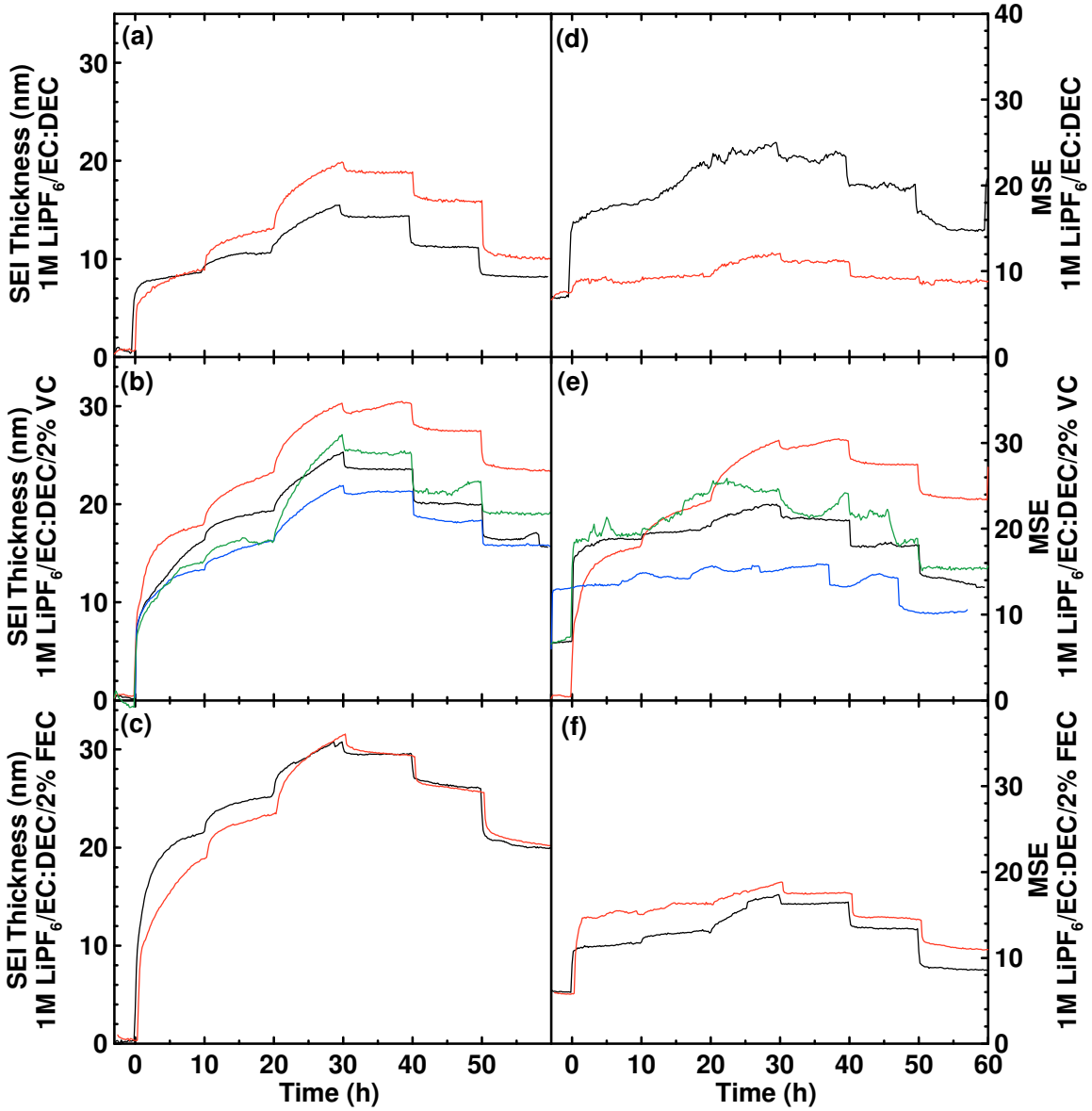

Figure 6.20 SEI thicknesses and MSEs determined ellipsometrically on TiN electrodes in Li/TiN in-situ cells using potentiostatic chronoamerometry. The electrolytes used were 1 M $LiPF_6$/EC:DEC (1:2) (a), 1 M $LiPF_6$/EC:DEC (1:2)/2% VC (b), and 1 M $LiPF_6$/EC:DEC (1:2)/2% FEC (c). The MSEs of the match between model and ellipsometric data are shown for the electrolytes 1 M $LiPF_6$/EC:DEC (1:2) (d), 1 M $LiPF_6$/EC:DEC(1:2)/2% VC (e), and 1 M $LiPF_6$/EC:DEC (1:2)/2% FEC (f). In order, the potential holds were 1.0 V, 0.5 V, 0.1 V, 1.0 V, 2.0 V, and 3.0 V (indicated by prominent steps).

These MSE values are permissible for these in-situ studies [89]. Typically, an in-situ system is much more difficult to model than an equivalent ex-situ system. For these in-situ measurements, a liquid ambient was used (the electrolyte). The mobile phase may react with the electrode changing it over time (hence the 3 h equilibrium step). Moreover, the light beam may interact with the mobile liquid differently than with the ambient air during an ex-situ measurement. As a result, matching the ellipsometric data to an optical model is more challenging. This is reflected by larger MSE values (>10). Unfortunately, there are no stringent criteria for a "good" MSE for these in-situ systems. Even worse, other in-situ SE studies on the SEI (such as Refs. [41-43, 85]) do not publish their MSEs for comparison. Thus, the only definition of a "good" optical model one can follow is: one that minimizes the MSE with as few variables as possible [89]. It is believed that the thickness results obtained from the optical models in this thesis are physical and match the working definition of a "good" model.

Table 6.4 Descriptions of the Li/TiN cells displayed in Figure 6.20.

Cell Identifier	Electrolyte	Figure 6.19 Curve Colour
110407	1 M $LiPF_6$/EC:DEC (1:2)	black
110308	1 M $LiPF_6$/EC:DEC (1:2)	red
110530	1 M $LiPF_6$/EC:DEC (1:2)/2% VC	black
110422	1 M $LiPF_6$/EC:DEC (1:2)/2% VC	red
110325	1 M $LiPF_6$/EC:DEC (1:2)/2% VC	blue
110315	1 M $LiPF_6$/EC:DEC (1:2)/2% VC	green
110508	1 M $LiPF_6$/EC:DEC (1:2)/2% FEC	black
110427	1 M $LiPF_6$/EC:DEC (1:2)/2% FEC	red

In a recent study by Nakai et al., the effect of FEC on the growth of SEI on Si negative electrodes was studied. In the study, 2 μm Si thin film electrodes were prepared by electron beam evaporation and Li/Si coin-type cells were constructed. There were two electrolytes used in the study: 1 M $LiPF_6$/EC:DEC (1:1) and 1 M $LiPF_6$/FEC:DEC (1:1). The Li/Si cells were cycled between 0.0 V and 1.2 V at a C/6 rate. After the first and thirtieth cycles, the Si electrodes were extracted from coin cells and rinsed with DMC in an Ar glovebox. The electrodes were transferred under Ar to the vacuum chamber of an

XPS for ex-situ measurements. From the cycling data, the cells cycled with FEC had a higher capacity retention and performed better than the cells without FEC. Improved cyclability of Li/Si cells with the presence of FEC is supported by Choi et al. [48]. There were very few differences in terms of SEI composition between electrodes extracted after the first or thirtieth cycle. After the first cycle, Nakai et al. observed that the FEC-derived SEI contained a greater concentration of F and C than the EC:DEC-based SEI. It was also found that the concentration of O at the surface of the SEI was lower in the FEC-based electrolyte than the EC-based electrolyte. In EC:DEC electrolytes, the SEI was oxygen-rich due to the decomposition products of EC and DEC (mainly, Li-oxides and Li-alkoxides). It was believed that the increased F concentration in the FEC-based SEI is due to the preferential reduction of FEC on the electrode surface than other electrolyte species.

Nakai et al. concluded that the FEC-derived SEI is *very thin* relative to the EC:DEC-derived SEI [44]. Nakai et al. suggested that the concentration of Si at the electrode surface reflected the thickness of the SEI. As there was more Si present at the surface of the electrode for the FEC-based electrolyte, it was determined to be thinner than the SEI formed with the EC:DEC solvent. From depth profiling (atomic concentration vs time as the surface was sputtered away) measurements using XPS, the Si concentration for the FEC-based electrolyte changed more steeply than the EC:DEC electrolyte, bolstering their conclusion. Nakai et al. suggested that the FEC-based SEI suppressed further decomposition of electrolyte due to the preferential reduction of FEC on the electrode surface. The improved cycling performance was considered to be caused by the suppression of SEI growth and cracking due to excessive decomposition of the electrolytes. It was suggested that for the EC:DEC electrolytes, the oxygen-rich SEI of Li-oxides and Li-alkoxides did not suppress electrolyte decomposition.

In Figures 6.20(a)-6.20(c), it is clear that the SEI layer was thicker in electrolytes containing additives. This greatly contrasts the results of Nakai et al. [44]. The following discussion attempts to answer the question: who is *correct*? Recall first that the measurements of Nakai et al. were performed ex-situ. The Si electrodes were extracted from the cells after the first and thirtieth cycle. In the publication, Nakai et al. gave no indication as to the state of charge of the Li/Si cells when the electrodes were

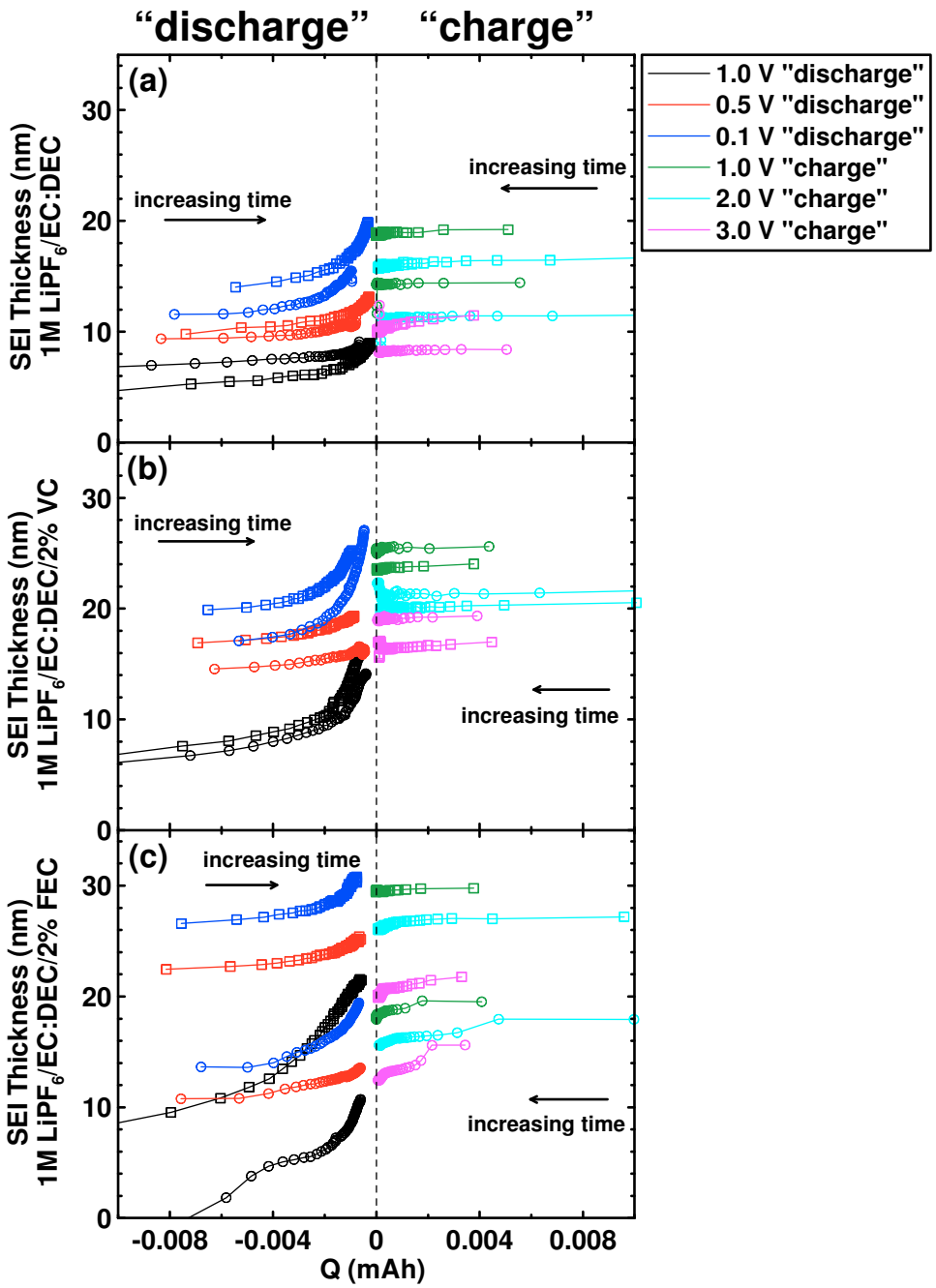

Figure 6.21 SEI layer thickness grown on TiN electrodes in Li/TiN in-situ cells plotted against the total charge, Q, delivered to the in-situ cells. The electrolytes used were: 1 M $LiPF_6$/EC:DEC (a), 1 M $LiPF_6$/EC:DEC/2% VC (b), and 1 M $LiPF_6$/EC:DEC/2% FEC (c). In the figure, coloured curves indicate the potential at which the in-situ cell was held and symbols describe various trials. Arrows indicate increasing time.

extracted. From our own in-situ work, it is clear that the SEI layer is thickest at the bottom of discharge and thinnest at the top of charge. So, if Nakai et al. disassembled the FEC-based cells during the charge and the EC:DEC-based cells during the discharge, a large discrepancy between SEI thickness would be observed. In the publication, the Si electrodes were rinsed prior to XPS analysis. It is unclear that these traditional rinsing steps prior to XPS analysis deteriorate the surface of the SEI. However, there is a possibility that the DMC rinse could distort a thin, delicate film, such as the SEI, in such a way as to report an artificially thickened (or thinned) film. Moreover, an SEI formed directly on the electrode surface may be bound more tightly than an SEI formed on a layer of reduced species from the FEC additive. An aggressive DMC rinse may have distorted the SEI layers and caused the FEC-based SEI to flake or slough off. Therefore, only the stable LiF and fluorinated Si would be detected. The measurements in this thesis were performed in-situ. As such, complications from rinsing are avoided entirely. However, it should be noted that ~8 mL of electrolyte was required to fill the in-situ cell. With such a large volume of electrolyte, a proportionate amount of impurities such as H_2O and HF would be present. During potentiostatic chronoamperomtry holds, these impurities would reduce, presumably before electrolyte species. As a result, the measured SEI thicknesses in-situ may have been thicker due to the impurity reaction species on the TiN electrode surface.

It has been observed that Li/graphite cells cycled with the addition of electrolyte additives, such as VC and FEC, have a much larger IRC than without the additives present [45]. IRC is due mainly to the formation of the SEI which irreversibly consumes Li in the cell. Thus, the IRC of a cell is closely related to the formation of the SEI layer. It follows that a cell with a large IRC would have a thick SEI layer and that a cell with a small IRC would have a thin SEI layer. Therefore, it makes sense that the SEI formed with the addition of electrolyte additives is thicker than without. It is thus believed that the SEI film thicknesses determined ellipsometrically are more robust than from other methods and that the SEI formed with the presence of additives is thicker than without.

Figures 6.21(a)-6.21(c) show SEI thickness data plotted against the total charge, Q, delivered to the Li/TiN in-situ cell during the potential hold studies. In Figures 6.21(a)-6.21(c), the coloured lines indicate the potential at which the in-situ cell was held

and the symbols contrast various trials. These data correspond to the thickness measurements in Figures 6.20(a)-6.20(c). Arrows indicate the direction of increasing time. The charge closely followed the current of the in-situ cell and approached 0 mA at the end of each potential hold. Figure 6.21(a) shows that the thickness of the SEI increased only slightly with charge until about -0.003 mAh and then rapidly increased to its local maxima. During the "charge", the SEI thickness did not change significantly as the total charge was varied. For Figures 6.21(b) and 6.21(c), the thickness of the SEI increased more rapidly with charge than in Figure 6.21(a) during the "discharge" at high potential (1 V). This is most likely a consequence of the preferential reduction of the additives VC and FEC on the electrode surface prior to other electrolyte species. The SEI then thickened rapidly to its local maximum near 0 mAh. For the other "discharge" holds (0.5 V and 0.1 V), the thickness of the SEI increased gradually until -0.003 mAh and then increased rapidly to the local maxima, as was observed in Figure 6.21(a). Similar to the cell with no additives, during the "charge", the thickness of the SEI rapidly decreased at each potential hold and remained relatively constant over the given range of charge. The instantaneous stripping of the SEI at potential holds above t = 30 h were poorly resolved in Figure 6.21. The ellipsometer and source-measure unit did not take a measurement at the same time and as such, no SE data was taken in these regions.

Chapter 7 Conclusion

Spectroscopic ellipsometry is a powerful research tool used to characterize very detailed reactions on a sample's surface. In this thesis, SE was used to carefully and methodically probe the surface of electrode materials during electrochemical testing in-situ. During the first discharge of a Li-battery (Li-ion battery), a thin transparent film, known as the solid electrolyte interphase, is formed on the electrode surfaces due to the reduction of electrolyte species. SE was used to observe and quantify its formation in real time. As well, SE was used to measure the optical constants of various electrolytes and the SEI itself.

In total, 3 electrode materials were studied in a novel electrochemical in-situ cell. These electrode materials, prepared by magnetron sputtering, included a-Si, Ni, and TiN thin films.

For a Li/a-Si in-situ cell cycled at a C/10 rate using constant current coulometry, measurements of SEI thickness could not be established due to the complexities of the Li-a-Si system. However, the ellipsometric parameters could be analyzed qualitatively to demonstrate the lithiation processes. As the a-Si thin film was lithiated, its optical properties changed from a transparent thin film to a metal-like opaque film suggesting the formation of an a-Li_xSi alloy. Large changes in Ψ and Δ most likely were due to the formation of an a-Li_xSi alloy, the formation of a thin transparent film, presumably the SEI, or a combination of both.

A Li/Ni in-situ cell was cycled at a C/5 rate using galvanostatic chronopotentiometry. It was shown that native oxide on the Ni surface underwent a displacement reaction with Li during lithiation near 0.4 V (see Eq. (6.1)). Moreover, a surface layer composed of displacement reaction products and SEI was observed. Its thickness was closely related to the cell's state of charge. The surface layer thickness increased to 17.1 ± 0.4 nm at the bottom of the first discharge and decreased to 5.4 ± 0.2 nm at the top of the first charge. An increase in thickness to 19.4 ± 0.5 nm was observed at the bottom of the second discharge. During the charge, the surface film was partially

stripped from the electrode surface, most likely due to the reverse displacement reaction (Eq. (6.1)).

The effect of electrolyte additives on the SEI was studied by potentiostatic chronoamperometry in Li/TiN in-situ cells. Electrolytes of 1 M $LiPF_6$/EC:DEC (1:2), 1 M $LiPF_6$/EC:DEC (1:2)/2 wt.% VC, and 1 M $LiPF_6$/EC:DEC (1:2)/2 wt.% FEC were tested. The formation of SEI was observed with all three electrolytes. It was found that the SEI formed on TiN electrodes with the presence of additives was thicker than without. These results make sense in terms of the IRC. It was found that the IRC is larger in Li/graphite cells with VC and FEC additives compared to cells prepared without the additives [45]. SEI is associated with IRC during cell cycling. Therefore, a large IRC corresponds to a thick SEI.

There are studies of SEI growth in the literature. In particular, there are in-situ investigations of SEI growth using SE (for example, Refs. [41-43, 90]). However, these studies typically omit the details necessary to repeat the measurements. The studies in this thesis present a methodical analysis of the growth of SEI with an emphasis on the SE technique. SE is a simple yet precise method used to observe and quantify the growth of the SEI on electrode materials for Li-ion batteries.

7.1 Future Work

The methods laid out in this thesis show a simple way to characterize SEI growth on electrode materials for Li-ion battery development. Provided the electrodes meet requirements such as low roughness, a high reflectivity, and no reaction with Li, SE can be used to measure the growth of an SEI film formed during electrochemical testing. An interesting candidate for future SEI growth analyses is carbon. Li intercalates into carbon to form LiC_6. Graphite, a structured carbon material, is currently the industry standard for negative electrode materials in Li-ion batteries. A carbon film can be easily prepared by magnetron sputtering. Although structurally different than graphite, sputtered carbon electrodes can be studied in-situ to obtain SEI layer information from the cycling of a Li/C in-situ cell.

It has been recently found that graphite powder can be "buff coated" onto many surfaces with good adhesion [91]. The process involves rubbing a graphite powder continuously in a circular motion onto a substrate. This "low-tech" method of preparing graphite can be applied to a glass plate substrate compatible with the current in-situ cell design. As Li/graphite is well understood, the results of a Li/C or Li/buffed graphite in-situ cell can be compared to the industry standard.

To increase the versatility of the in-situ cell equipment, the electrode "well" could be modified to allow for electrodes prepared by other methods to be studied. For example, glassy carbon, a highly reflective and smooth material, can be studied in the in-situ electrochemical cell. Its performance and the growth of the SEI could be compared to, say, the cycling behaviours of Li/sputtered C in-situ cells as well as to Li/graphite.

The SE analysis presented in much of this thesis was quantitatively robust. However, there were some difficulties matching an optical model to the optical parameters of the Li/a-Si in-situ cell. One must be able to correctly model the variation in ($n(\lambda)$, $k(\lambda)$) pairs of the a-Si electrode as the a-Li_xSi alloy is formed. This nontrivial task must be studied further in future in-situ studies.

Clearly, SE is a useful technique to study the formation of the SEI layer during electrochemical testing. It is predicted that this technique will be used in the future to uncover and understand many aspects of SEI formation during the cycling of Li-ion battery materials, old and new.

Bibliography

[1] E. Peled, J. Electrochem. Soc. **126**, 2047 (1979).

[2] E. Peled, D. Golodnitsky and G. Ardel, J. Electrochem. Soc. **144**, L208 (1997).

[3] D. Aurbach, J. Power Sources **89**, 206-218 (2000).

[4] D. Aurbach, B. Markovsky, I. Weissman, E. Levi and Y. Ein-Eli, Electrochim. Acta **45**, 67 (1999).

[5] D. Aurbach, B. Markovsky, M. Levi, E. Levi, A. Schechter, M. Moshkovich and Y. Cohen, J. Power Sources **81**, 95 (1999).

[6] M. Broussely, S. Herreyre, P. Biensan, P. Kasztejna, K. Nechev and R. J. Staniewicz, J. Power Sources **97-98**, 13 (2001).

[7] H. J. Ploehn, P. Ramadass and R. E. White, J. Electrochem. Soc. **151**, A456 (2004).

[8] A. J. Smith, J. C. Burns, X. Zhao, D. Xiong and J. R. Dahn, J. Electrochem. Soc. **158**, A447 (2011).

[9] D. Linden and T. Reddy, in *Handbook of Batteries*, edited by T. Reddy, 4th ed. (McGraw-Hill Professional, 2011).

[10] J. Dahn and G. M. Ehrlich, in *Linden's Handbook of Batteries*, edited by T. Reddy, 4th ed. (McGraw-Hill Professional, 2010).

[11] L. Y. Beaulieu, V. K. Cumyn, K. W. Eberman, L. J. Krause and J. R. Dahn, Rev. Sci. Instrum. **72**, 3313 (2001).

[12] I. A. Courtney and J. R. Dahn, J. Electrochem. Soc. **144**, 2045 (1997).

[13] O. Mao, R. A. Dunlap, I. A. Courtney and J. R. Dahn, J. Electrochem. Soc. **145**, 4195 (1998).

[14] A. Timmons and J. R. Dahn, J. Electrochem. Soc. **153**, A1206 (2006).

[15] J. R. Dahn, T. Zheng, Y. Liu and J. S. Xue, Science **270**, 590 (1995).

[16] M. N. Obrovac, L. Christensen, D. Ba Le and J. R. Dahn, J. Electrochem. Soc. **154**, A849 (2007).

[17] M. N. Obrovac and L. J. Krause, J. Electrochem. Soc. **154**, A103 (2007).

[18] M. Holzapfel, H. Buqa, F. Krumeich, P. Novak, F.-M. Petrat and C. Veit, Electrochem. Solid-State Lett. **8**, A516 (2005).

[19] L. Baggetto, J. Oudenhoven, T. van Dongen, J. Klootwijk, M. Mulder, R. Niessen, M. de Croon and P. Notten, J. Power Sources **189**, 402 (2009).

[20] L. Baggetto, J. F. M. Oudenhoven, T. van Dongen, J. H. Klootwijk, M. Mulder, R. A. H. Niessen, M. H. J. M. de Croon and P. H. L. Notten, J. Power Sources **189**, 402 (2009).

[21] L. Baggetto, N. Verhaegh, R. Niessen, F. Roozeboom, J. Jumas and P. Notten, J. Electrochem. Soc. **157**, A340 (2010).

[22] N. Pereira, M. Balasubramanian, L. Dupont, J. McBreen, L. C. Klein and G. G. Amatucci, J. Electrochem. Soc. **150**, A1118 (2003).

[23] D. Aurbach and A. Zaban, J. Electroanal. Chem. **348**, 155 (1993).

[24] M. Odzeimkowski, M. Krell and D. Irish, J. Electrochem. Soc. **139**, 3052 (1992).

[25] M. Odziemkowski and D. Irish, J. Electrochem. Soc. **139**, 3063 (1992).

[26] K. Kanamura, H. Tamura, S. Shiraishi and Z.-ichiro Takehara, J. Electroanal. Chem. **394**, 49 (1995).

[27] L. Dominey, in *Lithium Batteries: New Materials, Developments and Perspectives*, edited by G. Pistoia (Elsevier Science Ltd, 1993).

[28] K. R. Lawless, Rep. Prog. Phys. **37**, 231 (1974).

[29] M. Broussely, P. Biensan, F. Bonhomme, P. Blanchard, S. Herreyre, K. Nechev and R. Staniewicz, J. Power Sources **146**, 90 (2005).

[30] K.-Y. Peng, L.-C. Wang and J. C. Slattery, J. Vac. Sci. Technol. B **14**, 3316 (1996).

[31] P. Novák, D. Goers, L. Hardwick, M. Holzapfel, W. Scheifele, J. Ufheil and A. Würsig, J. Power Sources **146**, 15 (2005).

[32] M. Inaba, H. Tomiyasu, A. Tasaka, S.-K. Jeong and Z. Ogumi, Langmuir **20**, 1348 (2004).

[33] E. Peled, D. Bar Tow, A. Merson, A. Gladkich, L. Burstein and D. Golodnitsky, J. Power Sources **97-98**, 52 (2001).

[34] H. Schranzhofer, J. Bugajski, H. J. Santner, C. Korepp, K.-C. Möller, J. O. Besenhard, M. Winter and W. Sitte, J. Power Sources **153**, 391 (2006).

[35] H. J. Santner, C. Korepp, M. Winter, J. O. Besenhard and K.-C. Möller, Anal. Bioanal. Chem. **379**, 266 (2004).

[36] H. Buqa, A. Würsig, J. Vetter, M. E. Spahr, F. Krumeich and P. Novák, J. Power Sources **153**, 385 (2006).

[37] J.-ichi Yamaki, H. Takatsuji, T. Kawamura and M. Egashira, Solid State Ionics **148**, 241 (2002).

[38] Y. Wang, X. Guo, S. Greenbaum, J. Liu and K. Amine, Electrochem. Solid-State Lett. **4**, A68 (2001).

[39] C. Wang, A. J. Appleby and F. E. Little, J. Electroanal. Chem. **519**, 9 (2002).

[40] C. Wang, A. J. Appleby and F. E. Little, J. Electroanal. Chem. **497**, 33 (2001).

[41] K. Kwon, F. Kong, F. McLarnon and J. W. Evans, J. Electrochem. Soc. **150**, A229 (2003).

[42] F. Kong, R. Kostecki, G. Nadeau, X. Song, K. Zaghib, K. Kinoshita and F. McLarnon, J. Power Sources **97-98**, 58 (2001).

[43] F. Kong, J. Kim, X. Song, M. Inaba, K. Kinoshita and F. McLarnon, Electrochem. Solid-State Lett. **1**, 39 (1998).

[44] H. Nakai, T. Kubota, A. Kita and A. Kawashima, J. Electrochem. Soc. **158**, A798 (2011).

[45] D. Xiong, J. C. Burns, A. J. Smith, N. Sinha and J. R. Dahn, Submitted to 3M for Approval to Publish (2011).

[46] S. S. Zhang, J. Power Sources **162**, 1379 (2006).

[47] K. Xu, Chem. Rev. **104**, 4303 (2004).

[48] N.-S. Choi, K. H. Yew, K. Y. Lee, M. Sung, H. Kim and S.-S. Kim, J. Power Sources **161**, 1254 (2006).

[49] P. Drude, Annals of Physics **32**, 584 (1887).

[50] P. Drude, Annals of Physics **34**, 489 (1888).

[51] E. Bartholinus, *Experiments on Birefringent Icelandic Crystal* (Danish National Library of Science and Medicine, Copenhagen, 1991).

[52] C. Huygens, *Traité De La Lumière* (Leyden, 1690).

[53] É.-L. Malus, Procès-Verbaux De l'Academie Des Sciences **IV**, 144 (1808).

[54] É.-L. Malus, Mém. Soc. Arceuil **1**, 113 (1808).

[55] A. Fresnel, *Oeuvres Complètes d'Augustin Fresnel* (Imprimerie Impériale, Paris, 1866).

[56] D. B. Brewster, Phil. Trans. R. Soc. London **105**, 105 (1815).

[57] A. Rothen, Rev. Sci. Instrum. **16**, 26 (1945).

[58] D. E. Aspnes and A. A. Studna, Appl. Opt. **14**, 220 (1975).

[59] Y.-T. Kim, R. W. Collins, and K. Vedam, Surf. Sci. **233**, 341 (1990).

[60] H. Fujiwara, *Spectroscopic Ellipsometry: Principles and Applications* (Wiley, 2007).

[61] H. G. Tompkins and W. A. McGahan, *Spectroscopic Ellipsometry and Reflectometry: A User's Guide*, 1st ed. (Wiley-Interscience, 1999).

[62] H. G. Tompkins, *A User's Guide to Ellipsometry* (Dover Publications, 2006).

[63] D. J. Griffiths, *Introduction to Electrodynamics*, 3rd ed. (Benjamin Cummings, 1999).

[64] D. M. Mattox, *Handbook of Physical Vapor Deposition (PVD) Processing*, 1st ed. (William Andrew, 2007).

[65] J. Dahn, S. Trussler, T. Hatchard, A. Bonakdarpour, J. Mueller-Neuhaus, K. Hewitt and M. Fleischauer, Chem. Mater. **14**, 3519 (2002).

[66] V. Chevrier and J. R. Dahn, Meas. Sci. Technol. **17**, 1399 (2006).

[67] T. M. Byrne, S. Trussler, M. A. McArthur, L. B. Lohstreter, Z. Bai, M. J. Filiaggi and J. R. Dahn, Surf. Sci. **603**, 2888 (2009).

[68] I. H. Malitson, J. Opt. Soc. Am. **55**, 1205-1208 (1965).

[69] T. D. Hatchard and J. R. Dahn, J. Electrochem. Soc. **151**, A838 (2004).

[70] J. Hale and B. Johs, *CompleteEASE* (J.A. Woollam Co., Inc., 2009).

[71] M. A. McArthur, T. M. Byrne, R. J. Sanderson, G. P. Rockwell, L. B. Lohstreter, Z. Bai, M. J. Filiaggi and J. R. Dahn, Colloid. Surf. B **81**, 58 (2010).

[72] A. J. Smith, J. C. Burns, S. Trussler, and J. R. Dahn, J. Electrochem. Soc. **157**, A196 (2010).

[73] D. W. Marquardt, J. Soc. Indust. Appl. Math. **11**, 431 (1963).

[74] K. Levenberg, Quart. Appl. Math. **2**, 164 (1944).

[75] P. Patsalas and S. Logothetidis, J. Appl. Phys. **93**, 989 (2003).

[76] P. Patsalas and S. Logothetidis, J. Appl. Phys. **90**, 4725 (2001).

[77] G. E. Jellison and F. A. Modine, Appl. Phys. Lett. **69**, 371 (1996).

[78] P. Sánchez, O. Lorenzo, A. Menéndez, J. L. Menéndez, D. Gomez, R. Pereiro and B. Fernández, Ijms **12**, 2200 (2011).

[79] B. Johs and J. S. Hale, Phys. Stat. Sol. a **205**, 715 (2008).

[80] G. E. Jellison, M. F. Chisholm, and S. M. Gorbatkin Appl. Phys. Lett. **62**, 3348 (1993).

[81] H. Piller, *Handbook of Optical Constants I* (Academic, New York, 1985).

[82] P. Patsalas, C. Gravalidis and S. Logothetidis, J. Appl. Phys. **96**, 6234 (2004).

[83] T. Ogawa and K. Satoh, J. Chem. Eng. Data **21**, 33 (1976).

[84] D. P. Subedi, D. R. Adhikari, U. M. Joshi, H. N. Poudel and B. Niraula, Kathmandu University Journal of Science, Engineering and Technology **2**, 1 (2006).

[85] J. Lei, L. Li, R. Kostecki, R. Muller and F. McLarnon, J. Electrochem. Soc. **152**, A774 (2005).

[86] M. N. Obrovac and L. Christensen, Electrochem. Solid-State Lett. **7**, A93 (2004).

[87] Y. Wang and Q.-Z. Qin, J. Electrochem. Soc. **149**, A873 (2002).

[88] T. Zheng, A. S. Gozdz and G. G. Amatucci, J. Electrochem. Soc. **146**, 4014 (1999).

[89] J. Hilfiker, private communication (2010).

[90] F. Kong and F. McLarnon, J. Power Sources **89**, 180 (2000).

[91] A. Van Bommel, *Graphite Buff Coatings* (2011).